



저작자표시-비영리-변경금지 2.0 대한민국

이용자는 아래의 조건을 따르는 경우에 한하여 자유롭게

- 이 저작물을 복제, 배포, 전송, 전시, 공연 및 방송할 수 있습니다.

다음과 같은 조건을 따라야 합니다:



저작자표시. 귀하는 원저작자를 표시하여야 합니다.



비영리. 귀하는 이 저작물을 영리 목적으로 이용할 수 없습니다.



변경금지. 귀하는 이 저작물을 개작, 변형 또는 가공할 수 없습니다.

- 귀하는, 이 저작물의 재이용이나 배포의 경우, 이 저작물에 적용된 이용허락조건을 명확하게 나타내어야 합니다.
- 저작권자로부터 별도의 허가를 받으면 이러한 조건들은 적용되지 않습니다.

저작권법에 따른 이용자의 권리는 위의 내용에 의하여 영향을 받지 않습니다.

이것은 [이용허락규약\(Legal Code\)](#)을 이해하기 쉽게 요약한 것입니다.

[Disclaimer](#)

공학박사학위논문

**A study on the improved electrochemical properties of Si-based
anode and development of FeS₂ cathode for the Li-ion battery**

리튬 이차전지용 Si 계 음극의 전기화학 거동과
FeS₂ 양극 개발에 대한 연구

2014 년 2 월

서울대학교 대학원

재료공학부

손승범

**A study on the improved electrochemical properties of Si-based
anode and development of FeS₂ cathode for the Li-ion battery**

리튬 이차전지용 Si 계 음극의 전기화학 거동과
FeS₂ 양극 개발에 대한 연구

지도교수 오 규 환

이 논문을 공학박사학위논문으로 제출함

2013 년 12 월

서울대학교 대학원

재료공학부

손 승 범

손승범의 박사학위논문을 인준함

2013 년 12 월

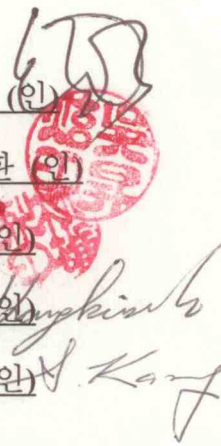
위 원 장 손헌준 (인)

부 위 원 장 오규환 (인)

위 원 유용렬 (인)

위 원 강기석 (인)

위 원 강선호 (인)



Abstract

Seoung-Bum Son

Department of Materials Science and Engineering

The graduate school

Seoul National University

This thesis studies the new electrode materials that possibly replace the current electrode materials for Li ion batteries. Electrochemical properties of Si based anode materials and FeS₂ cathode materials are studied and detailed microstructure observations are performed for the further understanding of the materials. This thesis is comprised of three parts. In the first part, we report the direct observation of microstructural changes of Li_xSi electrode with lithium insertion. HRTEM experiments confirm that lithiated amorphous silicon forms a shell around a core made up of the unlithiated silicon and that fully lithiated silicon contains a large number of pores of which concentration increases toward the center of the particle. Chemomechanical modeling is employed in order to explain this mechanical degradation resulting from stresses in the Li_xSi particles with lithium insertion. Because lithiation-

induced volume expansion and pulverization are the key mechanical effects that plague the performance and lifetime of high-capacity Si anodes in lithium-ion batteries, our observations and chemomechanical simulation provide important mechanistic insight for the design of advanced battery materials. In the second part, we report a Si-Ti-Ni ternary alloy developed for commercial application as an anode material for lithium ion batteries. Our alloy exhibits a stable capacity above 900 mAh g⁻¹ after 50 cycles and a high coulombic efficiency of up to 99.7% during cycling. To enable a highly reversible nano-Si anode, we employ melt spinning to embed nano-Si particles in a Ti₄Ni₄Si₇ matrix. The Ti₄Ni₄Si₇ matrix fulfills two important purposes. First, it reduces the maximum stress evolved in the nano-Si particles by applying a compressive stress to mechanically confine Si expansion during lithiation. And second, the Ti₄Ni₄Si₇ matrix is a good mixed conductor that isolates nano-Si from the liquid electrolyte, thus preventing parasitic reactions responsible for the formation of a solid electrolyte interphase. Given that a coulombic efficiency above 99.5% is rarely reported for Si based anode materials, our alloy's performance suggests a promising new approach to engineering Si anode materials. In the last part, we embed phase pure natural

cubic-FeS₂ (pyrite) in a stabilized polyacrylonitrile (PAN) matrix. The PAN matrix confines FeS₂'s electroactive species (Fe⁰ and S_n²⁻) for good reversibility and efficiency. Additionally, the stabilized PAN matrix can accommodate FeS₂'s 160% volume expansion upon full discharge because it is not fully carbonized. At room temperature, our PAN-FeS₂ electrode delivers a specific capacity of 470 mAh g⁻¹ on its 50th discharge. Using high resolution transmission electron microscopy (HRTEM) we confirm that FeS₂ particles are embedded in the PAN matrix and that FeS₂'s mobile electroactive species are confined during cycling. We also observe the formation of orthorhombic-FeS₂ at full charge, which validates the results of our previous all-solid-state FeS₂ battery study.

Student number: 2008-20653

Keywords: Silicon anode, X-ray diffraction, Focused Ion Beam, High Resolution Transmission Electron Microscopy, Chemomechanical modeling, Si-Ti-Ni alloy, Li Ion Batteries, melt spinning, nano-Si anode and Ti₄Ni₄Si₇ matrix, FeS₂, room temperature, reversible, liquid electrolyte, PAN.

Table of contents

Abstract	I
----------------	---

Table of contents	IV
-------------------------	----

List of Tables	VIII
----------------------	------

List of Figures	IX
-----------------------	----

Chapter 1: Introduction

1.1 Concept of lithium ion battery	1
--	---

1.2 Cathode materials	8
-----------------------------	---

1.3 Anode materials	14
---------------------------	----

1.4 Theoretical capacity	16
--------------------------------	----

1.5 Energy density and power density	17
--	----

1.6 References	19
----------------------	----

Chapter 2: Microstructure observation of electrochemically driven Li_xSi

2.1 Introduction	22
2.2 FIB apparatus equipped with air-lock system	25
2.3 Electrode sample preparation and XRD studies	30
2.4 HRTEM observation on electrode samples	37
2.5 Chemomechanical simulation	42
2.6 Conclusion	45
2.7 Materials and methods	46
2.8 References	51

Chapter 3: A highly reversible nano-Si anode enabled by mechanical confinement in an electrochemically activated $\text{Li}_x\text{Ti}_4\text{Ni}_4\text{Si}_7$ matrix

3.1 Introduction	54
3.2 Previous study with carbon coating on nano-Si	57
3.3 Synthesis of Si-Ti-Ni alloy: Mechanical confinement	61
3.4 Electrochemical properties of Si-Ti-Ni	66

3.5 Ionic conductivity measurement of $\text{Ti}_4\text{Ni}_4\text{Si}_7$ matrix	70
3.6 Material evolution of Si-Ti-Ni during cycling	77
3.7 Conclusion	80
3.8 Experimental section	82
3.9 References	86

Chapter 4: A Stabilized PAN- FeS_2 Cathode with an EC/DEC Liquid Electrolyte

4.1 Introduction	91
4.2 Previous study of Li/pyrite with solid state electrolyte	96
4.2.1 Solid state battery architecture	96
4.2.2 Reversible cycle stability of Li/ FeS_2 with solid state battery	100
4.3 Li/pyrite with EC/DEC electrolyte	105
4.3.1 Synthesis and microstructure observation of PAN- FeS_2	105
4.3.2 Electrochemical properties of PAN- FeS_2 and bare FeS_2	110
4.3.3 Microstructure observation of 10th charged PAN- FeS_2	115
4.3.4 Detailed dq/dv analysis of PAN- FeS_2 and bare FeS_2	122
4.3.5 Experimental section	131

4.4 Conclusions	134
4.5 References	135
Conclusion	140
요약 (국문초록)	143
Curriculum Vitae	146
Appendix 1	154
Appendix 2	161

List of Tables

Table 3.1. Space groups, lattice constants and atomic positions of Si and $\text{Ti}_4\text{Ni}_4\text{Si}_7$. Information in Table S1 is used for F method of STN alloy. Rietveld method shows that STN is 46 wt % Si and 54 wt % $\text{Ti}_4\text{Ni}_4\text{Si}_7$.

List of Figures

Figure 1.1. Simplified schematic of Li ion battery.

Figure 1.2. Models of the layered LiCoO_2 structure. (a) Drawn with lithium ions horizontally between CoO_2 octahedra. Lattice parameters $a_{\text{hex.}} = b_{\text{hex.}} = 2.8138 \text{ \AA}$ and $c_{\text{hex.}} = 14.0516 \text{ \AA}$. (b) Projection along the $[110]$ zone axis shows lithium, cobalt and oxygen atoms in columns. The projected cell is 2.44 \AA by 14.05 \AA .

Figure 1.3. Discharge voltage profiles of the LiCoO_2 cycled at different current densities (a) uncoated bulk LiCoO_2 (br-bLCO) (b) uncoated nano- LiCoO_2 (br-nLCO), and Al_2O_3 -coated nano- LiCoO_2 by (c) 2ALD and (d) 6ALD cycles on the electrodes.

Figure 2.1. FIB equipped with air-lock system and mobile chamber

Figure 2.2. General sequence of producing TEM sample prepared by FIB. (a) Pt deposition for surface protection. (b) Cross sectioning of desired particle. (c) Sample lift out using manipulating probe. (d) Achieved TEM sample on Cu grid.

Figure 2.3. (a) Voltage profile of Si anode at voltage range of 0.01 V to 1.5 V. (b) Corresponding differential capacity versus voltage curve.

Figure 2.4. A cross sectional image of Si particle with SEI layer.

Figure 2.5. Proposed model that suggests how a single silicon particle changes its microstructure during cycling.

Figure 2.6. XRD patterns of crystalline Si phase in JCPDS, experimental Li_2Si and experimental $\text{Li}_{4.4}\text{Si}$.

Figure 2.7. TEM images of Li_2Si . (a) BF image of Li_2Si . (b) HR and corresponding FFT of area A indicates that amorphous. (c) HR and

corresponding FFT of area B indicates that Si crystalline phase along the [112] direction.

Figure 2.8. BF image and corresponding diffraction pattern of $\text{Li}_{4.4}\text{Si}$.

Figure 2.9. Generated stress concentration profiles during Li insertion. (a) Radial stress. (b) Tangential stress. (c) Li ion concentration.

Figure 2.10. A schematic of all solid state Li ion battery in Ti metal test die.

Figure 2.11. A schematic of the electrode particle model.

Figure 3.1. TEM-EELS elemental mapping confirming that we achieve a conformal 5 nm thick PAN-carbon coating. (Cyan: Carbon, Red: Silicon)

Figure 3.2. (a) Cyclic capacity (blue circles) and CE (blue squares) of PAN-Si electrodes run at a rate of C/20 for the first 10 cycles and at C/10 for subsequent cycles. A conventional nano-Si electrode (red circles) was cycled

at a rate of C/10 as a control cell. After 150 cycles, our PAN-Si composite electrode has a specific charge capacity of nearly 1500 mAh g⁻¹ and a CE approaching 100%, whereas the conventional electrode fails after 3 cycles. (b) Voltage profiles of our nano-Si/cyclized-PAN electrode showing a minimal overpotential when cycled at 0.1C compared to 0.05C.

Figure 3.3. (a) Simplified schematics of melt spinner. (b) Achieved melt spun STN ribbon. (c) XRD pattern of ball milled melt spun STN powder that matched with Si phase (JCPDS, 27-1402) and Ti₄Ni₄Si₇ phase (JCPDS, 80-1015). (d) TEM image with HAADF mode of nano-Si and Ti₄Ni₄Si₇. (e) EDS results of given area in Figure 3.1d.

Figure 3.4. (a) Specific capacity and CE of STN anode versus cycle numbers. (b) Voltage profile of Si, STN and normalized STN to Si mass between 0.01 V and 1.5 V.

Figure 3.5. FIB equipped with air-lock system and the general TEM sample preparation sequence using the FIB. (a) FIB equipped with autonomously

developed air-lock system. (b) Pt deposited to protect particle surface. (c) Cross sectioning of desired STN particle. (d) Sample lift out using manipulating probe. (e) Achieved TEM sample on Cu grid.

Figure 3.6. TEM EELS mapping results of $\text{Ti}_4\text{Ni}_4\text{Si}_7$ electrode after 20th cycle. Strong contrast in given area infers that corresponding element is detected. (a) Zero loss. (b) Si map result. (c) Li map result. (d) Ni map result. (e) Ti map result.

Figure 3.7. (a) Voltage profile versus specific capacity of $\text{Ti}_4\text{Ni}_4\text{Si}_7$ between 0.01 V and 1.5 V. (b) Differential capacity versus voltage curve of STN and $\text{Ti}_4\text{Ni}_4\text{Si}_7$. (c) Schematics of solid state conductivity cell configuration. (d) CV test between -0.2 V and 0.2 V of $\text{Li}_{3.2}\text{Ti}_4\text{Ni}_4\text{Si}_7$.

Figure 3.8. (a) Voltage profile versus specific capacity of 1, 10, 20, 30, 40 and 50 cycles with schematics of STN structure. (b) EELS zero loss image at 50th charged status. (c) EELS mapping at 50th charged status (where red: Si, cyan: Li).

Figure 3.9. XRD result of synthesized $\text{Ti}_4\text{Ni}_4\text{Si}_7$.

Figure 4.1. (a) FESEM micrograph of synthetic FeS_2 that confirms cubic structure with 2-3 μm cubes. (b) X-ray diffraction of synthetic pyrite.

Figure 4.2. ASSLBs configuration. Black represents SLMP material, orange represents sulfide based glass-ceramic electrolyte 77.5 Li_2S – 22.5 P_2S_5 system and blue represents synthetic FeS_2 active material.

Figure 4.3. FeS_2 cycled at 30°C and 60°C in conventional liquid coin cell and in an all-solid-state configuration. (a) solid-state at 30°C, (b) solid-state at 60°C, (c) liquid coin cell at 30°C, (d) liquid coin cell at 60°C, (e) cycling data for cells cycled at 30°C, and (f) cycling data for cells cycled at 60°C. All cells cycled at a rate of C/10 for charge and discharge.

Figure 4.4. FIB preparation sequence. (a) Pt deposition upon FeS_2 particle, (b) Ga^+ ion milling of FeS_2 particle, (c) recovery of FeS_2 particle using lift-out technique and (d) final thinning of FeS_2 sample to 50-80nm.

Figure 4.5. Electrode material from the solid-state cell cycled at 60°C was recovered after the 20th charge for TEM analysis. (a) Bright field TEM image

of the 20th cycle sample. (b) HR-TEM of the 20th cycle sample. FFT analysis matches with orthorhombic-FeS₂ along the [-110] zone axis.

Figure 4.6. (a) SEM observation of 1hour ball milled natural pyrite. (b) After natural pyrite is ball milled, powder XRD analysis was performed to determine the phases and matched with cubic-FeS₂ (71-2219).

Figure 4.7. (a) Cross-sectional SEM image of an uncycled PAN-FeS₂ electrode. (b) TEM image with EELS zero-loss mode of the stabilized PAN matrix (light) and embedded FeS₂ particles (dark). (c) EELS elemental mapping of C (red), Fe (blue), and S (green).

Figure 4.8. (a) EELS iron mapping of Figure 1b. (b) EELS sulfur mapping of Figure 1b. (c) EELS carbon mapping of Figure 1b.

Figure 4.9. (a) Cyclic stability of the stabilized PAN-FeS₂ electrode versus that of a bare FeS₂ electrode. Specific capacity is reported w.r.t. mass of the FeS₂ active material. (b) Voltage profiles of PAN-FeS₂. (c) Voltage profiles of bare FeS₂.

Figure 4.10. Typical TEM sample preparation sequence using the FIB. (a) Pt deposition on protect particle surface and cross sectioning of desired PAN-FeS₂ particle. (b) Sample lift out using manipulating probe on Cu grid. (c) Achieved final TEM sample.

Figure 4.11. (a) TEM image of an embedded FeS₂ particle in a PAN-FeS₂ electrode collected after completion of its 10th charge. (b) High resolution (HR) image of the FeS₂ particle in Figure 4.9a and the corresponding FFT pattern matched with orthorhombic-FeS₂ along the [01-1] zone axis. (c) EELS elemental mapping for Fe. (d) EELS elemental mapping of S.

Figure 4.12. (a) TEM image with EELS zero-loss mode of Figure 4.11a. (b) EELS carbon mapping of area Figure 4.11a.

Figure 4.13. Cyclic capacity and voltage profile of an electrode manufactured with stabilized PAN, acetylene black, and PVDF following the same configuration, treatment, and electrochemical parameters as our stabilized

PAN-FeS₂ electrodes, respectively. It is shown that stabilized PAN is electrochemically stable within a voltage window of 1V to 3V.

Figure 4.14. The reduction of sulfur in an organic liquid electrolyte follows a three step process. Yellow balls represent sulfur atoms while grey balls represent lithium atoms.

Figure 4.15. Li - S phase diagram.

Figure 4.16. (a) Reductive dQ/dV profiles for the PAN-FeS₂ electrode and (b) reductive dQ/dV profiles for the bare FeS₂ electrode. The peaks at approximately 2.5V and 2.2V are attributed to Eq. (4.6) and Eq. (4.7) and Eq. (4.8), respectively, while the peak at approximately 2.1V is attributed to Eq. (4.1).

Figure 4.17. (a) Differential capacity versus voltage curve of PAN-FeS₂. (b) Differential capacity versus voltage curve of bare FeS₂.

Figure 4.18. Raman spectra for untreated PAN (blue) and PAN treated at 200°C in air for 1 hour and then at 500°C under Ar flow for 1 hour (red). The observation of graphite D and G bands confirms delocalized sp² π bonding which confirms a good intrinsic electronic conductivity and a conjugated structure.

Chapter 1: Introduction

1.1 Concept of lithium ion battery

Recent intense news coverage with critical energy issues indicate that worldwide concern is focusing on limited resources [1]. Natural resources such as fossil fuels and bio mass enable the use of modern technology but at the same time gaseous emissions from those resources not only pollute our environments but also create global warming [2]. Rising oil prices mainly caused by instability of Northern Africa and Middle East, worries about resource exhaustion, and aging nuclear plants with high potential for danger also make publics pay more attention to alternative energy sources [1]. So renewable solar and wind energy have attracted interests but variability in time and diffuse in space make renewables hardly replace the conventional oil and gas resources [2, 3]. Advanced batteries can store the occasional energy and give renewables an opportunity to replace the established energy resources.

In the last two decades, various kinds of energy storage systems such as hydrogen storages, fuel cells and many kinds of batteries have been

intensively researched. Although each storage systems have their own advantages and drawbacks but most of them are failed to be commercialized or remained as small sized batteries. However rechargeable lithium ion batteries (LIBs) which have relatively high power and energy densities have been spot lighted as a promising energy storage method for future use and commercialized in 1990's by Sony and Asahi Kasei.

First LIBs were reported by M.S. Whittingham now at Binghamton University in 1970's [5]. TiS_2 was used as a cathode material with intercalation chemistry against Li metal anode. Following equation was proposed as TiS_2 's single phase reaction.



It has been passed many years and now LIBs have revolutionized the way we live by powering the portable electric devices that provides all the conveniences around our lives.

LIBs are an indispensable power source for a variety of hand-held electronic devices and nowadays, LIBs are being developed with new electrode materials to provide electric vehicles (EV), hybrid electric vehicles (HEV) and plug-in hybrid electric vehicles (PHEV) with an affordable and

energy dense storage system [6, 7]. These applications demand electrode materials with a higher specific energy than that provided by commercially available materials. And from a life cycle perspective, it is essential that LIBs are made with environmentally benign materials.

Figure 1.1 describes a general concept of LIB. Generally LIBs are composed of anode, cathode, electrolyte, separator and current collectors. Simplified definition of terminologies can be found as follows.

- Anode – Electrode that undergoes *oxidation* during discharge and has a lower potential vs. Li compared to cathode.
- Cathode – Electrode that undergoes *reduction* during discharge and has a greater potential vs. Li compared to anode.
- Electrolyte – Organic liquid comprised of a lithium bearing salt-compound to promote Li-ion transport between anode and cathode.
- Current Collector – Electrically conductive metal to allow for the flow of electrons to each electrode.
- Separator – Porous, fibrous, silica sheet that prevents physical contact between anode and cathode while allowing for the flow of electrolyte/Li ion.

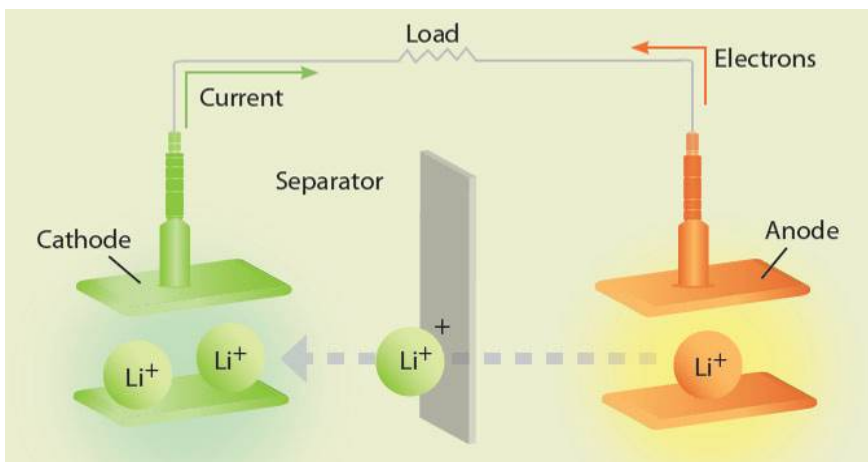
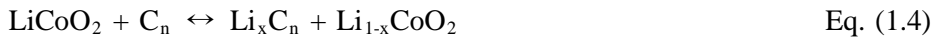


Figure 1.1. Simplified schematic of Li ion battery.

Since current LIBs are generally composed of LiCoO_2 cathode and graphite anode, electrochemical reactions of cathode and anode during charge and discharge are represented as



And overall reaction is described as



Repeatable charge and discharge reactions enable the function of rechargeable LIBs. During the charge, Li ions carry electrons and flow from cathode to anode in a conducting electrolyte, through a separator. While the LIBs are discharged, Li ions flow back to the cathode.

Difference in the chemical potential between two electrodes is the chemical driving force and this is expressed as *Standard Gibbs free energy change per mole of reaction*, ΔG°_r . This is determined by the difference between the *standard Gibbs free energy of formation* of products and reactants. When the Li ion moves from the cathode to the anode or vice versa, the Li potential in the cathode and anode changed. The Li chemical potential of the cathode and anode are defined in terms of the Li chemical potential in

its standard state and the activity of Li in the cathode or anode material.

$$\mu_{Li}^c = \mu_{Li}^o + RT \ln a_{Li}^c \quad \text{Eq. (1.5)}$$

$$\mu_{Li}^a = \mu_{Li}^o + RT \ln a_{Li}^a \quad \text{Eq. (1.6)}$$

$$\Delta\mu = -nFE \quad \text{Eq. (1.7)}$$

$$V_{oc} = (\mu_{Li}^c - \mu_{Li}^a) / F \quad \text{Eq. (1.8)}$$

Since the voltage in Eq. (1.8) is defined as the difference between the chemical potentials at the cathode and anode that is divided by Faradaic constant, F . And a relationship between voltage and activity is derived in Eq. (1.7) and known as Nernst equation [9].

The open-circuit voltage V_{oc} of LIBs is determined by the energies involved in both the electron transfer and the Li ion transfer. The energy involved in electron transfer is related to the work functions of the cathode and anode, which involved in Li ion transfer determined by the crystal structure and the coordinating geometry of the site into/from Li ions are inserted or extracted. Thermodynamic stability considerations require the redox energies of the cathode and the anode to lie within the band-gap of the electrolyte, so that no unwanted reduction or oxidation of the electrolyte occurs during the charge/discharge process. Thus the electrochemical stability

requirement imposes a limitation on the cell voltage as follow.

$$eV_{oc} = \mu_{Li}^c - \mu_{Li}^a < E_g \quad \text{Eq. (1.9)}$$

1.2 Cathode materials

The lithium cobalt oxide, LiCoO_2 , was among the lithium intercalation materials first reported by Mizushima in 1980's [10], and is currently the most extensively used cathode material for LIBs. Theoretical capacity of LiCoO_2 is about 274 mAh g^{-1} . However specific capacity of $\sim 150 \text{ mAh g}^{-1}$ is reversibly cycled due to structural restriction [11, 12]. Generally 0.5 mole of Li ions (Eq. (1.2)) participates intercalation reaction voltages up to 4.2 V (vs Li/Li^+) for stable cycle ability [13]. Using a voltage range above 4.2 V may results in increase of specific capacity but also leads the rapid capacity fade over 4.2 V. Figure 1.2 well describes a layered LiCoO_2 structure [8]. It has been known that over charging higher than 4.2 V causes LiCoO_2 structure degradation and electrolyte decomposition [14]. As Li ion is removed from Li_xCoO_2 , Co^{3+} is oxidized to unstable Co^{4+} . Increase of Co^{4+} amount damages the structure of LiCoO_2 with decrease of C-axis caused by a phase transition. The volume contraction along C-axis results in mechanical failure in LiCoO_2 structure which also leads rapid capacity fade during cycling. It has been also reported that the capacity degradation of LiCoO_2 is partially related with the dissolution of Co^{3+} ion into the liquid electrolyte

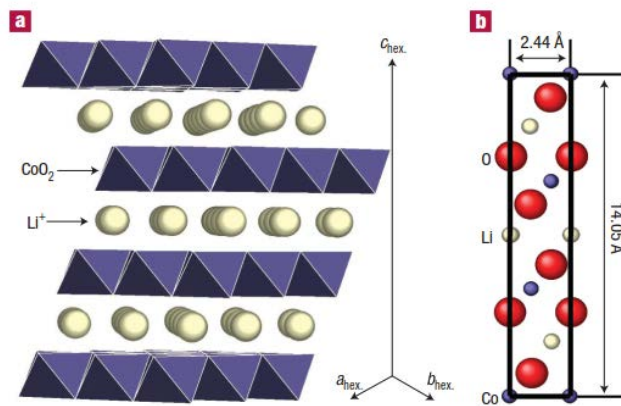


Figure 1.2. Models of the layered LiCoO_2 structure. (a) Drawn with lithium ions horizontally between CoO_2 octahedra. Lattice parameters $a_{\text{hex.}} = b_{\text{hex.}} = 2.8138 \text{ \AA}$ and $c_{\text{hex.}} = 14.0516 \text{ \AA}$. (b) Projection along the $[110]$ zone axis shows lithium, cobalt and oxygen atoms in columns. The projected cell is 2.44 \AA by 14.05 \AA

solution [15, 16].

Figure 1.3 shows the typical discharge voltage plateau of LiCoO_2 with variation of particle size and atomic layer deposition (ALD) coating [17]. Since the theoretical capacity of LiCoO_2 is limited by $\sim 150 \text{ mAh g}^{-1}$, lots of efforts to improve the cycle abilities have been made. Two major approaches for the improvement of cycle ability of LiCoO_2 were use of nano sized LiCoO_2 particles and ALD surface coatings. Nano sized particles decreases the over-potential compared to bulk sized particle and thus achieved capacity is increased. This indicates that more surface area helps to increase the kinetics and contribute to accelerate charge transfer reaction [17]. Al_2O_3 ALD coatings on LiCoO_2 particles or electrode surfaces are now well known approach to improve in cycle performance of LiCoO_2 . It is known that surface engineering of LiCoO_2 particles by using ALD coatings are effective for lowering interfacial resistance and reducing Co dissolution during cycling. Therefore good cycle stability is achieved by ALD coating even with a high upper limit voltage over 4.2 V [17, 18]. However intrinsic theoretical capacity of LiCoO_2 is still insufficient for advanced batteries and various LiMO_2 (M = transition metal) layered structure materials are developed. Among materials

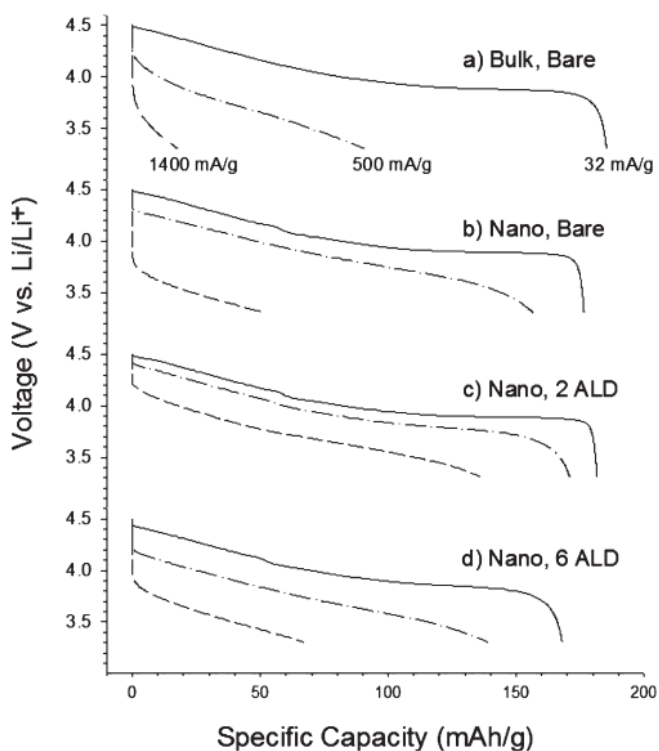


Figure 1.3. Discharge voltage profiles of the LiCoO_2 cycled at different current densities (a) uncoated bulk LiCoO_2 (br-bLCO) (b) uncoated nano- LiCoO_2 (br-nLCO), and Al_2O_3 -coated nano- LiCoO_2 by (c) 2ALD and (d) 6ALD cycles on the electrodes.

$\text{Li}[\text{Ni}_{1/3}\text{Co}_{1/3}\text{Mn}_{1/3}]\text{O}_2$ materials that has the same amounts of transition metal of Ni, Mn, and Co will be introduced here to understand the role of each transition metal ions in the layered structure [19]. This material has the same structure with LiCoO_2 but 3 different elements have different oxidation state and enables super lattice structure which is more stable than LiCoO_2 . In $\text{Li}[\text{Ni}_{1/3}\text{Co}_{1/3}\text{Mn}_{1/3}]\text{O}_2$, oxidation state of Ni, Co, and Mn are +2, +3, and +4, respectively. So electrochemically inactive tetravalent Mn provides the structural stability during cycling against Li even at high voltage of 4.6 V and also reduced Co^{+3} improves the thermal stability comparing to LiCoO_2 [20]. As a result, $\text{Li}[\text{Ni}_{1/3}\text{Co}_{1/3}\text{Mn}_{1/3}]\text{O}_2$ shows higher than 200 mAh g^{-1} of specific capacity at voltage of 4.6 V and now attracts a lot of attention as a possible cathode materials.

However it seems hard to meet the continuous demands for higher power with energy dense system with these layered LiMO_2 with intercalation reaction limited by its inevitable capacity limits owing to number of exchanged electron [21-23]. So-called conversion reaction materials which are represented by Sulfur have brought interest with an expectation of higher gravimetric and volumetric capacity system [25]. A lot of effort has been

being made on sulfur for the use of reversible Li/S batteries. However it has not yet to be commercialized due to electrochemical irreversibility with Li. The most reason of irreversibility of sulfur lies on the head of solubility of polysulphide to liquid electrolyte. Among the sulphide materials that have conversion reaction [21], iron sulphides (FeS_2) have been considered as lithium primary batteries [22] due to its high specific capacity (894 mAh g^{-1} for FeS_2) [26, 27]. In this thesis, chapter 3 studies the PAN- FeS_2 cathode material to demonstrate the improved reversibility of Li/ FeS_2 system.

1.3 Anode materials

Most of current LIBs adopt graphite intercalation materials as an anode part. Graphite has been initially invented by R. Yazami in 1980's. [28] Graphite basically comprises sp_2 -hybridized carbon atoms arranged in a planar "honeycomb-like" network so called as a "graphene" layer is formed. Van der Waals forces between graphene layers provide a weak cohesion and this enables the layered graphite structure. A maximum lithiation amount of one Li per six carbon atom can deliver the theoretical capacity of 372 mAh g^{-1} forming LiC_6 . The intercalation reaction between lithium and carbon proceeds via the prismatic surface but occurs only at defect sites through the basal plane. The interlayer distance between graphene layers can be changed upon lithium insertion and extraction. The stacking order of graphene layers shift from AB to AA and total volume of graphite increases as 10.3%. Currently, artificial of synthetic graphite are commonly used for the industrial application [28].

The demands for development of advanced battery with higher energy and power density need new anode material with higher volumetric and gravimetric capacity. Most promising candidate that can replace the graphite

is Si. The best advantage that silicon has is that silicon has a capacity of 3579 mAh g⁻¹ which is 10 times higher than graphite. However, silicon has not been successfully used in a commercial battery yet because when Si is alloying with Li, it undergoes volume expansion around 400% accompanied by mechanical stress and this fact brings poor cycle life of Si [29-31]. In this thesis, chapter 2 studies the detailed microstructure observation of Li_xSi upon Li insertion and chapter 3 studies a highly reversible Si-Ti-Ni anode to meet the demand for a low-cost, high capacity with a high coulombic efficiency and good capacity retention.

1.4 Theoretical capacity

The theoretical capacity of LIB is determined by the amount of active materials in the cathode and anode. It is represented as the total quantity of electricity involved in the electrochemical reaction and is defined in terms of coulombs or ampere-hour (Ah). In general, 1 gram-equivalent weight of active material deliver 96,487 C or 26.8 Ah and the definition of the gram-equivalent weight is the atomic or molecular weight of the active material in grams divided by the number of electrons or Li ions involved in the reaction. Similarly, the ampere-hour capacity on a volume basis can be calculated using the appropriate data for ampere-hour per cubic centimeter.

1.5 Energy density and power density

The capacity of a LIB can also be shown as an energy term in order to take both the voltage and the quantity of electricity into consideration. The theoretical energy is the maximum value that can be delivered by a specific LIB system and it is calculated as the product of voltage and capacity with the unit of watt-hour. The actual energy density is always less than the theoretical energy density due to the inactive components in the LIB such as the electrolyte, binders and conductive additives, and current collectors.

The rate at which energy is delivered from or to the LIB decides its power density. The maximum power which the LIB can deliver or accept is determined by the highest rate at which the LIB can be cycled without any failure and is governed by kinetic process of the whole system of the LIB. In practice, the charge/discharge rate is expressed in terms of C-rate and defined as

$$I = M \times C_n \quad \text{Eq. (1.10)}$$

where, I is discharge (charge) current [A], C is numerical value of rated capacity of the LIB [Ah], n is time for which rated capacity is declared [hr], and M is multiple or fraction of C .

In addition, E-rate in terms of the rate of the constant power discharge mode is becoming more popular for battery powered application such as PHEV or EV batteries. E-rate can be used to express the discharge or charge rate in terms of power

$$P = M \times E_n \quad \text{Eq. (1.11)}$$

where, P is power [W], E is numerical value of rated energy of the LIB [Wh], n is time at which the LIB was rated [hours] and M is multiple of fraction of E .

1.6 References

- [1] J. W. Tester, *Energ. Environ. Sci.* **2011**, 4, 10.
- [2] J. B. Goodenough, Y. Kim, *Chem. Mater.* **2010**, 22, 3.
- [3] <http://www.eia.doe.gov/fuelrenewable.html>. Accessed on 05/25/2009.
- [4] http://en.wikipedia.org/wiki/Lithium-ion_battery
- [5] M.S. Whittingham, *Science* **1976**, 192, 4244.
- [6] J. M. Tarascon, M. Armand, *Nature* **2001**, 414, 359.
- [7] S. D. Beattie, D. Larcher, M. Morcrette, B. Simon, J. M. Tarascon, *J. Electrochem. Soc.* **2008**, 155, 158.
- [8] Y. Shao-horn, L. Croguennec, C. Delmas, E. Chris Nelson, M. A. O'Keefe, *Nat. Mat.* **2003**, 2, 7.
- [9] R. A. Huggins, *Advanced Batteries: Materials Science Aspects*, Springer, **2008**.
- [10] K. Mizushima, P.C. Jones, Pal. Wiseman, John B. Goodenough, *Mater. Res. Bull.* **1980**, 17, 783.
- [11] C. Delmas, *Mater. Sci. Eng.* **1989**, B3, 97.
- [12] R. Koksang, J. Barker, H. Shi, M.Y. Saïdi, *Solid State Ionics* **1996**, 84, 1.

- [13] A. Sakuda, H. Kitaura, A. Hayashi, K. Tadanaga, M. Tatsumisago, *J. Power Sourc.* **2009**, 189, 527.
- [14] J.N. Reimers, J.R. Dahn, *J. Electrochem. Soc.* **1992**, 139, 2091.
- [15] G.G. Amatucci, J.M. Tarascon, L.C. Klein, *Solid State Ionics* **1996**, 83, 167.
- [16] H. Li, Z. Wang, L. Chen, X. Huang, *Adv. Mater.* **2009**, 21, 45.
- [17] I. D. Scott, Y. S. Jung, A. S. Cavanagh, Y. Yan, A. C. Dillon, S. M. George, S.-H. Lee, *Nano Letters* **2011**, 11, 2.
- [18] J. H. Woo, J. E. Trevey, A. S. Cavanagh, Y. S. Choi, S. C. Kim, S. M. George, K. H. Oh, S.-H. Lee, *J. Electrochem. Soc.* **2012**, 159, 7.
- [19] T. Ohzuku, Y. Makimura, *Chem. Lett.* **2001**, 7.
- [20] S.-T. Myung, K. Izumi, S. Komaba, Y.-K. Sun, H. Yashiro, N. Kumagai, *Chem. Mater.* **2005**, 17, 14.
- [21] Y. Kim, J.B. Goodenough, *J. Phys. Chem. C* **2008**, 112, 38.
- [22] M.S. Whittingham, *Chem. Rev.* **2004**, 104, 10.
- [23] J.B. Goodenough, *J. Power Sourc.* **2007**, 174, 2.
- [25] X.L. Ji, K.T. Lee, L.F. Nazar, *Nat. Mat.* **2009**, 8, 6.
- [26] D. Bernardi, J. Newman, *J. Electrochem. Soc.* **1987**, 134, 6.

- [27] R. Fong, J.R. Dahn, C.H.W. Jones, *J. Electrochem. Soc.* **1989**, 136, 11.
- [28] R. Yazami, P. Touzain, *J. Power Sourc.* **1983**, 9, 3.
- [29] S. Golmon, K. Maute, S. H. Lee, M. L. Dunn, *Appl. Phys. Lett.* **2010**, 97
- [30] V. A. Sethuraman, M. J. Chon, M. Shimshak, V. Srinivasan, P. R. Guduru, *J. Power Sourc.* **2010**, 195, 5062.
- [31] S. D. Beattie, D. Larcher, M. Morcrette, B. Simon, J. M. Tarascon, *J. Electrochem. Soc.* **2008**, 155, A158.

Chapter 2: Microstructure study of electro-chemically driven Li_xSi

2.1 Introduction

Currently, graphite is a popular anode material for commercial LIBs because it exhibits a stable capacity of 372 mAh g^{-1} [1-4]. Although graphite has proven to be a stable anode material, industry is interested in developing new anode materials with higher capacities. One of the most promising materials studied to replace graphite is Silicon (Si). The experimentally verified specific capacity of Si is 3579 mAh g^{-1} (forming $\text{Li}_{15}\text{Si}_4$) which is the highest specific capacity known among materials to the date [5-8].

The major drawback to silicon is the volume expansion upon Li insertion in the range of 300% to 400% occurring due to the formation of Li_xSi alloys [9-14]. Stress associated with the large volume changes have been cited as the cause of cracking and pulverization of Si electrodes that lead to a loss of electrical contact and capacity fade during cycling.

Commonly, researchers focus on resolving capacity fade of Si anodes caused by mechanical failure upon Li insertion. Some researchers have

approached this problem using nano structured Si based materials such as Si nanowires, Si-C nano composites, and/or 3D-porous Si particles [15-17]. Recently, it has been reported that nano-Si powders with multiwalled-carbon-nanotubes (MWCNTs) as conducting additives, and carbon coating on Si particles have shown positive effects on specific capacity and cycle performance [18, 19].

Numerous papers have also been published regarding phase changes and experimental determination of the maximum capacity of Si in Li-ion batteries. Based on their in situ XRD studies, M.N. Obrovac and L. Christensen suggested that when crystalline-Si is used as the starting material, the material initially passes through a two-phase region in which the surface of the particle forms amorphous Li_xSi with the core of the particle remaining crystalline. It is reported that after full lithiation of crystalline Si, it forms the thermodynamically unstable phase $\text{Li}_{15}\text{Si}_4$ (below 50 mV) showing $\sim 3579 \text{ mAh g}^{-1}$ [3, 11].

Many reports on phase transition of Li_xSi during Li insertion are based on X-ray diffraction, but there are very limited numbers of transmission electron microscopy (TEM) analyses reported due to the difficulty of sample

preparation [20, 21]. Our FIB apparatus with TEM sampling capability on selective areas enables the observation of atomic images of our electrode materials. Chemomechanical modeling is also employed in order to explain mechanical degradation resulting from stresses in the Li_xSi particles upon lithium insertion. Our observations and chemomechanical simulation provide important mechanistic insight for the design of advanced Li-ion battery materials.

2.2 FIB apparatus equipped with air-lock system

A focused ion beam (FIB, FEI NOVA200 dual beam system) equipped with an air-lock chamber (Figure 2.1) is used for TEM sample preparation. Ga ion source is used for FIB sectioning. The use of an air-lock system allows for accurate structural observation of Si composite electrodes. Typical observation equipment requires materials to be exposed to air for a brief period of time, allowing the highly reactive lithium/silicon materials to oxidize. The mobile air-lock system maintains a vacuum state while samples are loaded from glove box to FIB chamber preventing the air exposure to materials.

For the detailed observation of lithiated Si electrodes, TEM samples are prepared using our FIB air-lock system. As described in detail in Figure 2.2, the TEM samples are prepared from a free standing solid pellet. The solid state battery structure provides such an advantage that the Si composite electrode can be easily disassembled from the solid state battery without compromising the microstructural configuration of the composite electrode. All disassembling processes are carried out in a glove box.

Figure 2.2 shows a typical sample preparation sequence using FIB. The



Figure 2.1. FIB equipped with air-lock system and mobile chamber

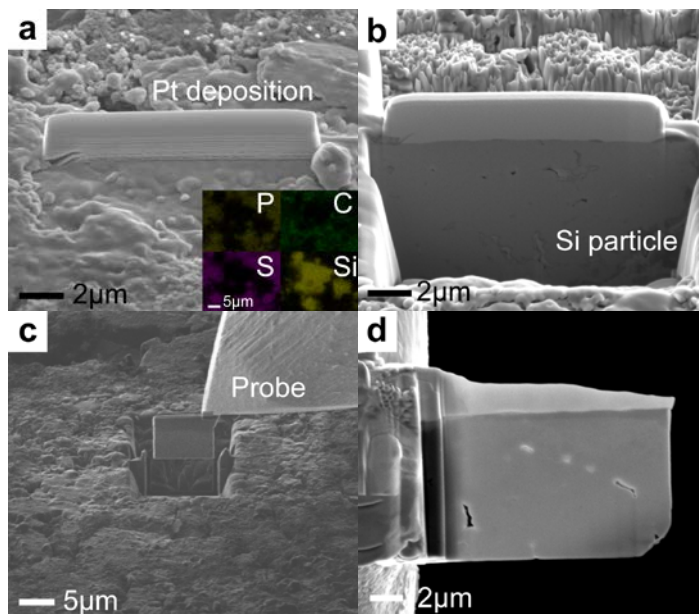


Figure 2.2. General sequence of producing TEM sample prepared by FIB. (a) Pt deposition for surface protection. (b) Cross sectioning of desired particle. (c) Sample lift out using manipulating probe. (d) Achieved TEM sample on Cu grid

SEM image in Figure 2.2a is a surface of composite electrode that contains Si, acetylene black and SSE. Pt deposition is used for the protection of desired surface area. Cross sectioning of the Li_2Si particle in Figure 2.2b is shown. A cross sectional sample of $10\ \mu\text{m} \times 5\ \mu\text{m} \times 0.1\ \mu\text{m}$ was produced using the lift-out technique (Figure 2.2c) and then attached to Cu TEM grid using a manipulating probe (100.7TM, Omniprobe). Further thinning of the sample with very careful beam condition of 10 kV and 30 ~ 50 pA was performed until a 50 - 90 nm thickness is achieved, which is the ideal condition for TEM observation (Figure 2.2).

There is a possibility that Pt electrochemically alloy with Li. So it is conceivable that lithium from the Si particle will be extracted into the Pt, especially at low voltages. However, when regarding molar volume (molar volume of Si is $12.05\ \text{cm}^3\ \text{mol}^{-1}$ and Pt is $9.09\ \text{cm}^3\ \text{mol}^{-1}$) and actual volume of diameter of $10\ \mu\text{m}$ Si particle and Pt deposition layer ($520\ \mu\text{m}^3$ of Si particle and $20\ \mu\text{m}^3$ of Pt layer), there are huge differences of containable number of Li atom per Si or Pt atom (The Si particle can hold about 20 times more Li than Pt layer). Therefore, Pt deposition on Li_xSi particle does not have serious problem on observe Li_xSi samples even though Pt layer takes away Li out of

Li_xSi particle because the amount of taken Li is negligible in whole Li_xSi particle. For example, if there is Li_2Pt layer on Li_2Si sample, from the molar volume of Si and Pt, the number of Si and Pt atoms can be calculated and the containable Li atom can be expected.

- Si atoms in particle: $520\mu\text{m}^3 \times (6.02 \times 10^{23}) / 12.05\text{cm}^3 = 260.8 \times 10^{11}$
- Li atoms in Li_2Si : 520×10^{11}
- Pt atoms in Pt layer: $20\mu\text{m}^3 \times (6.02 \times 10^{23}) / 9.09\text{cm}^3 = 13.24 \times 10^{11}$
- Li atoms in Li_2Pt : 26×10^{11}

If Li_2Pt is formed and Li_2Si loses that amount Li itself, composition ratio change is only from Li_2Si to $\text{Li}_{1.9}\text{Si}$ which is negligible for observation of Li_2Si .

2.3 Electrode samples preparation and XRD studies

Figure 2.3 shows the voltage profile and differential capacity of a crystalline Si anode in a solid state Li half cell construction. Si shows a long plateau at 0.1 V during Li insertion that indicates a two-phase reaction between crystalline Si phase and amorphous Li_xSi phase. Li reaction to Si is limited to 0.1 V and shown discharge capacity of 4153 mAh g^{-1} . During subsequent charging, the voltage goes up to 0.45 V sharply and shows a plateau illustrating a two-phase reaction between crystalline $\text{Li}_{15}\text{Si}_4$ phase and amorphous Li_xSi phase. A full discharge capacity of 4153 mAh g^{-1} at 0.01 V is partially resultant from side reactions at the beginning of discharge of which capacity should be excluded. An achievable charge capacity of $\sim 3553 \text{ mAh g}^{-1}$ after charging up to 1.5 V shows an irreversible capacity loss of $\sim 600 \text{ mAh g}^{-1}$ is due to side reactions. It is well known that the formation of a solid electrolyte interphase (SEI) can be responsible for large irreversible capacity losses during initial cycle. The SEM image of cross-sectioned Li_2Si sample (half way discharged) in Figure 2.4 supports the notion of side reactions and the formation of an SEI layer during lithiation of Si particles. The differential capacity curve versus voltage in Figure 1b with mirroring voltage profiles,

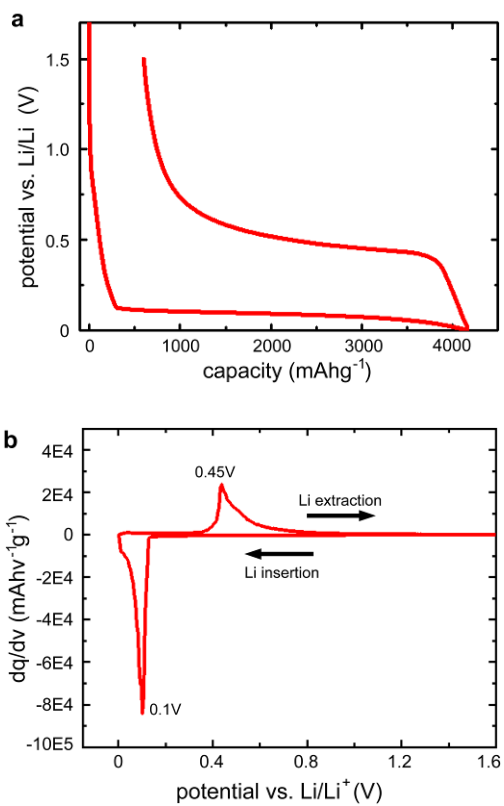


Figure 2.3. (a) Voltage profile of Si anode at voltage range of 0.01 V to 1.5 V.

(b) Corresponding differential capacity versus voltage curve.

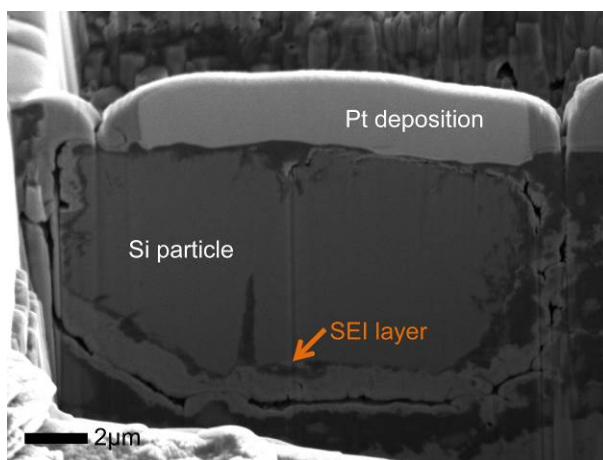


Figure 2.4. A cross sectional image of Si particle with SEI layer.

confirms that the long plateaus observed at 0.1 V during discharge and 0.45 V during charging represent two-phase reaction. It can be inferred that the peak at 0.45 V is a result of formation of a crystalline $\text{Li}_{15}\text{Si}_4$ phase when discharged down to 0.01 V.

It has been known that Si forms a two-phase region of crystalline Si and amorphous Li_xSi during Li insertion, and then forms the crystalline $\text{Li}_{15}\text{Si}_4$ phase at full discharge (at 30 mV) as shown in Figure 2.5. Therefore electrode samples corresponding to those regions were prepared for XRD and HRTEM observation. The first voltage-stop, corresponding to the two-phase region, is made at a discharge capacity of 1908 mAh g^{-1} (approximate nominal composition of Li_2Si at ~0.1 V) [15]. The second voltage-stop, for full lithiation status, is made at the discharge capacity of 4153 mAh g^{-1} (nominal composition of $\text{Li}_{4.4}\text{Si}$ at 0.01 V).

Figure 2.6 shows XRD patterns of crystalline Si phase in JCPDS, experimental Li_2Si and experimental $\text{Li}_{4.4}\text{Si}$. It turned out to be difficult to observe the amorphous phase by x-ray diffraction because of the background from the glass capillary tubes. Peaks other than those of crystalline Si phase can be seen in the Li_2Si sample. These peaks do not correspond to any Li_xSi

phase, but instead match peaks observed for the SSE, which is used in composite electrode fabrication [22, 23]. The XRD pattern for the fully lithiated sample (with nominal composition of $\text{Li}_{4.4}\text{Si}$) clearly shows the formation of a new phase after full discharge down to 0.01 V. All peaks of the fully lithiated Si sample are exactly matched with those of $\text{Li}_{15}\text{Si}_4$ phase initially reported by M. N. Obrovac and L. Christensen [6].

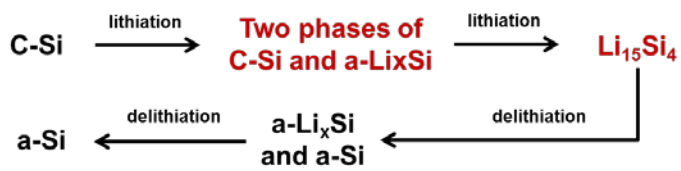


Figure 2.5. Proposed model that suggests how a single silicon particle changes its microstructure during cycling.

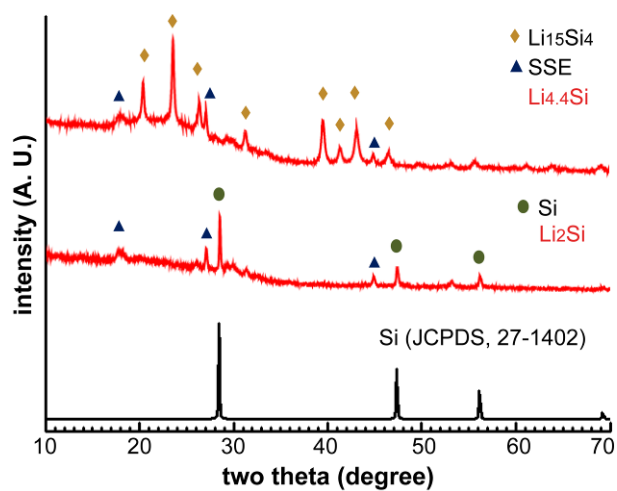


Figure 2.6. XRD patterns of crystalline Si phase in JCPDS, experimental Li_2Si and experimental $\text{Li}_{4.4}\text{Si}$.

2.4 HRTEM observation on electrode samples

Figure 2.7a shows the bright field (BF) TEM image of the one single Li_2Si particle sample which has been known to exhibit a two-phase region [11]. Energy dispersive X-Ray spectroscopy (EDS) measurement shown in inset of Figure 2.7a reveals that samples are mostly composed of Si, with a small amount of Cu detected. No signal from oxygen is detected, which implies that the TEM sample is never exposed to air. It is observed that the majority of the surface (which contacts the Pt) is amorphous phase while the inside area of the particle is filled with crystalline. HR images and FFTs in Figure 2.7b and Figure 2.7c support that each area is formed with amorphous and crystalline Si phase (along [112] zone axis), respectively. This confirms that a two-phase region is formed with amorphous Li_xSi at the surface and crystalline Si phase in the core of particle as previously proposed.[11] As shown in Figure 2.7a, amorphization due to Li insertion in Si begins from the surface. While it is widely accepted that amorphous Li_xSi initially forms at the surface with crystalline Si being maintained in the core of particles, there has never been precise observation of this phenomenon using TEM. Here, a Li_xSi particle maintaining a crystalline core with amorphization at the surface

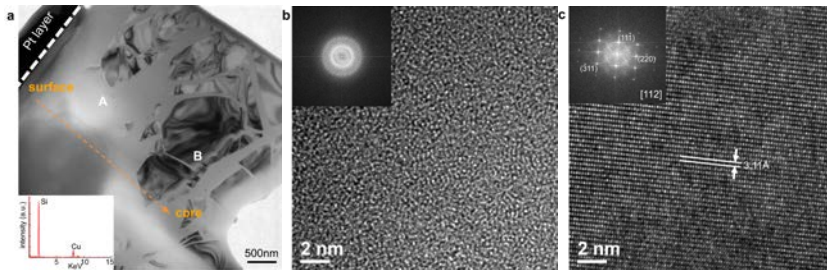


Figure 2.7. TEM images of Li_2Si . (a) BF image of Li_2Si . (b) HR and corresponding FFT of area A indicates that amorphous. (c) HR and corresponding FFT of area B indicates that Si crystalline phase along the [112] direction.

during Li insertion is confirmed. This observation also infers that Li concentration in the Si particle is surface dominant which explains mechanical failure of Si anodes upon Li insertion.

Thermodynamically stable Li-Si crystalline phases such as $\text{Li}_{12}\text{Si}_7$, Li_7Si_3 and $\text{Li}_{13}\text{Si}_4$ are not shown in this region because the energy barrier for nucleation which is combined with surface and volume energy of nucleus, is higher when it is about to nucleate and thus makes meta-stable amorphous Li_xSi [24, 25].

Figure 2.8 shows the BF image of a fully lithiated Si sample having a high concentration of pores. Each pores and dense area can be recognized by strong and weak contrast, respectively, as direct beam have transmitted different mass thickness of a particle sample. It is observed that porosity in the Si particle shown has a more pronounced concentration toward the inner-particle area. A large variety and number of pores are observed in the core area of the particle, while towards the surface, pores appear relatively smaller in size and fade in number. We attribute the pore formation parallel to the surface to tensile stress which is applied normal to the surface of Si particles. Cracks are expected to initiate from these pores as a result of mechanical

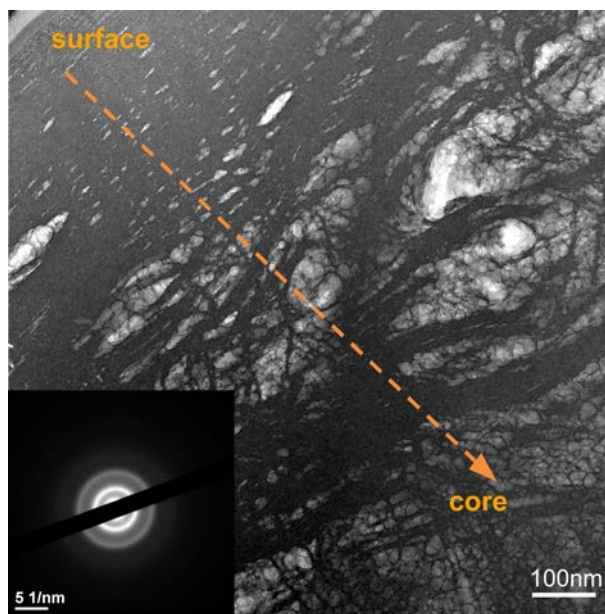


Figure 2.8. BF image and corresponding diffraction pattern of $\text{Li}_{4.4}\text{Si}$.

stresses caused by volume expansion upon Li insertion to Si particles. We have employed chemomechanical modeling for further support these findings and mechanical degradation and simulation results are discussed in detail in Figure 2.9.

The diffusive ring pattern of SAED in the inset of Figure 2.8 shows that the area under investigation is amorphous phase. This result conflicts with our XRD study previously discussed in Figure 2.6, as it was revealed that fully lithiated Si anodes yield similar results to previous research with crystalline $\text{Li}_{15}\text{Si}_4$ phase in particles. It is proposed that the reason for observation of amorphous-only phase is that Ga has stronger binding energy towards Li than Si, so Ga ion bombardment to Li_xSi sample likely remove Li ion out of Li_xSi . [26]

2.5 Chemomechanical simulation

Chemomechanical modeling was employed to simulate the stresses experienced by Si electrode particles during lithiation in an effort to gain insight as to what causes the observed porosity pattern in lithiated Si electrodes. Figure 2.9 shows the stress and Li concentration profiles of lithiation of Si particles. r/R_{out} indicates the radius of a Si particle, $r/R_{out} = 0$ refers to the center of a particle, and $r/R = 1$ is the surface of particle. Radial stress profiles show highly concentrated stress at the core of Si during the beginning of lithiation ($t = 100s, 230s, \text{ and } 1000s$).^[27] In this stage, as shown in Figure 2.7, there is a lithium concentration difference between the core, which remains as crystalline Si, and surface, which turns from crystalline to amorphous Li_xSi . The surface which is made up of Li_xSi expands outward while the core remains static and without lithiation. A concentration difference along r/R_{out} of tangential stress profile in Figure 2.9b is the result of these two different phase areas have different swelling behavior. As the concentration increases in the material near the surface, it swells with respect to the material near the center of the particle, i.e., there is a mismatch in strain. Material just inside the surface that has yet to swell constrains material at the

surface from swelling freely, which results in tensile stress near the center of the particle. This stress concentration also accounts for Figure 2.8 which shows high porosity concentration towards to core of Si. It is shown that pores in Si result from tensile stress during lithiation and pore concentration grows towards to core of particles.

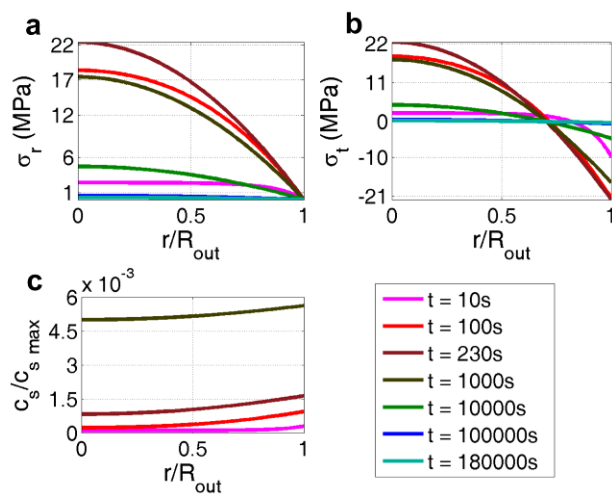


Figure 2.9. Generated stress concentration profiles during Li insertion. (a)

Radial stress. (b) Tangential stress. (c) Li ion concentration

2.6 Conclusion

In this work, we observed microstructural transformations of lithiated Si anodes in all-solid-state Li half cells. XRD analysis was performed to observe the phase variation of Si samples during Li insertion. It was shown that crystalline Si undergoes amorphization during lithiation and forms a crystalline phase after full discharge, known as $\text{Li}_{15}\text{Si}_4$. Two-phase regions were observed by HRTEM showing amorphous Li_xSi at the surface and crystalline Si phase at the core of particles for the first time. HRTEM observation of fully discharged Si anode samples revealed that particles consisting of high concentrations of pores in the Si particle are responsible for cracks and pulverization of Si during Li insertion. The chemomechanical modeling was employed to explain the generated stresses during Li insertion in relation to observed porosity pattern in detailed TEM study.

2.7 Materials and Methods

All solid state Si half cells were prepared for these experiments. Li_2S (Aldrich, 99.999%) - P_2S_5 (Aldrich, 99%) at a molar ratio of 77.5:22.5 respectively, is used as a solid state electrolyte (SSE). These starting materials were combined into a stainless steel vial and planetary ball milling was carried out for 20 continuous hours.[18] Composite electrode materials are made up of crystalline bulk Si powders (Alfa-Aesar, 99%, -100mesh), acetylene black (Alfa-Aesar, 50% compressed) and SSE $\text{Li}_2\text{S-P}_2\text{S}_5$ at a weight ratio of 1: 1: 5 respectively.[12] Si powder is annealed at 900°C for 5 hours under Ar atmosphere to remove any undesired defects. A bi-layer pellet was made with 5 mg of composite electrode on the top of 200 mg of SSE powder at 5 ton. Li foil is attached to opposite side of the SSE at 1 ton, as shown in Figure 2.9. All pressing and testing operations were carried out with Ti metal bodies as current collectors for both working and counter electrodes and also covered by a poly (aryl ether ether ketone) mold ($\Phi = 1.3$ cm). All processes including assembly and testing of all-solid-state batteries was carried out in Ar-filled glove box.

The microstructure of Li_xSi phases was investigated by HR-TEM (JEOL

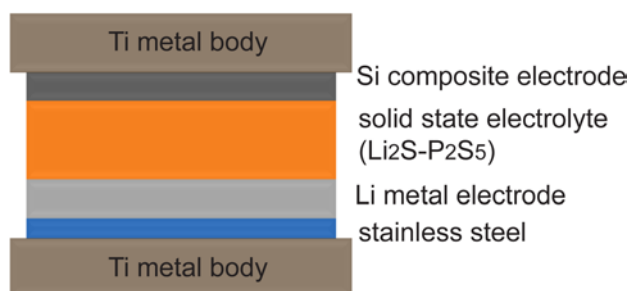


Figure 2.10. A schematic of all solid state Li ion battery in Ti metal test die.

3000F) operating at 300 keV and Gatan, Digital Micrograph software was used for analysis of selected area electron diffraction (SAED) and fast Fourier transform (FFT). XRD data for phase determination was collected with X-ray diffractometer (XRD, Bruker, D8 Advance) with Cu-K α radiation. An air tight capillary holder was used to prevent any possible reactions between the Li_xSi electrode samples and air during XRD measurement.

The finite element method was employed to simulate the stresses experienced by Si electrode particles during Li insertion. The model including material properties described in our previous study [27, 28] is used for the simulations performed. Experiments performed were current controlled, so instead of modeling the surface reaction kinetics the surface Li flux is prescribed to balance the in the applied current in the experiments. Modeling employed a constant Li flux at the surface to balance the applied current in the experiments.[22] In the experiments, 70 μ A of current is applied to a half cell with a particle/electrolyte interface area of 1.3273 cm², which corresponds to $j_s = 5.466e^{-6}$ mol m⁻²s⁻¹ of Li ion flux across the electrode / electrolyte interface where F is Faraday's constant. Figure 2.11 is a schematic of the electrode particle model. A 1 μ m sphere particle is simulated with the specified

flux, j_s , applied to the sphere surface, Γ_{sj} , for 5 hours, which is the amount of time required to reach about 95% utilization. The sphere is idealized as perfectly symmetric, and is discretized with 60 evenly sized three node bar elements. Stress distributions within the simulated particle are plotted for various times in order to facilitate a discussion on the stresses experienced by Si electrode particles during Li insertion.

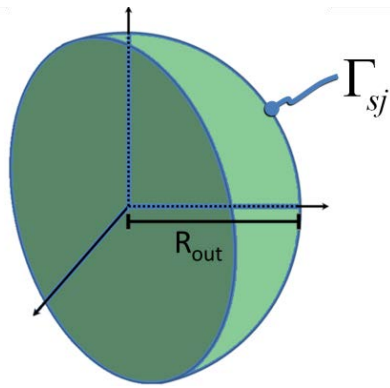


Figure 2.11. A schematic of the electrode particle model.

2.8 References

- [1] J. M. Tarascon, M. Armand, *Nature* **2001**, 414, 359.
- [2] S. D. Beattie, D. Larcher, M. Morcrette, B. Simon, J. M. Tarascon, *J. Electrochem. Soc.* **2008**, 155, 158.
- [3] M. N. Obrovac, L. Christensen, *Electrochem. Solid State Lett.* **2004**, 7, 93.
- [4] W. J. Weydanz, M. Wohlfahrt-Mehrens, R. A. Huggins, *J. Power Sources* **1999**, 81, 237.
- [5] J. R. Dahn, T. Zheng, Y. Liu, J. S. Xue, *Science* **1995**, 270, 590.
- [6] Y. Wang, J. Dahn, *J. Electrochem. Soc.* **2006**, 153, A2314
- [7] T. D. Hatchard, J. R. Dahn, *J. Electrochem. Soc.* **2004**, 151, A838.
- [8] Y. M. Kang, S. B. Suh, Y. S. Kim, *Inorg. Chem.* **2009**, 48, 11631.
- [9] S. Golmon, K. Maute, S. H. Lee, M. L. Dunn, *Appl. Phys. Lett.* **2010**, 97, 033111.
- [10] L. Y. Beaulieu, K. W. Eberman, R. L. Turner, L. J. Krause, J. R. Dahn, *Electrochem. Solid State Lett.* **2001**, 4, A137.
- [11] M. N. Obrovac, L. J. Krause, *J. Electrochem. Soc.* **2007**, 154, A103
- [12] J. Trevey, J. S. Jang, Y. S. Jung, C. R. Stoldt, S. H. Lee, *Electrochem. Comm.* **2009**, 11, 1830.

- [13] R. Deshpande, Y. Qi, Y. T. Cheng, *J. Electrochem. Soc.* **2010**, 157, A967.
- [14] V. B. Shenoy, P. Johari, Y. Qi, *J. Power Sources* **2010**, 195, 6825.
- [15] C. K. Chan, R. Ruffo, S. S. Hong, R. A. Huggins, Y. Cui, *Nat. Nanotechnology*. **2007**, 3, 31.
- [16] A. Magasinski, P. Dixon, B. Hertzberg, A. Kvit, J. Ayala, G. Yushin, *Nat. Mater.* **2010**, 9, 353.
- [17] J. Cho, *J. Mater. Chem.* **2010**, 20, 4009.
- [18] J. E. Trevey, K. W. Rason, C. R. Stoldt, S. H. Lee, *Electrochem. Solid State Lett.* **2010**, 13, A154.
- [19] J. Xiao, W. Xu, D. Wang, D. Choi, W. Wang, X. Li, G. L. Graff, J. Liu, J. G. Zhang, *J. Electrochem. Soc.* **2010**, 157, A1047.
- [20] J. Y. Huang, L. Zhong, C. M. Wang, J. P. Sullivan, W. Xu, L. Q. Zhang, S. X. Mao, N. S. Hudak, X. H. Liu, A. Subramanian, H. Fan, L. Qi, A. Kushima, J. Li, *Science*. **2010**, 330, 1515.
- [21] X. H. Liu, L. Q. Zhang, L. Zhong, Y. Liu, H. Zheng, J. W. Wang, J. H. Cho, S. A. Dayeh, S. T. Picraux, J. P. Sullivan, S. X. Mao, Z. Z. Ye, J. Y. Huang, *Nano Letters* **2011**, 11, 2251.
- [22] S. Golmon, K. Maute, M. L. Dunn, *Comput Struct* **2009**, 87, 1567.

- [23] J. E. Trevey, J. Wang, C. M. Deluca, K. K. Maute, M. L. Dunn, S. H. Lee, V. M. Bright, *Sensor Actuator Phys* **2011**, 167, 139.
- [24] J. E. Trevey, Y. S. Jung, S. H. Lee, *J. Power Sources* **2010**, 195, 4984
- [25] A. Hayashi, S. Hama, H. Morimoto, M. Tatsumisago, T. Minami, *J. Am. Ceram. Soc.* **2001**, 84, 477.
- [26] W. J. Zhang, *J. Power Sources* **2011**, 196, 877.
- [27] P. Limthongkul, Y.-I. Jang, N.J. Dudney, Y.-M. Chiang, *Acta Materialia* **2003**, 51, 1103.
- [28] V. L. Chevrier, J. W. Zwanziger, J. R. Dahn, *J. Alloy. Comp.* **2010**, 496, 25.

Chapter 3: A highly reversible nano-Si anode enabled by mechanical confinement in an electrochemically activated $\text{Li}_x\text{Ti}_4\text{Ni}_4\text{Si}_7$ matrix

3.1 Introductions

Traditionally an important additive in manufacturing, Si is becoming an ever more popular material in commercial use. The backbone of the semiconductor industry, Si is in virtually all electronic devices. Recently, Si, especially nano-Si, has received extra attention due to advances and prospects in the energy storage market. Si is the primary material in solar cells. As both a thin film and as a bulk wafer, Si is currently the most efficiency material on the market. But, while research continues to improve the efficiency of commercial solar cells, consumers are still unable to store the energy that is not immediately used making solar cell advancements unmarketable and costly. Likewise, as gas prices rise and consumers look to purchase hybrid electric (HEV) and electric vehicles (EV), many are deterred by the high cost and the short driving ranges. The most promising solution to current battery shortfalls is nano-Si [1-4].

In order to deploy Li-ion batteries in electric vehicles, it is essential to develop durable electrodes with high energy density and high power. The utilization of Si is also advantageous because it is non-toxic and the 2nd most abundant element in the Earth's crust [5, 6]. However, Si has yet to be commercialized because it undergoes a volume expansion of 300% with the insertion of 3.7 mole Lithium (Li) per mole of Si. Such a large volume expansion results in mechanical fatigue which causes rapid capacity fade and continually subjects fresh Si surfaces to the parasitic reduction of liquid electrolyte. Poor coulombic efficiency (CE) arises from the formation of a solid electrolyte interphase (SEI). The problem of rapid capacity fade and low CE must be solved before Si can be adopted as an anode in commercial LIBs [7-10].

The development of Si anodes is primarily concerned with two tasks: First, with how to mitigate stress evolution in Si particles during Li insertion and extraction. And second, with how to maintain a high CE over many cycles. Previous research has shown that nano-structured Si electrodes composed of Si nano-particles, Si nano-wires or Si nano-alloys can better accommodate the stresses generated during cycling. Nano-Si electrodes also have better reaction

kinetics because Li-ion diffusion pathways are shortened compared to the bulk^[11-17]. Interesting prelithiation strategy has also been reported to improve the cycling performance of nano electrode materials [18, 19]. However, nano-structured Si electrodes tend to be expensive to fabricate because the synthesis of many of these materials requires chemical or physical vapor deposition. For this reason, the aforementioned technologies are not suitable for large scale manufacture to meet commercial demand.

3.2 Previous study with carbon coating on nano-Si

Carbon coating on the surface of particle is widely used method for electrode materials in LIBs. Carbon coating on the Si particle mainly take three advantages. First, coating on the surface prevents the volume expansion and mechanical failure of Si upon Li insertion/extraction. Second, coating protects the exposure of Si surface and SEI layer formation. And last, carbon on the surface can enhance the sluggish kinetics of Si particle. In this sense we have applied carbon coating on nano-Si using polyacrylonitrile (PAN) polymer. Figure 3.1 shows a TEM-EELS image of conformal thin coating (~ 5 nm) of carbon coating (cyan) on nano-Si particles (red). The coating provides an intimately linked conductive network that connects nano-Si particles throughout the electrode and also increases the mechanical stability during cycling.

Figure 3.2 describes electrochemical properties of PAN-carbon coating on nano-Si electrode. The electrode was run at a rate of C/20 for the first 10 cycles and a rate of C/10 for all subsequent cycles. At cycle 150, our PAN-Si electrode exhibits a specific charge capacity of nearly 1500 mAh g^{-1} with a CE approaching 100%. Such good cycle life and CE is evidence that the PAN

coating has good mechanical resiliency. Figure 3.2b displays the 1st, 3rd, 10th, 30th, 40th, and 50th voltage profiles of our PAN-Si anode. The first cycle profile shows a specific charge capacity of 2585 mAh g^{-1} , which is equivalent to the extraction of 2.7 mole Li per mole of Si. At cycle 50, the specific charge capacity is 2078 mAh g^{-1} (2.2 mole Li).

This study shows us a way to improve the cycle stability of Si anode but also remains the problems to be solved. Using a nano sized Si is helpful to reduce the generated stress during cycling with increased kinetics due to shortened diffusion length. However fabrication or synthesis of nano sized Si is too expensive to apply in commercial LIBs. We also observed gradual capacity loss of PAN-Si electrode during cycling mainly caused by loss of active materials.

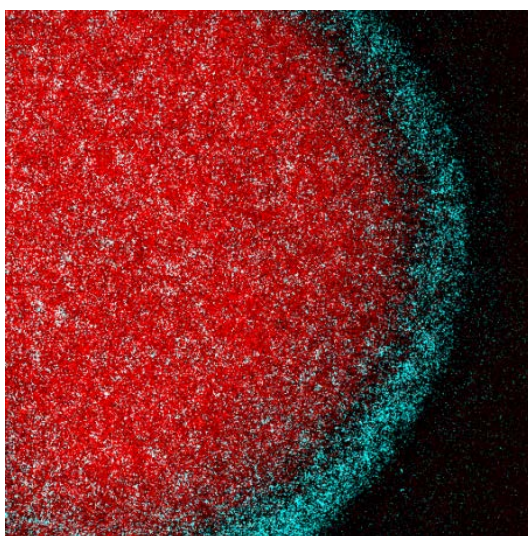


Figure 3.1. TEM-EELS elemental mapping confirming that we achieve a conformal 5 nm thick PAN-carbon coating. (Cyan: Carbon, Red: Silicon)

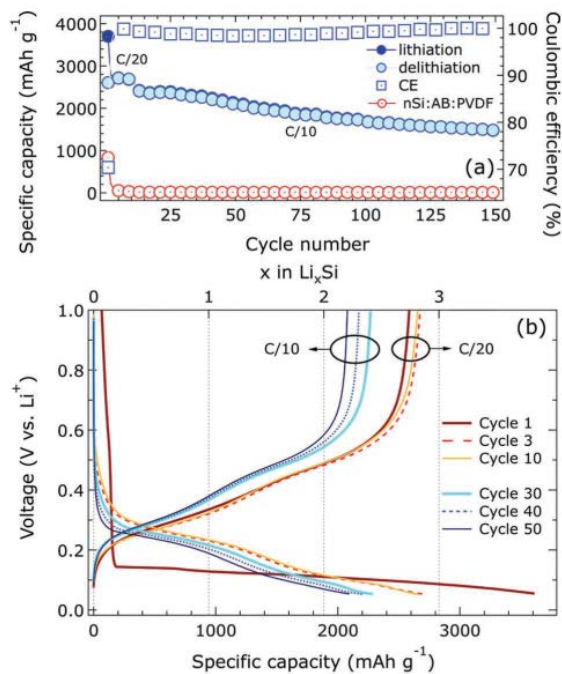


Figure 3.2. (a) Cyclic capacity (blue circles) and CE (blue squares) of PAN-Si electrodes run at a rate of C/20 for the first 10 cycles and at C/10 for subsequent cycles. A conventional nano-Si electrode (red circles) was cycled at a rate of C/10 as a control cell. After 150 cycles, our PAN-Si composite electrode has a specific charge capacity of nearly 1500 mAh g⁻¹ and a CE approaching 100%, whereas the conventional electrode fails after 3 cycles. (b) Voltage profiles of our nano-Si/cyclized-PAN electrode showing a minimal overpotential when cycled at C/10 compared to C/20.

3.3 Synthesis of Si-Ti-Ni alloy: Mechanical confinement

We have developed the Si-Ti-Ni (here after denoted as STN) ternary alloy to answer the call for a low-cost, high capacity anode with a high CE and good capacity retention. STN alloy has been initially designed by SAMSUNG SDI (Patent KR 2007-0027775) to confine volume expansion of Si upon Li insertion in Ti-Ni (Nitinol) shape memory alloy matrix. (And later this chapter we provide that nano-Si is not embedded in Nitinol but $\text{Ti}_4\text{Ni}_4\text{Si}_7$ matrix.)

To synthesize the STN alloy, we use melt spinning to embed nano-Si particles in a matrix of $\text{Ti}_4\text{Ni}_4\text{Si}_7$. We chose the melt spinning method because it is inexpensive and can be implemented at standard temperature and pressure. Melt spinning is an established process used to synthesize alloys by rapidly solidifying molten metal solutions at a rate of 10^4 to 10^7 K s^{-1} . Examples of materials synthesized by melt spinning include polymeric fibers, magnetic alloys, and shape memory alloys [20-23]. Our STN alloy's exceptional performance and ease of manufacture makes it an attractive prospect for commercialization in advanced LIBs. Our characterization of STN alloy anode also provides important mechanistic insight for the development of

advanced anode materials for LIBs.

Figure 3.3a depicts a simplified schematic of the melt spinner used in this study. Melt spun STN ribbons are on average less than 1mm wide and 15 μ m thick (Figure 3.3b). Powder X-ray diffraction (XRD) analysis was performed to determine the phases present in the STN alloy (Figure 3.3c). We find that the STN alloy is composed of crystalline Si (JCPDS, 27-1402) and $\text{Ti}_4\text{Ni}_4\text{Si}_7$ (JCPDS, 80-1015) [24]. The $\text{Ti}_4\text{Ni}_4\text{Si}_7$ phase was previously reported by J. H. Westbrook et al., however, its electrochemical properties have not yet been reported to the best of our knowledge [25]. We used the Rietveld method to analyze XRD patterns and calculate the relative ratio of the component phases in our STN alloy. Table 3.1 provides the information used for the Rietveld method analysis. The result informs us that the Si and $\text{Ti}_4\text{Ni}_4\text{Si}_7$ phases take possession of 46 and 54 weight percent (wt %) of the STN alloy respectively.

As shown in Figure 3.3d, high resolution transmission electron microscopy (HRTEM) analysis was performed using the high angle annular dark field (HAADF) mode to observe the microstructure of the STN alloy in detail. It is observed that the structure is composed of two different compositions which are Si (weak contrast) and $\text{Ti}_4\text{Ni}_4\text{Si}_7$ (strong contrast).

We find that our STN ternary alloy is composed of 20-50 nm diameter Si nano particles embedded in a $\text{Ti}_4\text{Ni}_4\text{Si}_7$ matrix. Rapid solidification from the molten state only allows for the formation of nano sized Si. The remaining melt portion then forms the $\text{Ti}_4\text{Ni}_4\text{Si}_7$ matrix. Additional energy dispersive spectroscopy (EDS) results presented in Figure 1e support the conclusion that the STN alloy is composed of nano-Si and $\text{Ti}_4\text{Ni}_4\text{Si}_7$.

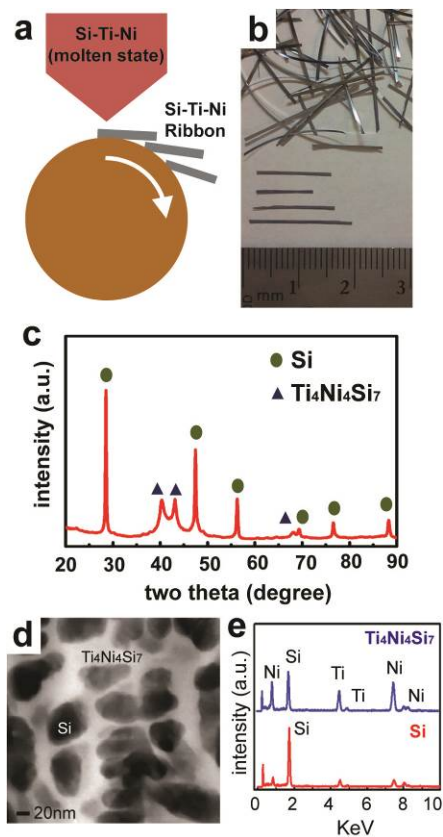


Figure 3.3. (a) Simplified schematics of melt spinner. (b) Achieved melt spun STN ribbon. (c) XRD pattern of ball milled melt spun STN powder that matched with Si phase (JCPDS, 27-1402) and $\text{Ti}_4\text{Ni}_4\text{Si}_7$ phase (JCPDS, 80-1015). (d) TEM image with HAADF mode of nano-Si and $\text{Ti}_4\text{Ni}_4\text{Si}_7$. (e) EDS results of given area in Figure 3.1d.

Phase			Si		
Space Group			Fd-3mS		
a	b	c	α	β	γ
5.43Å	5.43Å	5.43Å	90.0	90.0	90.0
Atom		Site	x	y	z
Si		8a	0	0	0

Phase			Ti ₄ Ni ₄ Si ₇		
Space Group			I4/mmm		
a	b	c	α	β	γ
12.52Å	12.52Å	4.93Å	90.0	90.0	90.0
Atom		Site	x	y	z
Ti 1		8h	0.13519	0.13519	0
Ti 2		8j	0.6898	0.5	0
Ni 1		16k	0.1495	0.64946	0.25
Si 1		8h	0.29358	0.29358	0
Si 2		8i	0.2925	0	0
Si 3		8j	0.9083	0.5	0
Si 4		4e	0	0	0.25

Table 3.1. Space groups, lattice constants and atomic positions of Si and

Ti₄Ni₄Si₇. Information in Table 3.1 is used for Rietveld method of STN alloy.

Rietveld method shows that STN is 46 wt % Si and 54 wt % Ti₄Ni₄Si₇.

3.4 Electrochemical properties of Si-Ti-Ni

Constant current - constant voltage (CCCV) discharge-charge tests were conducted to characterize the electrochemical properties of the STN alloy. Cells were cycled at a rate of 0.1C for the first cycle, 0.2C for the second cycle and 1C for all subsequent cycles (1C rate corresponds to 0.88 mA cm^{-2}). This cycling with gradual C-rate increase is typical way for continuous discharge-charge experiment in Li ion battery and specially STN alloy needs to be ran at slower rate in its initial cycling because nano-Si is covered by $\text{Ti}_4\text{Ni}_4\text{Si}_7$ matrix and this makes hard for Li ion to go through the $\text{Ti}_4\text{Ni}_4\text{Si}_7$ matrix and alloy with nano-Si. The STN alloy delivers an initial discharge and charge capacity of 1325 mAh g^{-1} and 1158 mAh g^{-1} respectively (Figure 3.4a). While the first cycle has a CE of 87.7%, by the 10th cycle our STN alloy exhibits a CE of 99.7%. To the best of our knowledge, a CE this high is rarely reported for Si based anode materials [14, 26-29]. The STN alloy also has a stable capacity and exhibits a discharge capacity of 900 mAh g^{-1} by the 50th cycle. Considering that Si is known for its slow diffusion kinetics, it is remarkable that such a high CE and specific capacity are both possible at a rate of 1C.

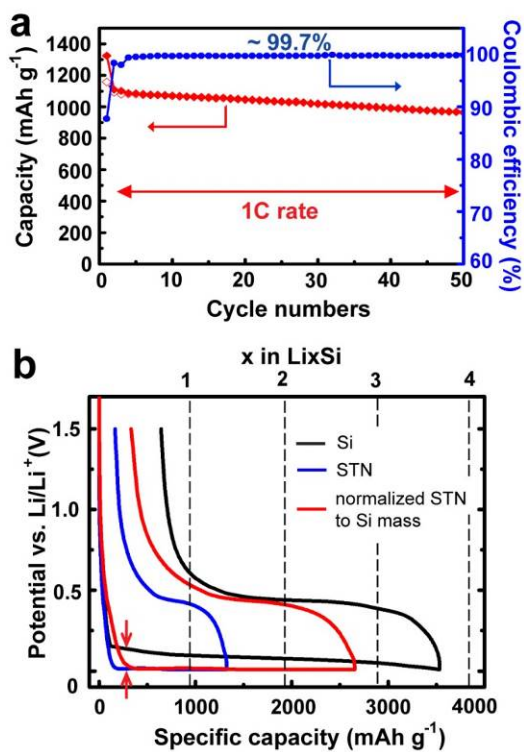


Figure 3.4. (a) Specific capacity and CE of STN anode versus cycle numbers.

(b) Voltage profile of Si, STN and normalized STN to Si mass between 0.01 V and 1.5 V.

Figure 3.4b presents the initial voltage profiles (versus specific capacity and x in Li_xSi) of Si and the STN alloy. To compare the lithiation extent of Si and the STN alloy, we also plot the voltage profile of the STN alloy normalized to Si mass. It is important to make this comparison because the STN alloy is composed of 46 wt% of the Si phase and 54 wt% of the $\text{Ti}_4\text{Ni}_4\text{Si}_7$ phase. The phase fraction, and not the elemental fraction of Si, should be considered for this comparison because the $\text{Ti}_4\text{Ni}_4\text{Si}_7$ phase contains Si that does not readily alloy with Li. For this reason, we used our previous Rietveld analysis results to normalize the STN alloy to the mass of the nano-Si phase.

We observe that the discharge plateau of our STN alloy anode occurs at a lower voltage than that of the Si anode. This overpotential is indicated by arrows in Figure 3.4b. It has been reported that a compressive stress imparted upon Si particles can lower the discharge voltage plateau [30]. In this case, the $\text{Ti}_4\text{Ni}_4\text{Si}_7$ matrix of our STN alloy confines the free volume expansion of the embedded nano-Si particles during Li insertion. Mechanical confinement provided by the $\text{Ti}_4\text{Ni}_4\text{Si}_7$ matrix therefore limits the extent of Li insertion and manifests itself as the observed overpotential. To support this conclusion, we infer that the degree of volume expansion is directly related to the degree

of lithiation of the fully discharged state. We find that the normalized STN alloy accommodates 2.7 mole Li-ions per mole of nano-Si, while unconfined bulk Si accommodates 3.7 mole Li-ions per mole of Si. The $\text{Ti}_4\text{Ni}_4\text{Si}_7$ matrix contributes to the mechanical stability of nano-Si particles by decreasing the maximum stress generated during Li insertion and extraction. We believe that the reason nano-Si only accommodates 2.7 mole Li-ions per mole is nano-Si is covered by $\text{Ti}_4\text{Ni}_4\text{Si}_7$ matrix and this matrix apply compressive stress to nano-Si. Under compressive stress, volume of nano-Si is hard to expand as it supposed to and this cause limited Li-ion accommodation of nano-Si. We have mentioned this in our manuscript. We will soon show that the $\text{Ti}_4\text{Ni}_4\text{Si}_7$ matrix is electrochemically active. Our calculation of 2.7 mole Li per mole Si already takes this finding into account.

There is not enough evidence to prove the $\text{Li}_x\text{Ti}_4\text{Ni}_4\text{Si}_7$ matrix helps to reduce the formation of an SEI layer on the Si surface. However, from the fact that lots of numbers of nano-Si is covered by $\text{Ti}_4\text{Ni}_4\text{Si}_7$ matrix and help not to exposed by liquid electrolyte directly, we asserts that having less surface area caused by $\text{Ti}_4\text{Ni}_4\text{Si}_7$ matrix coating is helpful to reduce the SEI layer formation.

3.5 Ionic conductivity measurement of $\text{Ti}_4\text{Ni}_4\text{Si}_7$ matrix

The observed overpotential between Si and STN may also indicate that the reduction of Si is limited by the diffusion of Li-ions in the $\text{Ti}_4\text{Ni}_4\text{Si}_7$ matrix. To examine this issue we investigated the electrochemical properties of the $\text{Ti}_4\text{Ni}_4\text{Si}_7$ matrix. A $\text{Ti}_4\text{Ni}_4\text{Si}_7$ ingot was prepared and ball milled for the purpose of electrochemical characterization in a half cell configuration. Figure 3a presents the voltage profile (versus specific capacity) for the $\text{Ti}_4\text{Ni}_4\text{Si}_7$ cycled with a current density of 50mA g^{-1} . It shows that $\text{Ti}_4\text{Ni}_4\text{Si}_7$ is electrochemically active versus Li and provides a limited reversible capacity. However, only 55% of the first discharge capacity was reversible. After the first cycle, the composition of $\text{Ti}_4\text{Ni}_4\text{Si}_7$ is better represented by $\text{Li}_x\text{Ti}_4\text{Ni}_4\text{Si}_7$. After the 20th charge, the $\text{Ti}_4\text{Ni}_4\text{Si}_7$ half cell was disassembled to prepare a sample for TEM analysis. The TEM sample was never exposed to air because our focused ion beam (FIB) apparatus is equipped with an air-lock chamber. (See Figure 3.5 for a detailed TEM sample preparation sequence using FIB). Electron energy loss spectroscopy (EELS) mapping of $\text{Ti}_4\text{Ni}_4\text{Si}_7$ (Figure 3.6) indicates that Li is distributed throughout $\text{Ti}_4\text{Ni}_4\text{Si}_7$. This evidence supports our assertion that irreversible Li-ion loss is attributed to the

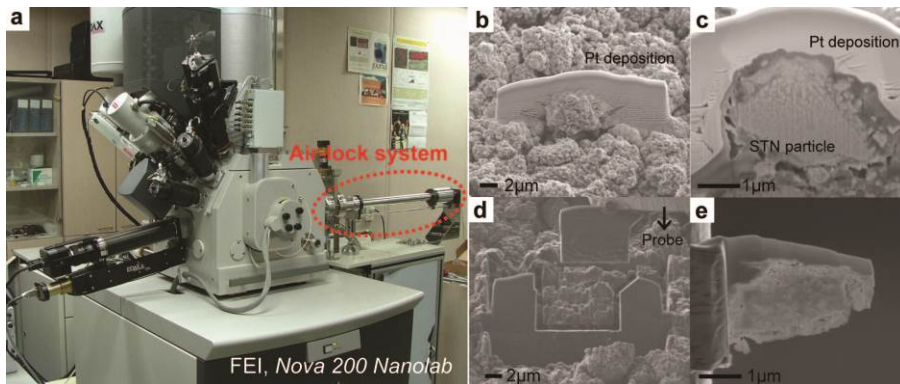


Figure 3.5. FIB equipped with air-lock system and the general TEM sample preparation sequence using the FIB. (a) FIB equipped with autonomously developed air-lock system. (b) Pt deposited to protect particle surface. (c) Cross sectioning of desired STN particle. (d) Sample lift out using manipulating probe. (e) Achieved TEM sample on Cu grid.

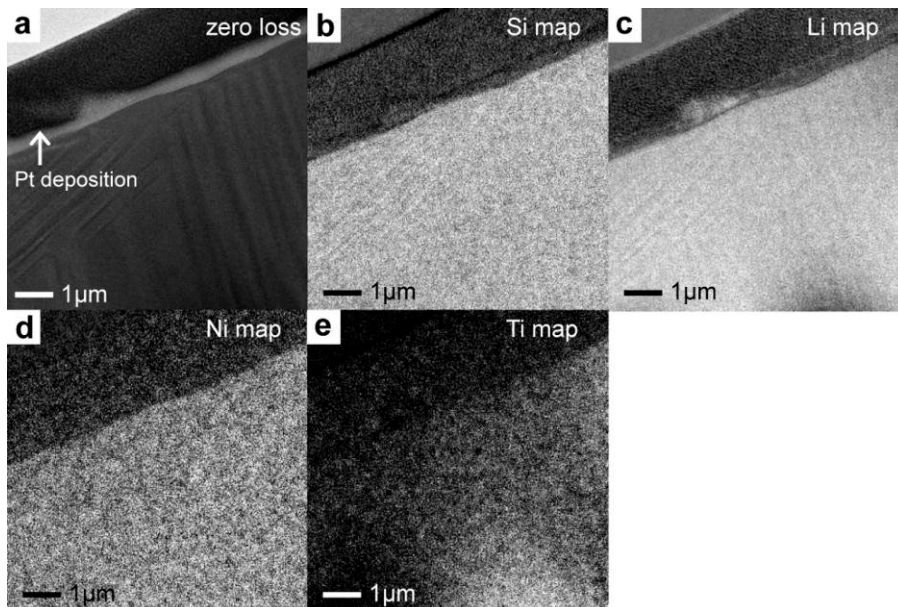


Figure 3.6. TEM EELS mapping results of $\text{Ti}_4\text{Ni}_4\text{Si}_7$ electrode after 20th cycle. Strong contrast in given area infers that corresponding element is detected. (a) Zero loss. (b) Si map result. (c) Li map result. (d) Ni map result. (e) Ti map result.

compositional change of $Ti_4Ni_4Si_7$ to $Li_xTi_4Ni_4Si_7$.

To confirm the electrochemical activity of $Ti_4Ni_4Si_7$ in the STN alloy we analyzed differential capacity (dQ/dV) data. Figure 3.7b presents the initial dQ/dV of the STN alloy (red) versus that of $Ti_4Ni_4Si_7$ (blue). During discharge, the STN alloy exhibits a reduction peak at 0.066V while $Ti_4Ni_4Si_7$ exhibits a reduction peak at 0.077 V. The close proximity of these peaks indicates that the reduction of $Ti_4Ni_4Si_7$ also occurs in the STN alloy. Two closely related oxidation peaks during charging also confirm the electrochemical activity of $Ti_4Ni_4Si_7$ in the STN alloy.

Because the first cycle of the $Ti_4Ni_4Si_7$ half cell exhibited the most irreversibility, it is likely that the electrochemical performance of STN is related to $Li_xTi_4Ni_4Si_7$ instead of $Ti_4Ni_4Si_7$. To study the properties of $Li_xTi_4Ni_4Si_7$ in more detail, we calculated x using the irreversible capacity of the $Ti_4Ni_4Si_7$ half cell presented in Figure 3.7a and b. We find an irreversible capacity of 137 mAh g^{-1} between the 1st and 20th cycles. Assuming a Faradaic reaction, we used equation (1) to calculate x to equal 3.2.

$$x = \frac{0.137Ah}{g_{Ti_4Ni_4Si_7}} \times \frac{\text{molecular weight of } Ti_4Ni_4Si_7}{mol_{Ti_4Ni_4Si_7}} \times \frac{mol e^-}{26.8Ah} = \frac{3.2 mol Li^+}{mol_{Ti_4Ni_4Si_7}} \quad (1)$$

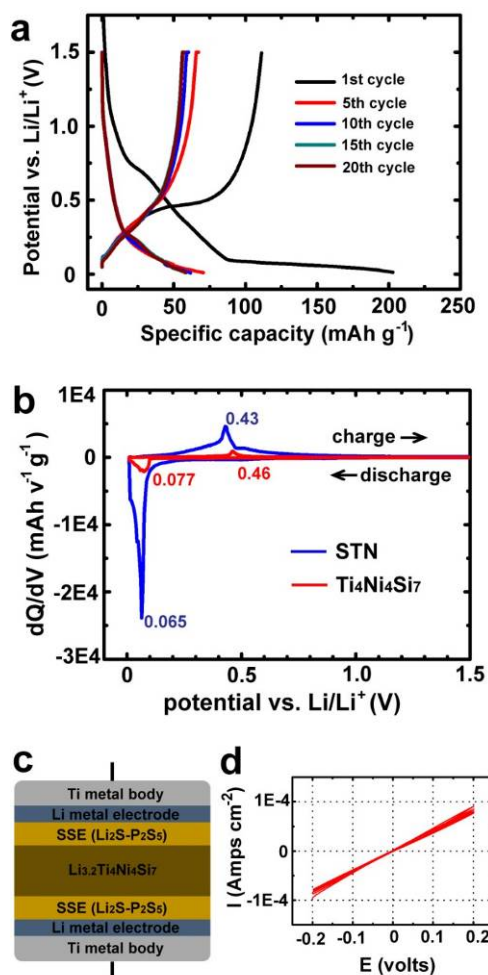


Figure 3.7. (a) Voltage profile versus specific capacity of $\text{Ti}_4\text{Ni}_4\text{Si}_7$ between 0.01 V and 1.5 V. (b) Differential capacity versus voltage curve of STN and $\text{Ti}_4\text{Ni}_4\text{Si}_7$. (c) Schematics of solid state conductivity cell configuration. (d) CV test between -0.2 V and 0.2 V of $\text{Li}_{3.2}\text{Ti}_4\text{Ni}_4\text{Si}_7$.

$\text{Li}_{3.2}\text{Ti}_4\text{Ni}_4\text{Si}_7$ was prepared by mixing $\text{Ti}_4\text{Ni}_4\text{Si}_7$ with an appropriate amount of stabilized Li metal powder (SLMP) [31]. An ionic conductivity cell was prepared (Figure 3.7c) to measure the ionic conductivity of $\text{Li}_{3.2}\text{Ti}_4\text{Ni}_4\text{Si}_7$ using two Li metal electrodes. Figure 3.7d shows the cyclic voltammetry (CV) test between -0.2 V and 0.2 V. The ionic conductivity of $\text{Li}_{3.2}\text{Ti}_4\text{Ni}_4\text{Si}_7$ can be calculated using equation (2) where R is the slope of the CV curve, l is the thickness of the $\text{Li}_{3.2}\text{Ti}_4\text{Ni}_4\text{Si}_7$ layer and A is the cross-sectional area of the cell.

$$\sigma = \frac{1}{R} \times \frac{l}{A} \quad (2)$$

We sandwiched 77.5 Li_2S : 22.5 P_2S_5 binary solid-state electrolyte (SSE) on both sides of our $\text{Li}_{3.2}\text{Ti}_4\text{Ni}_4\text{Si}_7$ layer to block electron transfer. The electron blocking electrode method is a very well-known method used to measure the ionic conductivity of mixed conductors [32, 33]. The SSE's contribution to Ohmic resistance is subtracted from that of the total cell to obtain the resistance of only the $\text{Li}_{3.2}\text{Ti}_4\text{Ni}_4\text{Si}_7$ pellet. We found that $\text{Li}_{3.2}\text{Ti}_4\text{Ni}_4\text{Si}_7$ has an ionic conductivity of $2.5 \times 10^{-5} \text{ S cm}^{-1}$. (It is known that Li ion conductivity of Si is order of $10^{-15} \text{ S cm}^{-1}$ at room temperature [34].) This value is only one

order of magnitude less than the ionic conductivity of a typical sulfide based SSE at room temperature [35]. This result indicates that $\text{Li}_x\text{Ti}_4\text{Ni}_4\text{Si}_7$ matrix takes a role as an ionic conductor during cycling. An electronic conductivity of 0.24 S cm^{-1} is also measured with using a Ti metal rod / $\text{Li}_{3.2}\text{Ti}_4\text{Ni}_4\text{Si}_7$ / Ti metal rod cell setup. This result also explains that excellent rate capability of STN alloy owing to the fact that $\text{Li}_x\text{Ti}_4\text{Ni}_4\text{Si}_7$ matrix is a mixed conductor. Good ionic conductivity confirms that the observed overpotential is likely not due to mass transfer effects but rather due to the mechanical confinement of nano-Si particles.

3.6 Material evolution of Si-Ti-Ni during cycling

Figure 3.8. presents the material evolution of our STN alloy upon cycling. Before cycling, the STN alloy consists of nano-Si embedded in a matrix of $\text{Ti}_4\text{Ni}_4\text{Si}_7$. The confirmation of the presence of nano-Si is also important because nano-Si has been shown to exhibit better cycling stability than bulk-Si. Nano particles are more resilient to the stresses associated with lithium-induced volume expansion, cracking and pulverization [7, 36]. After the first cycle, we have found that the $\text{Ti}_4\text{Ni}_4\text{Si}_7$ matrix is better represented by $\text{Li}_x\text{Ti}_4\text{Ni}_4\text{Si}_7$ according to our electrochemical study of a $\text{Ti}_4\text{Ni}_4\text{Si}_7$ ingot. When we consider the electrochemical participation of the $\text{Ti}_4\text{Ni}_4\text{Si}_7$ during cycling, we are then able to calculate that nano-Si is alloyed with 2.7 Li ions. EELS mapping (Figure 3.8c) confirms our theory of lithium distribution in the STN structure after its 50th charge. We find that Li ions in the matrix area are still present after charging. This infers that matrix maintains the composition of $\text{Li}_{3.2}\text{Ti}_4\text{Ni}_4\text{Si}_7$ and that the matrix's high ionic conductivity is preserved during cycling.

We previously used TEM EELS analysis to investigate the microstructural properties of a $\text{Ti}_4\text{Ni}_4\text{Si}_7$ ingot. To better understand the STN

alloy's charged state, we use the same analysis technique with a STN alloy sample collected after its 50th charge. Figure 3.8b and c presents the EELS analysis of this sample. When the zero loss image (Figure 3.8b) is compared to the EELS mapping (Figure 3.8c), we find that areas of strong contrast correspond to nano-Si and areas of weak contrast correspond to the $\text{Li}_{3.2}\text{Ti}_4\text{Ni}_4\text{Si}_7$ matrix. The zero loss images also do not show any evidence of cracks or material pulverization.

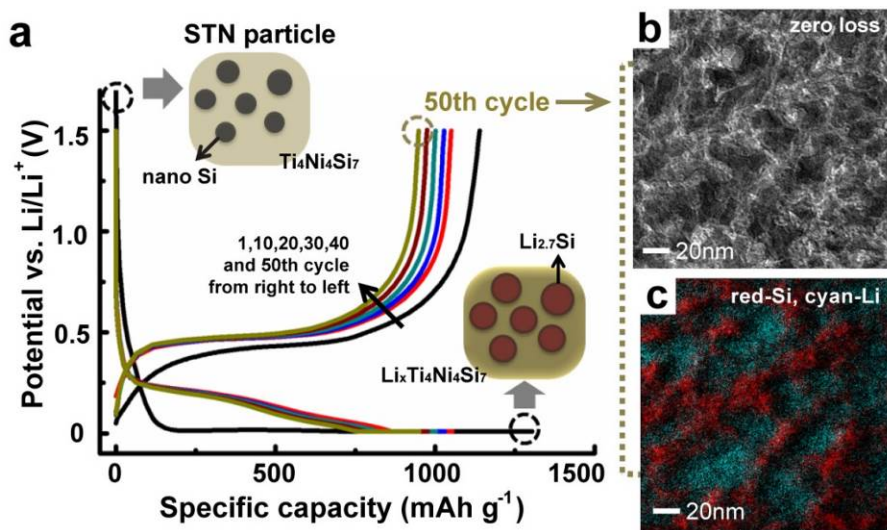


Figure 3.8. (a) Voltage profile versus specific capacity of 1, 10, 20, 30, 40 and 50 cycles with schematics of STN structure. (b) EELS zero loss image at 50th charged status. (c) EELS mapping at 50th charged status (where red: Si, cyan: Li).

3.7 Conclusions

We embed nano-Si in a $\text{Li}_x\text{Ti}_4\text{Ni}_4\text{Si}_7$ matrix for three reasons. First, because the $\text{Li}_x\text{Ti}_4\text{Ni}_4\text{Si}_7$ matrix limits the extent of Si lithiation. At STN's fully discharged state, one mole of Si is lithiated with 2.7 moles of Li ions ($\text{Li}_{2.7}\text{Si}$) instead of the 3.7 moles of Li ions ($\text{Li}_{3.7}\text{Si}$) in a typical Si electrode. Limiting the extent of lithiation minimizes the maximum stress generated by reducing the volume expansion experienced by a Si particle. Secondly, because the $\text{Li}_x\text{Ti}_4\text{Ni}_4\text{Si}_7$ matrix facilitates fast and efficient Li ion and electron transfer to nano-Si. We find that $\text{Li}_{3.2}\text{Ti}_4\text{Ni}_4\text{Si}_7$ functions as solid state ionic conductor with an ionic conductivity of $2.5 \times 10^{-5} \text{ S cm}^{-1}$ and an electronic conductivity of 0.24 S cm^{-1} at room temperature. And finally, because the $\text{Li}_x\text{Ti}_4\text{Ni}_4\text{Si}_7$ matrix helps to reduce the formation of an SEI layer on the Si surface. The formation of a SEI layer on the surface of active materials typically increases interfacial resistance to charge transfer and also lowers the CE of the system. Therefore, reducing the exposed active Si surface area will mitigate the parasitic reaction responsible for SEI layer formation. The $\text{Li}_x\text{Ti}_4\text{Ni}_4\text{Si}_7$ matrix coats much of the nano-Si surface and prevents the reduction of the organic electrolyte. This protection enables our

system to have better mass transfer kinetics and a high CE[37-39]. As a result, our STN system demonstrates a specific capacity in excess of 900 mAh g⁻¹ after the 50th discharge-charge cycle and a CE of 99.7% at a rate of 1C. We have presented a low-cost nanoscale Si anode. Previous nanoscale Si anodes suffer from capacity fade because full utilization of Si results in mechanical fatigue and because their large surface area reacts readily with organic liquid electrolyte. Creative, but expensive ways to mitigate stress evolution have been devised but few Si anodes with acceptable CE have been developed. The electrochemically activated Li_xTi₄Ni₄Si₇ matrix is an extraordinary material that both electrochemically and mechanically enables the reversible and stable cycling of nano-Si for high energy density LIB.

3.8 Experimental section

Melt spun ribbon was obtained by a single roller melt-spinning technique. Copper quenching roller with a diameter of 400 mm is used for rapid solidification at the ratio of 1500 rates per minute (RPM). This process is done under Ar atmosphere. The molten state of Si-Ti-Ni master alloy is used with an atomic ratio of 68%-16%-16% as a starting material, respectively.

A composition of $\text{Ti}_4\text{Ni}_4\text{Si}_7$ particles is prepared as follows. A melt of Ti (99.99%), Ni (99.99%) and Si (99.5%) was prepared by heating a molar ratio of $\text{Ti}_4\text{Ni}_4\text{Si}_7$ using an electric arc melting furnace. After electric arc heating, the melt is cooled in a Cu mold by running cold water through the inside of the mold. XRD results shown in Figure 3.9 confirm the $\text{Ti}_4\text{Ni}_4\text{Si}_7$ phase.

Standard types of 2016 half coin cells with Li metal foil as a counter electrode were prepared for these experiments. The anode mixture was composed of STN, ketjen black and polyamide/imide (PAI) binder with a wt % ratio of 88%-4%-8%, and mixed with a 1-methyl-2-pyrrolidinone (NMP) solution. The mixture was coated on Cu foil and then dried under air. Considering weight ratio among materials, 1.0 mg cm^{-2} of STN is applied on the single electrode. 1.5 M LiPF_6 in ethylene carbonate, diethyl carbonate

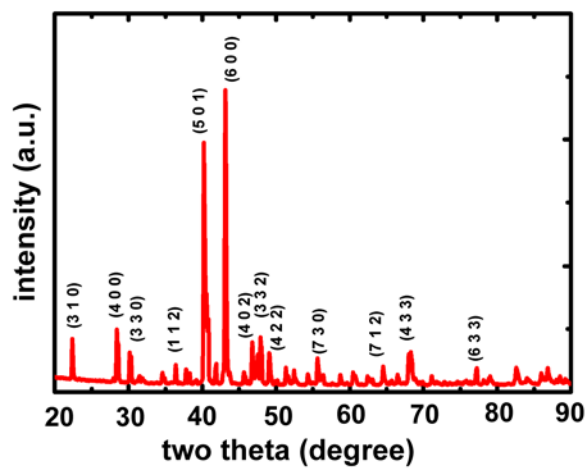


Figure 3.9. XRD result of synthesized $\text{Ti}_4\text{Ni}_4\text{Si}_7$.

and fluoroethylene carbonate (5:70:25) was used as the electrolyte [40]. Constant current (CC) is applied during discharge and charge between the voltage range of 0.01 V and 1.5 V. Constant voltage (CV) is applied until amount of 0.01c is achieved at 0.01 V and 20 minutes of holds are made at both 0.01 V and 1.5 V.

SLMP (FMC Lithium Corp.) is used to synthesize a $\text{Li}_x\text{Ti}_4\text{Ni}_4\text{Si}_7$. SLMP and $\text{Ti}_4\text{Ni}_4\text{Si}_7$ is mixed for half an hour and heat treated at 100°C for 2 hours in the Ar-filled glove box. Li_2S (Aldrich, 99.999%) - P_2S_5 (Aldrich, 99%) at a molar ratio of 77.5:22.5 respectively, is used as a SSE. These starting materials were combined into a stainless steel vial and planetary ball milling was carried out for 20 continuous hours. All pressing and testing operations were carried out with Ti metal bodies as current collectors and covered by a poly (aryl ether ether ketone) mold ($\Phi = 1.3$ cm). Li metal foil (Alfa Aesar) is used for electrodes. All assembly processes of solid state ionic conductivity cell were carried out in Ar-filled glove box.

A FIB (FEI, NOVA200 dual beam system) equipped with an air-lock chamber is used for TEM sample preparation. Ga ion source is used for FIB sectioning. The use of an air-lock system enables to observe lithiated STN

structure without any exposure to the air. Air exposure to lithiated sample causes structure changes with oxidation, however this mobile air-lock system maintains a vacuum state while samples are loaded from glove box to FIB chamber. Our previous paper explains the sample prepare sequence in detail [8].

The microstructure of STN structure was investigated by HR-TEM (JEOL 3000F equipped with EDS) operating at 300 keV and analytical TEM (TECNAI F20 equipped with EELS) operating at 200 keV. XRD data for phase determination was collected with X-ray diffractometer (XRD, Bruker, D8 Advance) with Cu-K α radiation.

3.9 References

- [1] J. M. Tarascon, M. Armand, *Nature* **2001**, 414, 359.
- [2] C. K. Chan, H. L. Peng, G. Liu, K. McIlwrath, X. F. Zhang, R. A. Huggins, Y. Cui, *Nat. Nanotechnol.* **2008**, 3, 31.
- [3] T. D. Hatchard, J. R. Dahn, *J. Electrochem. Soc.* **2004**, 151, A838.
- [4] M. N. Obrovac, L. Christensen, *Electrochem. Solid State Lett.* **2004**, 7, A93.
- [5] A. H. Mayne, S. C. Bayliss, P. Barr, M. Tobin, L. D. Buckberry, *Phys. Status Solidi A-Appl. Res.* **2000**, 182, 505.
- [6] U. Kasavajjula, C. S. Wang, A. J. Appleby, *J. Power Sources* **2007**, 163, 1003..
- [7] S. Golmon, K. Maute, S. H. Lee, M. L. Dunn, *Appl. Phys. Lett.* **2010**, 97
- [8] S. B. Son, J. E. Trevey, H. Roh, S. H. Kim, K. B. Kim, J. S. Cho, J. T. Moon, C. M. DeLuca, K. K. Maute, M. L. Dunn, H. N. Han, K. H. Oh, S. H. Lee, *Adv. Energy Mater.* **2011**, 1, 1199.
- [9] V. A. Sethuraman, M. J. Chon, M. Shimshak, V. Srinivasan, P. R. Guduru, *J. Power Sources* **2010**, 195, 5062.

- [10] S. D. Beattie, D. Larcher, M. Morcrette, B. Simon, J. M. Tarascon, *J. Electrochem. Soc.* **2008**, 155, A158.
- [11] J. E. Trevey, K. W. Rason, C. R. Stoldt, S. H. Lee, *Electrochem. Solid State Lett.* **2010**, 13, A154.
- [12] H. Kim, J. Cho, *Nano Lett.* **2008**, 8, 3688.
- [13] X. H. Liu, L. Q. Zhang, L. Zhong, Y. Liu, H. Zheng, J. W. Wang, J. H. Cho, S. A. Dayeh, S. T. Picraux, J. P. Sullivan, S. X. Mao, Z. Z. Ye, J. Y. Huang, *Nano Lett.* **2011**, 11, 2251.
- [14] A. Magasinski, P. Dixon, B. Hertzberg, A. Kvit, J. Ayala, G. Yushin, *Nat. Mater.* **2010**, 9, 353.
- [15] H. Jung, Y. U. Kim, M. S. Sung, Y. Hwa, G. Jeong, G. B. Kim, H. J. Sohn, *J. Mater. Chem.* **2011**, 21, 11213.
- [16] H. T. Nguyen, F. Yao, M. R. Zamfir, C. Biswas, K. P. So, Y. H. Lee, S. M. Kim, S. N. Cha, J. M. Kim, D. Pribat, *Adv. Energy Mater.* **2011**, 1, 1154.
- [17] B. S. Lee, S. B. Son, K. M. Park, W. R. Yu, K. H. Oh, S. H. Lee, *J. Power Sources* **2012**, 199, 53.

- [18] L. Q. Mai, B. Hu, W. Chen, Y. Y. Qi, C. S. Lao, R. S. Yang, Y. Dai, Z. L. Wang, *Adv. Mater.* **2007**, 19, 3712.
- [19] L. Q. Mai, L. Xu, B. Hu, Y. H. Gu, *J. Mater. Res.* **2010**, 25, 1413.
- [20] H. H. Liebermann, C. D. Graham, *IEEE Trans. Magn.* **1976**, 12, 921.
- [21] B. Gupta, N. Revagade, J. Hilborn, *Prog. Polym. Sci.* **2007**, 32, 455.
- [22] A. Manaf, R. A. Buckley, H. A. Davies, M. Leonowicz, *J. Magn. Magn. Mater.* **1991**, 101, 360.
- [23] Z. L. Xie, J. VanHumbeeck, Y. Liu, L. Delaey, *Scripta Mater.* **1997**, 37, 363.
- [24] E. Horache, T. P. Feist, J. A. Stuart, J. E. Fischer, *J. Mater. Res.* **1990**, 5, 1887.
- [25] J. H. Westbrook, R. K. DiCerbo, A. J. Peat, *GE Technical Report* **1958**, 58-RL-2117, 1.
- [26] C. J. Yu, X. Li, T. Ma, J. P. Rong, R. J. Zhang, J. Shaffer, Y. H. An, Q. Liu, B. Q. Wei, H. Q. Jiang, *Adv. Energy Mater.* **2012**, 2, 68.
- [27] X. L. Li, J. H. Cho, N. Li, Y. Y. Zhang, D. Williams, S. A. Dayeh, S. T. Picraux, *Adv. Energy Mater.* **2012**, 2, 87.

- [28] T. H. Hwang, Y. M. Lee, B. S. Kong, J. S. Seo, J. W. Choi, *Nano Lett.* **2012**, 12, 802.
- [29] H. Wu, G. Zheng, N. Liu, T. J. Carney, Y. Yang, Y. Cui, *Nano Lett.* **2012**, 12, 904.
- [30] V. A. Sethuraman, V. Srinivasan, A. F. Bower, P. R. Guduru, *J. Electrochem. Soc.* **2010**, 157, A1253.
- [31] C. R. Jarvis, M. J. Lain, Y. Gao, M. Yakovleva, *J. Power Sources* **2005**, 146, 331.
- [32] D. J. Vischjager, A. A. van Zomeren, J. Schoonman, I. Kontoulis, B. C. H. Steele, *Solid State Ion.* **1990**, 40-41, 810.
- [33] T. Inoue, J. I. Kamimae, M. Ueda, K. Eguchi, H. Arai, *J. Mater. Chem.* **1993**, 3, 751.
- [34] I. Riess, *Solid State Ion.* **1991**, 44, 199.
- [35] J. Trevey, J. S. Jang, Y. S. Jung, C. R. Stoldt, S. H. Lee, *Electrochem. Comm.* **2009**, 11, 1830.
- [36] H. Gleiter, *Prog. Mater. Sci.* **1989**, 33, 223.
- [37] Y. M. Lee, J. Y. Lee, H. T. Shim, J. K. Lee, J. K. Park, *J. Electrochem. Soc.* **2007**, 154, A515.

- [38] F. Kong, R. Kostecki, G. Nadeau, X. Song, K. Zaghbi, K. Kinoshita, F. McLarnon, *J. Power Sources* **2001**, 97-98, 58.
- [39] H. Nakai, T. Kubota, A. Kita, A. Kawashima, *J. Electrochem. Soc.* **2011**, 158, A798.
- [40] N. S. Choi, K. H. Yew, K. Y. Lee, M. Sung, H. Kim, S. S. Kim, *J. Power Sources* **2006**, 161, 1254.

Chapter 4: A Stabilized PAN-FeS₂ Cathode with an EC/DEC Liquid Electrolyte

4.1 Introduction

The energy density of conventional Li-ion batteries with LiMO₂ (M = transition metal) cathodes and graphitic anodes is approaching a practical upper limit after two decades of optimization. In order to improve the energy density of Li-ion batteries further, new cathodes must be developed with capacities that compare to those of advanced anodes such as Si [1]. The FeS₂ conversion chemistry is a promising candidate to replace the LiMO₂ intercalation chemistry because FeS₂ is inexpensive, energy dense, and environmentally benign. The four electron reduction of cubic-FeS₂ (pyrite) with lithium ($\text{FeS}_2 + 4\text{Li}^+ + 4\text{e}^- \rightarrow \text{Fe} + 2\text{Li}_2\text{S}$) provides a specific capacity of 894 mAh g⁻¹, whereas, the very best LiMO₂ intercalation cathodes can only provide 200 mAh g⁻¹ [2-8]. For these reasons Energizer popularized the FeS₂/Li chemistry as a primary battery [9], but a secondary FeS₂/Li battery is not yet commercially available. The safety issues associated with lithium metal anodes can be cited as one obstacle obstructing the realization of a

rechargeable FeS₂/Li battery [10-12], however, the FeS₂ cathode also presents very difficult problems. This paper addresses the problems of the cathode by embedding natural pyrite in a commercially available, stabilized PAN matrix.

The problems associated with a rechargeable FeS₂ cathode can be understood by considering the electroactive species of FeS₂ during cycling. Though still the subject of much debate, a proposed reaction mechanism for cubic-FeS₂ at low temperatures is provided below for an initial discharge and subsequent charge [7, 11-14]. From Eq. (4.2) we see that small aggregates of superparamagnetic Fe⁰ atoms are one product of the reduction of FeS₂ with four Li⁺. Fe₀ particles have an average diameter of 3.6 nm and are highly reactive in order to catalyze the oxidation of the other full discharge product, Li₂S, which is highly resistive. Unfortunately, nano-Fe⁰ particles tend to agglomerate into non-reactive α-Fe particles which results in the electrochemical isolation of Li₂S and a rapid loss of battery capacity [11, 15].

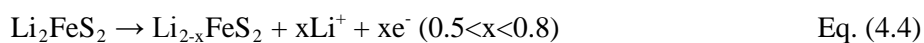
From Eq. (4.5) it is also evident that cubic-FeS₂ is not reformed at full charge. Our previous work found that the charge products of an all-solid-state cubic-FeS₂ cathode are a multiphase mixture of ortho-FeS₂ (marcasite), FeS_{8/7}, and S [11]. Prior to this study it was generally accepted that the charge

products were only Fe_{1-x}S and S from the disproportionation of an $\text{Li}_{2-x}\text{FeS}_2$ intermediary phase [11]. This work will provide further evidence that ortho- FeS_2 is a charge product at ambient temperature. More importantly, the reversibility and efficiency of FeS_2 batteries will suffer from the same problems as that of a Li-S battery because sulfur is one of the three proposed charge products. The initial reduction of sulfur produces soluble and highly mobile polysulfides (S_n^{2-}). The dissolution of these polysulfides into an organic liquid electrolyte contributes to capacity fade and results in a parasitic redox shuttle that reduces charging efficiency [16-20].

Initial Discharge



Subsequent Charge



The mobility of Fe^0 and polysulfides in organic liquid electrolytes explains why conventional FeS_2 cathodes are not reversible. An all-solid-state battery architecture is uniquely capable of confining the electroactive species of FeS_2 [15, 21] and we recently demonstrated the full reversibility of FeS_2 as a cathode versus lithium metal at 60°C [11]. Though this study represents a milestone for the secondary FeS_2 conversion chemistry, it is still more desirable to incorporate FeS_2 into a conventional liquid or polymer battery because the manufacturing processes associated with conventional batteries are mature. Prior to our work many studies attempted to use composite polymer electrolytes to confine FeS_2 's electroactive species [8, 22-25]. Unfortunately, none of these studies could demonstrate acceptable reversibility because polymer electrolytes do not provide sufficient confinement. More recently, other studies have examined the cycle ability of synthetic FeS_2 /carbon and FeS_2 /PANI composites in liquid electrolytes with limited success [8, 19, 26-28].

Here, we embed FeS_2 in a stabilized PAN matrix that confines electroactive species to prevent active material loss and improve Coulombic efficiency (CE). Stabilized PAN enables the reversibility of FeS_2 by

considering the need to not only confine FeS_2 's electroactive species but also to accommodate FeS_2 's expansion. The effectiveness of stabilized polymers as confining matrices has been previously demonstrated with PAN-S and PANi-S composites [29-31]. It has also been shown that thin coatings of stabilized PAN can accommodate the 300% volume expansion of nano-Si particles. [32] By avoiding the full carbonization of PAN the elastic properties of the PAN precursor can be retained, while the conjugation of PAN during the stabilization process provides good electronic conductivity [33]. More importantly, the preparation of the PAN- FeS_2 composite is simple and the precursors are inexpensive, commercially available natural pyrite and PAN. The results of this study will demonstrate that the challenges associated with a conventional FeS_2 cathode can be overcome.

4.2 Previous study of Li/FeS₂ with solid state electrolyte

4.2.1 Solid state battery architecture

The basic nature of an all-solid-state cell enables the reversible Li/FeS₂ system with the confinement of electro-active species. Li₂S-P₂S₅ binary glass-ceramic solid electrolytes are applied to demonstrate the reversible Li/FeS₂ system at ambient temperature and elevated temperature.

Synthetically prepared FeS₂ is characterized with FESEM microscopy and x-ray analysis. FESEM shows cubic FeS₂ particles with 3μm wide faces (Figure 4.1a). X-ray diffraction analyses of synthetically prepared FeS₂ match well with cubic pyrite (Figure 4.1b).

Cell fabrication and cell testing for this study was carried out under an inert argon gas environment. And Figure 4.2 shows the architecture of all-solid-state lithium batteries (ASSLBs). The composite positive electrode is a 10:20:2 weight ratio mixture of synthetic FeS₂, 77.5 Li₂S: 22.5 P₂S₅, and carbon black (Timcal Super C65) respectively. The composite positive electrode is mixed using an agate mortar and pestle. Stabilized lithium metal powder (SLMP) is used as the negative electrode (FMC Lithium Corp.). The construction of solid state cells utilizes a titanium-polyaryletheretherketone

(PEEK) test cell die. 200 mg of solid electrolyte powder is pressed at 1 metric ton in the PEEK cell die. 5 mg of composite positive electrode and the stabilized lithium metal powder are then attached to opposite sides of the solid electrolyte pellet by pressing at 5 metric tons. Cycling test was also conducted in glove box filled with Ar gas at ambient temperature and elevated temperature (60°C).

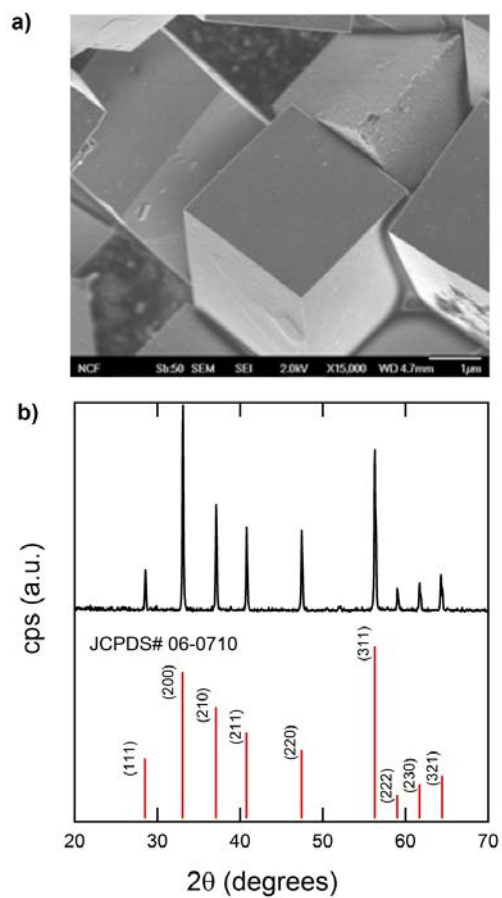


Figure 4.1. (a) FESEM micrograph of synthetic FeS₂ that confirms cubic structure with 2-3 μm cubes. (b) X-ray diffraction of synthetic pyrite.

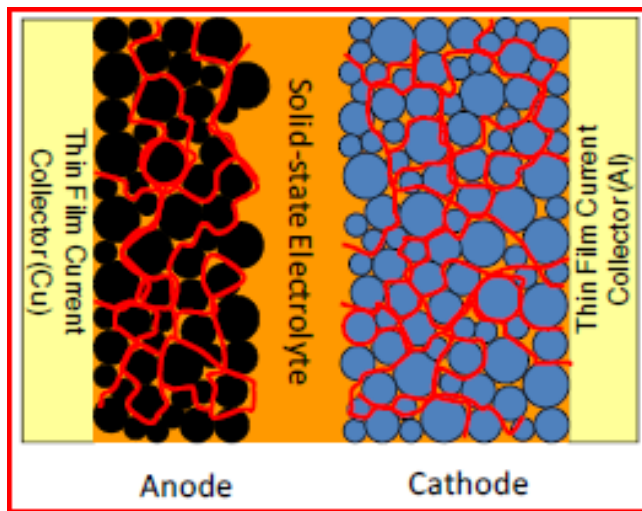


Figure 4.2. ASSLBs configuration. Black represents SLMP material, orange represents sulfide based glass-ceramic electrolyte 77.5 Li₂S – 22.5 P₂S₅ system and blue represents synthetic FeS₂ active material.

4.2.2 Reversible cycle stability of Li/FeS₂ with solid state battery

Constant current constant voltage test of synthetic FeS₂ was conducted in both an all-solid-state and liquid cell configuration. Voltage range of 1.0V and 3.0V vs. Li⁺/Li was applied to achieve full utilization of FeS₂. The results of cycling at ambient temperature (30°C) and moderate temperature (60°C) are given in Figure 4.3. Cells cycled with solid state electrolyte show a stable capacity during cycling and gradual increase in capacity with cycling is owing to better FeS₂ utilization. Cell cycled at 30°C exhibits a discharge capacity of 750 mAh g⁻¹ by the 20th cycle while the cell cycled at 60°C exhibits a theoretical discharge capacity of 894 mAh g⁻¹. It is assumed that the ionic conductivity of solid electrolyte contributes to the full FeS₂ utilization. It is known that conductivity of the 77.5 Li₂S - 22.5 P₂S₅ solid electrolytes improves from 9.17x10⁻⁴ Ω⁻¹ cm⁻¹ (30°C) to 4.4x10⁻³ Ω⁻¹ cm⁻¹ (60°C).

HRTEM analysis was conducted to determine the structures and phases and electrode material from the solid-state cell cycled at 60°C upon completion of its 20th charge are prepared for the observation as shown in Figure 4.4. Figure 4.5a shows a BF image TEM image of the 20th cycled charged FeS₂ solid-state electrode. Darker areas correspond to nano-

crystalline orthorhombic-FeS₂ while the lighter areas correspond to an amorphous region composed of FeS_y and elemental sulfur. FFT analyses of HRTEM images matches well with orthorhombic-FeS₂ along the [-110] zone axis (Figure 4.5b).

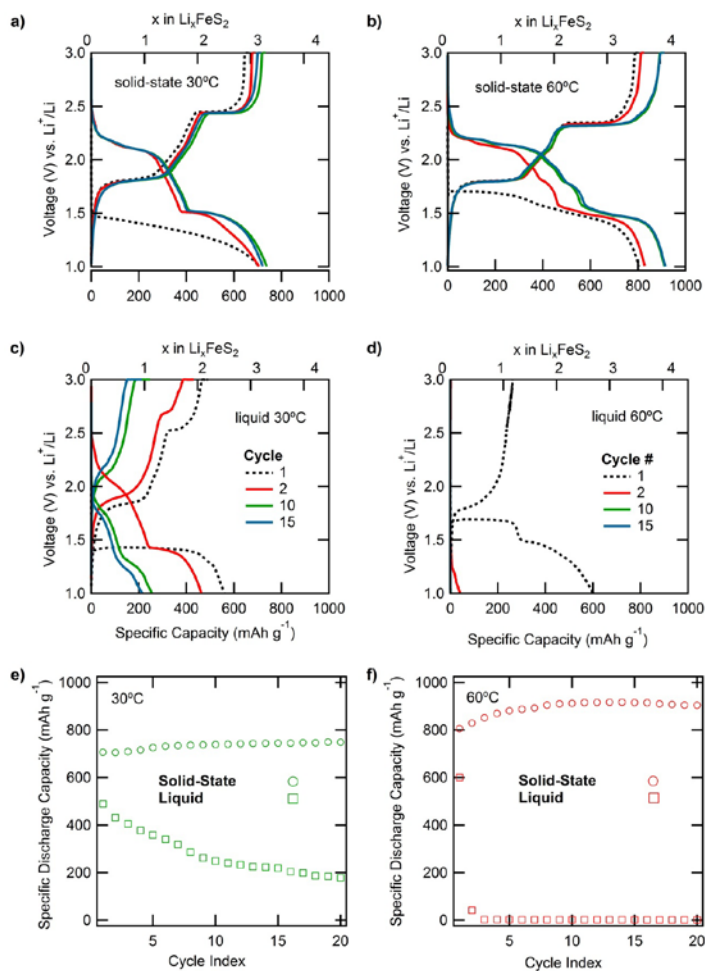


Figure 4.3. FeS_2 cycled at 30°C and 60°C in conventional liquid coin cell and in an all-solid-state configuration. (a) solid-state at 30°C, (b) solid-state at 60°C, (c) liquid coin cell at 30°C, (d) liquid coin cell at 60°C, (e) cycling data for cells cycled at 30°C, and (f) cycling data for cells cycled at 60°C. All cells cycled at a rate of C/10 for charge and discharge.

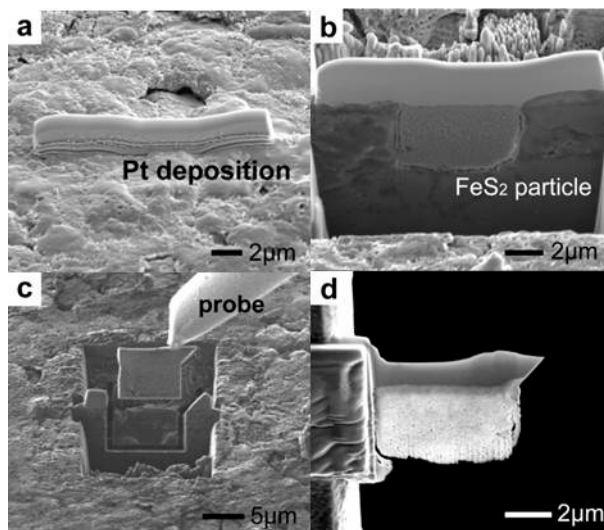


Figure 4.4. FIB preparation sequence. (a) Pt deposition upon FeS₂ particle, (b) Ga⁺ ion milling of FeS₂ particle, (c) recovery of FeS₂ particle using lift-out technique and (d) final thinning of FeS₂ sample to 50-80nm.

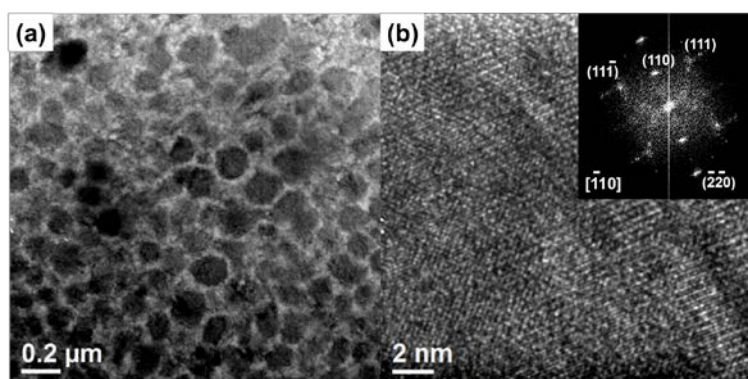


Figure 4.5. Electrode material from the solid-state cell cycled at 60°C was recovered after the 20th charge for TEM analysis. (a) Bright field TEM image of the 20th cycle sample. (b) HR-TEM of the 20th cycle sample. FFT analysis matches with orthorhombic-FeS₂ along the $[-110]$ zone axis.

4.3 Li/FeS₂ with EC/DEC electrolyte

4.3.1 Synthesis and microstructure observation of PAN-FeS₂

The natural pyrite used in this study was first ball milled in order to reduce the average particle size. Field emission scanning electron microscopy (FESEM) of ball milled FeS₂ provided in Figure 4.6a shows that particles vary in diameter from 100 nm to 10 μm and X-ray diffraction (XRD) of the ball milled material provided in Figure 4.6b confirms that our material is phase pure pyrite (cubic-FeS₂).

Figure 4.7 presents the microstructure and elemental mapping of an uncycled PAN-FeS₂ composite electrode. A Focused Ion Beam (FIB) microscope was used to prepare a sample for HRTEM [34]. Platinum was deposited on the electrode surface in order to protect the observation area during FIB cross sectioning. A cross-sectional image (Figure 4.7a) shows that most ball milled FeS₂ particles are fully embedded in the stabilized PAN matrix. Figure 4.7b presents the electron energy loss spectrum (EELS) zero-loss image and Figure 4.7c presents the EELS elemental mapping of the same cross-sectioned sample. EELS mapping shows that the PAN matrix area is matched with C (red) and the embedded particles are matched with Fe (blue)

and S (green).

It is possible that FeS₂ may have decomposed during the secondary stabilization heat treatment at 500°C because FeS₂ has been shown to thermal decompose to Fe_{1-x}S and S at the slightly higher temperature of 550°C [35]. Should S have been evolved from the decomposition of FeS₂ it would react with PAN and be widely distributed like S in the PAN-S materials [29]. However, the EELS elemental mapping indicates that S is segregated to FeS₂ particles. Because S is not distributed throughout the sample we conclude that FeS₂ did not decompose during the secondary heat treatment and that FeS₂ does not react with PAN. Figure 4.8 provides the individual EELS elemental mappings of Fe, S and C.

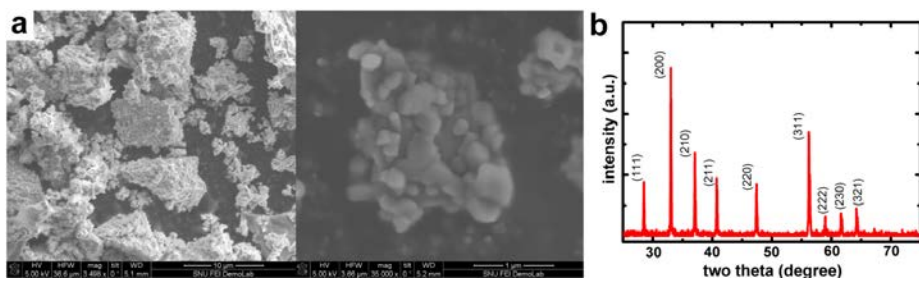


Figure 4.6. (a) SEM observation of 1hour ball milled natural pyrite. (b) After natural pyrite is ball milled, powder XRD analysis was performed to determine the phases and matched with cubic-FeS₂ (71-2219).

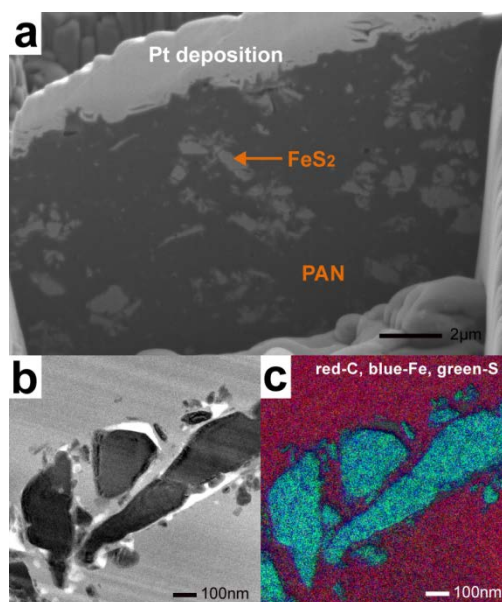


Figure 4.7. (a) Cross-sectional SEM image of an uncycled PAN-FeS₂ electrode. (b) TEM image with EELS zero-loss mode of the stabilized PAN matrix (light) and embedded FeS₂ particles (dark). (c) EELS elemental mapping of C (red), Fe (blue), and S (green).

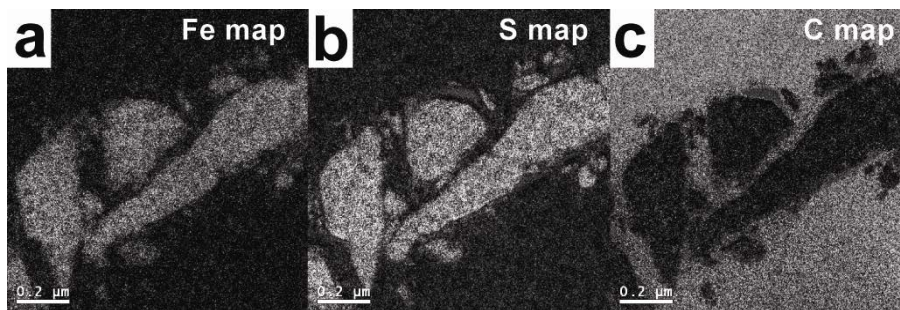


Figure 4.8. (a) EELS iron mapping of Figure 1b. (b) EELS sulfur mapping of Figure 1b. (c) EELS carbon mapping of Figure 1b.

4.3.2 Electrochemical properties of PAN-FeS₂ and bare FeS₂.

Two electrodes were characterized electrochemically using a constant current, constant voltage (CCCV) cycling protocol. The first electrode was made with the PAN-FeS₂ electrode material presented in Figure 4.9 while the second electrode is a control sample which we will call bare FeS₂. Both cells were cycled between 1V and 3V at a rate of 0.1 C for all cycles. The cyclic stabilities and CE of the PAN-FeS₂ (red) and bare FeS₂ (orange) electrodes are provided in Figure 4.9a. Bare FeS₂ delivers an initial discharge capacity of 828 mAh g⁻¹ which is close to FeS₂'s theoretical capacity of 894 mAh g⁻¹. Bare FeS₂ has a notably low initial CE of 63% along with a consistently low cycling CE, drastically hindering its capacity retention so that by the 20th cycle it delivers a discharge capacity of only 120 mAh g⁻¹, or only 14% of its initial discharge capacity. Though PAN-FeS₂ delivers a lower initial discharge capacity of 729 mAh g⁻¹, its cyclic stability and CE are greatly improved compared to bare FeS₂. With a significantly improved initial CE of 94%, our PAN-FeS₂ electrode delivers 470 mAh g⁻¹, a discharge capacity retention value of 64%, with a CE approaching 99.25% by the 50th cycle. Other FeS₂-C composite electrodes showed at most ~350 mAh g⁻¹ by the 40th

cycle [8,26-27]. PAN-FeS₂ not only exceeds capacities shown by previous work, but it is also unique in that the precursors are commercially available natural pyrite and PAN [8, 22-25]. Figure 4.9b and 4.9c provide the voltage profiles for PAN-FeS₂ and bare FeS₂, respectively. The stable capacity of PAN-FeS₂ is correlated with voltage profiles that are more stable compared to that of bare FeS₂. With cycling, bare FeS₂'s voltage profiles develop overpotentials and lose the upper charging voltage plateau at approximately 2.4V.

Historically, only FeS and S were identified as charge products. The difference between the first and subsequent discharge voltage profiles was explained by the fact that the reduction of S occurs at a higher potential than that of either FeS or cubic-FeS₂. The potential of the higher voltage plateau of subsequent discharges is very close to that of sulfur.

In our previous work [11], we studied an all-solid-state FeS₂/Li metal battery and discovered ortho-FeS₂ (marcasite) as a new charge product. That work concluded that the charge products are well represented by Eq. (4.5) and we expect the ratio of charge products in our PAN-FeS₂ electrode to be similar. Charge products given in Eq. (4.5) are ortho-FeS₂, FeS, and S. It

should be noted that Eq. (4.5) can only progress in the direction written and that the discharge path for each charge product follows a different path.

We also concluded that the reduction of electrochemically precipitated ortho-FeS₂ occurs at a higher potential than that of cubic-FeS₂. The difference between initial and subsequent voltage profiles can be explained by the reduction of ortho-FeS₂ instead of cubic-FeS₂. We believe that Equation 1 will progress at difference potentials based upon the phase of FeS₂ present. The 1st two-electron reduction of electrochemically precipitated ortho-FeS₂ occurs at 2.1 V which is very close to the reduction potentials of sulfur.

To differentiate the reduction of ortho-FeS₂ from the reduction of sulfur, we examined the differential capacity (dQ/dV) profiles of our PAN-FeS₂ electrodes. A dQ/dV peak corresponds to a voltage plateau and a specific chemical reaction according to Gibb's phase rule assuming that kinetics are fast. The area under a dQ/dV peak is the capacity (mAh) that a certain chemical reaction delivers. We see that PAN-FeS₂ exhibits 3 plateaus in the range of 1.8 – 2.8 V. According to literature, sulfur should exhibit two peaks at approximately 2.2 and 2.4 V. We observe these two peaks in Figure 4.14a and b. The third peak at 2.1 V is attributed to the reduction of ortho-FeS₂

which occurs at a higher potential than the reduction of cubic-FeS₂. Though we did not attempt to deconvolute the dQ/dV peaks, the peak corresponding to the initial reduction of ortho-FeS₂ (Eq. (4.1)) is much larger than the peaks for sulfur. For this reason sulfur is not a dominant active material, but it is certainly substantial. Instead, we believe that ortho-FeS₂ is the dominant active material on subsequent cycles and that Eq. (4.5) reflects the ratio of charge products approximately.

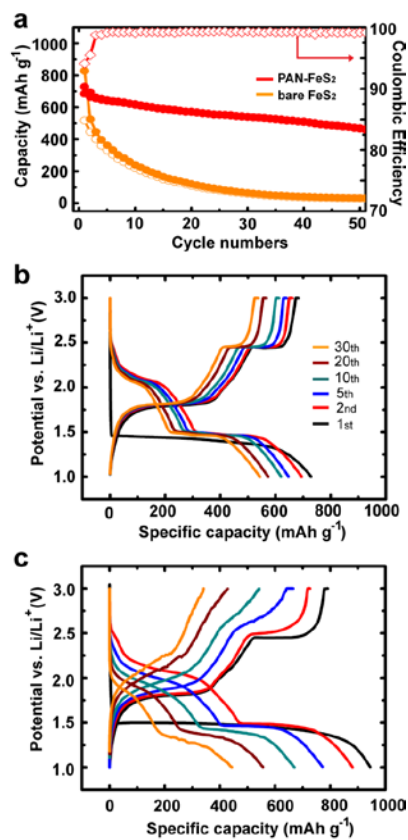


Figure 4.9. (a) Cyclic stability of the stabilized PAN-FeS₂ electrode versus that of a bare FeS₂ electrode. Specific capacity is reported w.r.t. mass of the FeS₂ active material. (b) Voltage profiles of PAN-FeS₂. (c) Voltage profiles of bare FeS₂.

4.3.3 Microstructure observation of 10th charged PAN-FeS₂.

To better understand the mechanism behind the improved stability of the PAN-FeS₂ electrode and identify the phases present at full charge, we use TEM and EELS to study the microstructure of a PAN-FeS₂ electrode recovered after completion of its 10th charge. As with the uncycled PAN-FeS₂ sample, the 10th charge TEM sample is prepared using a FIB microscope as shown in Figure 4.10. The bright field TEM image of an embedded FeS₂ particle is provide in Figure 4.11a while the HRTEM image and fast Fourier transform (FFT) of the same particle is provided in Figure 4.11b. Although we observed cubic-FeS₂ before cycling, the FFT of the HRTEM image matches with ortho-FeS₂ (marcasite) along the [01-1] zone axis. Because our electrode is made with phase pure natural cubic-FeS₂ (Figure 4.6b), we conclude that the observed ortho-FeS₂ is produced electrochemically. This result is consistent with our previous all-solid-state FeS₂/Li battery study where we observed ortho-FeS₂ as a charge product [11]. It is the first time that ortho-FeS₂ has been observed in an ambient temperature battery because the aforementioned all-solid-state FeS₂ sample was recovered after charging at 60°C. Later in the discussion we will analyze

the differential capacities (dQ/dV) of the two electrodes presented in Figure 4.9 in order to provide further evidence that Eq. (4.5) is the valid reaction for FeS_2 's final charging step.

Figures 4.11c and d provide the EELS elemental mapping of Fe and S while Figure 4.12 provides the zero-loss and the EELS mapping of C for the same particle. After cycling, it is clear that there is no migration of S or Fe into the stabilized PAN matrix. This result suggests that the stabilized PAN matrix completely obstructs the dissolution of intermediate polysulfides into the liquid electrolyte and prevents the reaction of Fe^0 with the liquid electrolyte. Confinement of polysulfides explains why PAN- FeS_2 exhibited a higher CE than bare FeS_2 . By confining polysulfides in PAN the parasitic shuttle mechanism, which reduces charging efficiency, cannot be initiated. It also suggests that our stabilized PAN is not very porous to accommodate the passage of solvated polysulfides. Supporting this idea, we measured the Brunauer-Emmett-Teller (BET) porosity of PAN- FeS_2 to be only $1.50 \text{ m}^2 \text{ g}^{-1}$. Because PAN- FeS_2 has such a low porosity, it also suggests that it is difficult for the liquid electrolyte to impregnate the stabilized PAN matrix. Previously, we have found that stabilized PAN is electrochemically active and stable

against the liquid electrolyte between 50 mV and 1V [32]. Here, we also show PAN's electro-chemical stability within a voltage window of 1V to 3V after running parallel experiments to those reported in this work with cells only containing stabilized PAN and no FeS₂ (Figure 4.13). The stabilized PAN materials shows the initial discharge capacity of 35 mAh g⁻¹ with a CE of 74%. By the 50th cycle stabilized PAN achieves 16 mAh g⁻¹ and CE approaches up to 98%. This result reveal that achieved capacity of PAN-FeS₂ during cycles are mainly contributed by FeS₂ conversion electrochemistry. We suspect that stabilized PAN is a mixed conductor, however, more work is currently underway to characterize its conductive properties.

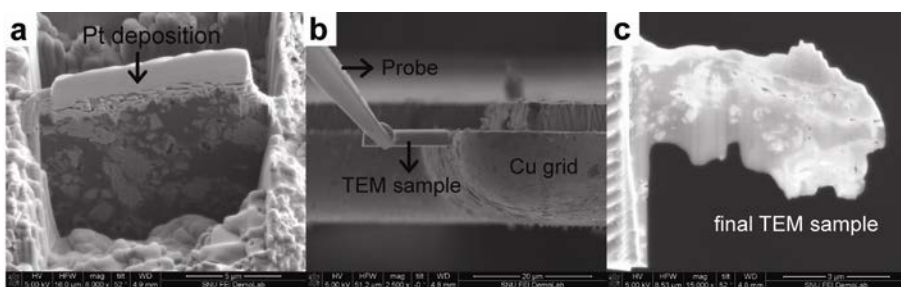


Figure 4.10. Typical TEM sample preparation sequence using the FIB. (a) Pt deposition on protect particle surface and cross sectioning of desired PAN-FeS₂ particle. (b) Sample lift out using manipulating probe on Cu grid. (c) Achieved final TEM sample.

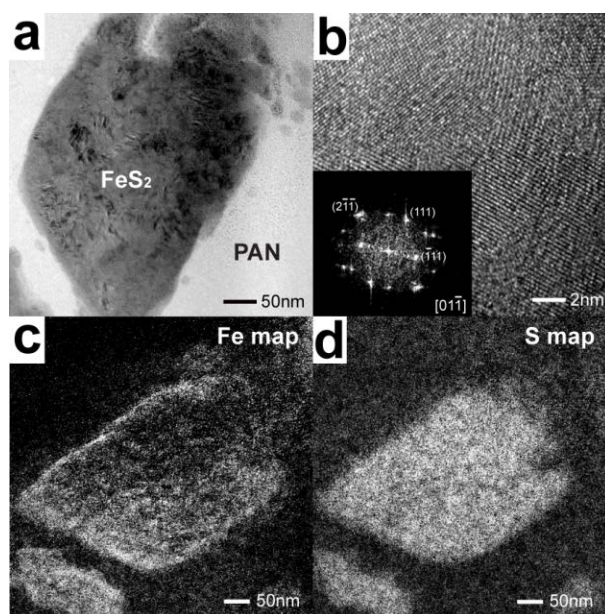


Figure 4.11. (a) TEM image of an embedded FeS_2 particle in a PAN- FeS_2 electrode collected after completion of its 10th charge. (b) High resolution (HR) image of the FeS_2 particle in Figure 4.9a and the corresponding FFT pattern matched with orthorhombic- FeS_2 along the $[01\bar{1}]$ zone axis. (c) EELS elemental mapping for Fe. (d) EELS elemental mapping of S.

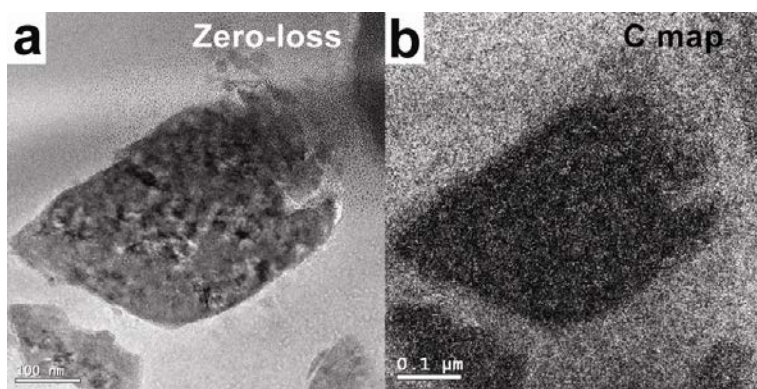


Figure 4.12. (a) TEM image with EELS zero-loss mode of Figure 4.11a. (b)

EELS carbon mapping of area Figure 4.11a.

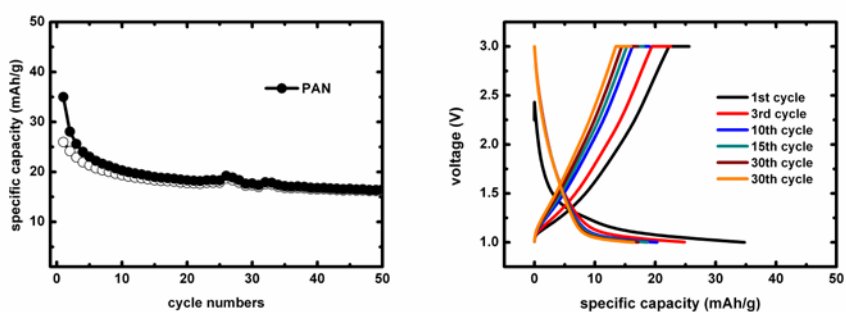


Figure 4.13. Cyclic capacity and voltage profile of an electrode manufactured with stabilized PAN, acetylene black, and PVDF following the same configuration, treatment, and electrochemical parameters as our stabilized PAN-FeS₂ electrodes, respectively. It is shown that stabilized PAN is electrochemically stable within a voltage window of 1V to 3V.

4.3.4 Detailed dq/dv analysis of PAN-FeS₂ and bare FeS₂.

We use dQ/dV analysis to differentiate the direct reduction of sulfur from the reduction of ortho-FeS₂. It is important to acknowledge that an all-solid-state sulfur battery exhibits one discharge plateau [36] while a liquid sulfur battery exhibits two discharge plateaus [37]. The explanation for this difference can be explained by the nature of sulfur's intermediary species. The reduction of sulfur follows a three step process (Figure 4.14) [37]. During the first step represented by Eq. (4.6) the reduction of elemental sulfur produces highly soluble polysulfide species. The average potential of the first reaction step is 2.4V because the reaction kinetics is fast due to the mobility and molecular nature of the polysulfides. During the second step represented by Eq. (4.7) further reduction of the soluble polysulfides results in the precipitation of Li₂S₂. The downward arrow indicates that Li₂S₂ is a solid precipitate. And finally, during the third step represented by Eq. (4.8) Li₂S₂ is



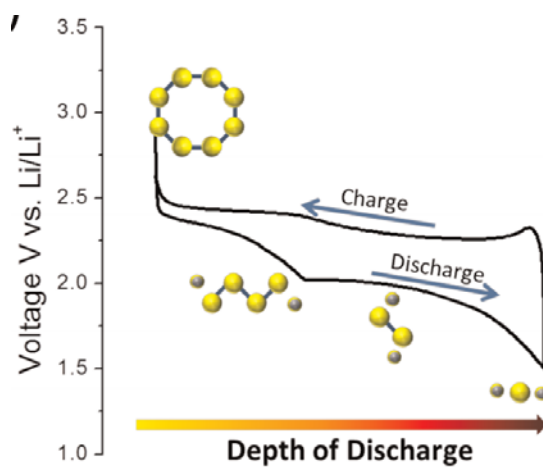


Figure 4.14. The reduction of sulfur in an organic liquid electrolyte follows a three step process. Yellow balls represent sulfur atoms while grey balls represent lithium atoms.

fully reduced to Li_2S . The last two steps of the reaction occur at a lower potential of about 2.1V because the kinetics of these reactions are slower compared to that of the first step. The energy required to nucleate the Li_2S_2 solid phase slows the second step reaction and the third step reaction is limited by the solid state diffusion of Li^+ . In an all-solid-state battery the polysulfides produced during the first step reaction are confined by the glass electrolyte and the reaction is limited by the solid state diffusion of Li^+ to the immobile polysulfides. Slower transport results in overpotential so that the first reaction step occurs at the same potential as the second and third reaction steps.

To support this theory we also provide the Li - S phase diagram in Figure 4.15 [38]. From this it is evident that there are no intermediary phases between Li and Li_2S at room temperature and that there is a two phase region between the compositions of S and Li_2S . The observation of Li_2S_2 in the reduced Li - S electrodes of other studies can be explained by the fact that Li_2S_2 is metastable. Metastable phases are not thermodynamically stable and therefore they will not be present in thermodynamic phase diagrams. From Gibb's phase rule we know that the reduction of sulfur should occur at

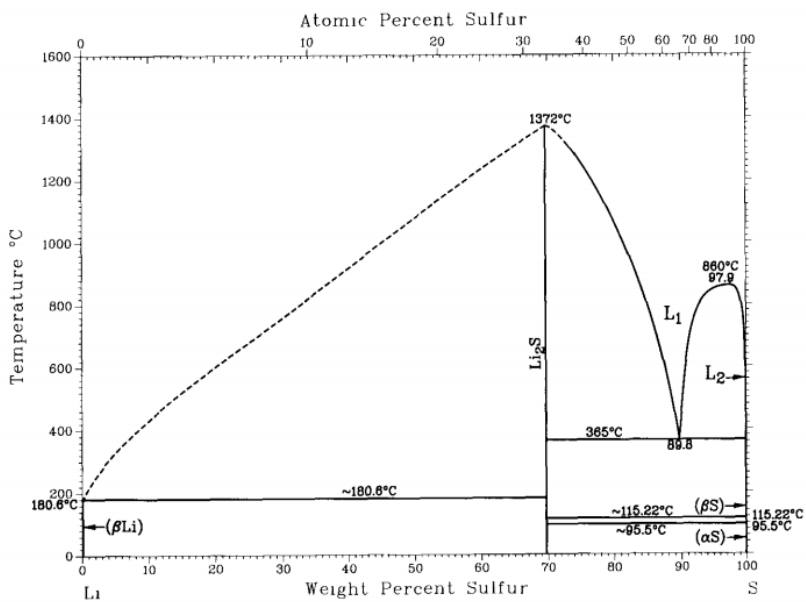


Figure 4.15. Li - S phase diagram.

only one voltage plateau, however, in liquid cells we observe two plateaus. As stated before, the kinetics of sulfur reduction explain the two voltage plateaus and not the presence of two phase regions. In an all-solid-state battery architecture the reduction of sulfur is always limited by the solid-state diffusion of lithium ions and there is no initial kinetic benefit because polysulfides are not mobile. To further support this theory, two other studies examined the electrochemical properties of PAN-S and PANi-S electrodes in liquid cells [39, 40]. Because these were liquid batteries it is expected that the reduction of sulfur should exhibit two plateaus, however, sulfur exhibited only one plateau because the polysulfides were confined within the cyclized PAN and PANi polymers. In the PAN-FeS₂ electrode polysulfides are also held immobile so we fully expect that the reduction of sulfur also occurs in one plateau in our case as well.

We have shown that elemental S and Fe are not observed in our stabilized PAN matrix after cycling which verifies the complete confinement of FeS₂'s intermediary electroactive species. However, we still observe some capacity fade. To explain this, some FeS₂ particles are not fully embedded within our stabilized PAN matrix during material preparation so they are

subject to attack by the liquid electrolyte during cycling. To fully coat every particle, we propose a direct electrode blading with stabilized PAN as previously described [32]. In this way, partially embedded FeS₂ particles will be protected by a secondary protective coating of stabilized PAN.

As stated earlier, FeS_y and S were generally believed to be the final charge products of a low temperature FeS₂ battery [7]. Reductive dQ/dV analysis in the range of 1.8V to 2.8V (Figure 4.16) can be used to differentiate the direct reduction of S from the reduction of ortho-FeS₂ and lend further support to the validity of Equation 5. Figure 4.15 provides the dQ/dV for both PAN-FeS₂ and bare FeS₂ in the whole voltage range of 1V – 3V. As expected we observe three peaks in the range 2.0 to 2.5 V: one for ortho-FeS₂ (2.1 V) and two for sulfur (2.2 V and 2.5 V). The peak at 2.5 V is not a side reaction because if it were it would have also been observed during the initial discharge, however, because sulfur was not yet present the peak is also not present. The peak at 2.1 V corresponds to the reduction of ortho-FeS₂ to Li₂FeS₂ (Eq.(4.1)) whereas the peaks at 2.5 and 2.2 V correspond to the reduction of S (Equations 6, 7, and 8). During the initial discharge the reduction of cubic-FeS₂ occurs at 1.5 – 1.7 V, while on subsequent cycles the

reduction of ortho-FeS₂ occurs at 2.1 V. The explanation for the difference may be related to a change in microstructure or kinetics [11].

In a liquid cell the direct reduction of sulfur occurs in two steps even though the thermodynamic phase diagram suggests only one plateau. The reduction of S follows a three step process as presented below [20]. The first step, Eq. (4.6) occurs at a higher voltage than the other two steps because the mobility and molecular nature of the polysulfides improves the reaction kinetics. Sulfur does not exhibit two plateaus in an all-solid-state structure because polysulfides are confined such that their reduction does not enjoy a kinetic advantage. The presence of two sulfur plateaus for PAN-FeS₂ suggests that some polysulfides are mobile in the liquid electrolyte and that the confinement of FeS₂ is incomplete. This corroborates our previous observation that some FeS₂ particles are not fully embedded in the PAN matrix.

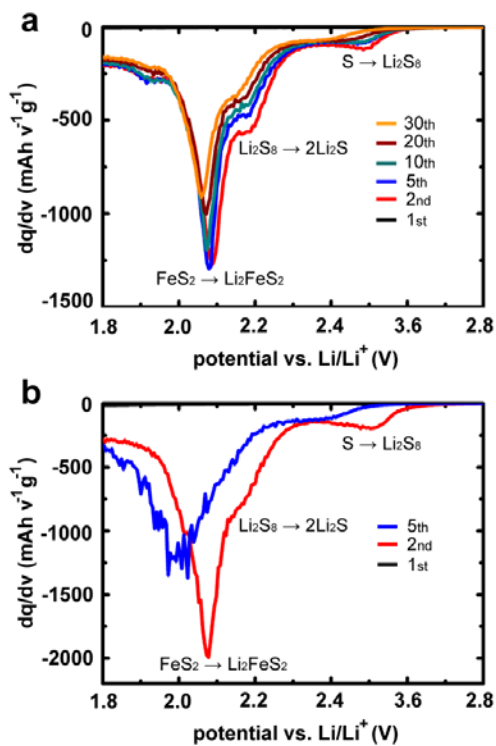


Figure 4.16. (a) Reductive dQ/dV profiles for the PAN- FeS_2 electrode and (b) reductive dQ/dV profiles for the bare FeS_2 electrode. The peaks at approximately 2.5V and 2.2V are attributed to Eq. (4.6) and Eq. (4.7) and Eq. (4.8), respectively, while the peak at approximately 2.1V is attributed to Eq. (4.1).

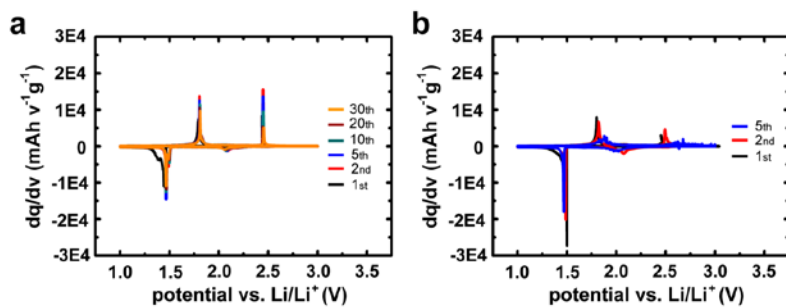


Figure 4.17. (a) Differential capacity versus voltage curve of PAN- FeS_2 . (b)

Differential capacity versus voltage curve of bare FeS_2 .

4.3.5 Experimental section.

First, naturally occurring pyrite (FeS_2 , Alfa Aesar) was mechanically ground at 400 RPM for 1 hour using a planetary ball mill (Across International) in order to reduce the average particle size. Next, ball milled FeS_2 and PAN (MW = 150,000 g mol⁻¹, Sigma Aldrich) were mixed in a mass ratio of 7:3, respectively, using a mortar and pestle. The mixture was then dissolved in N, N-dimethylformamide (DMF, 99%, Alfa Aesar), stirred via magnetic stirring for 6 hours, and then dried overnight. The stabilization of PAN followed a two-step process. The dried PAN- FeS_2 mixture was first heat treated in air at 200°C for 1 hour (Thermolyne) and then heat treated under Ar flow at 500°C for 1 hour (Thermo Scientific). The heating and cooling rate for each heat treatment was 1.66 °C per minute [33].

After preparing the PAN- FeS_2 composite via a two-step heat treatment in air at 200°C and in Ar flow at 500°C, it was then desired to observe how effectively FeS_2 was embedded in stabilized PAN and if FeS_2 decomposed or reacted with PAN. Evidence for the conjugation and intrinsic electronic conduction of stabilized PAN is shown in Figure 4.18.

Cathode slurry was prepared by combining PAN- FeS_2 , acetylene black

(Alfa Aesar), and PVDF (poly (vinylidene fluoride), Alfa Aesar) binder in a 60:20:20 weight ratio, respectively, with a 1-methyl-2-pyrrolidinone (NMP, Alfa Aesar) solvent. The slurry was coated on Al foil, dried under air, and then calendared. On average, the FeS₂ active material loading is 1.5 mg cm⁻², and the area of each of the tested electrodes was of 1.33 cm². Test coin cells (2032, Pred Materials) were assembled with the prepared PAN-FeS₂ working electrode, a lithium metal foil counter electrode (Alfa Aesar), a glass fiber separator (Whatman, GF/G), and 1.5 M LiPF₆ in ethylene carbonate, diethyl carbonate (50:50, Soulbrain) electrolyte. The test cells were cycled using a constant current, constant voltage (CCCV) testing protocol between the voltage range of 1 V and 3 V at a constant rate of 0.1C. The voltage is held constant at 3V at the end of each charging cycle for 30 minutes.

The microstructure of PAN-FeS₂ structure was investigated by analytical TEM (TECNAI F20 equipped with EELS) operating at 200 keV. As previously described, the TEM samples were prepared by sectioning a cycled electrode using a FIB's Ga⁺ ion beam (FEI, NOVA200 dual beam system) [41].

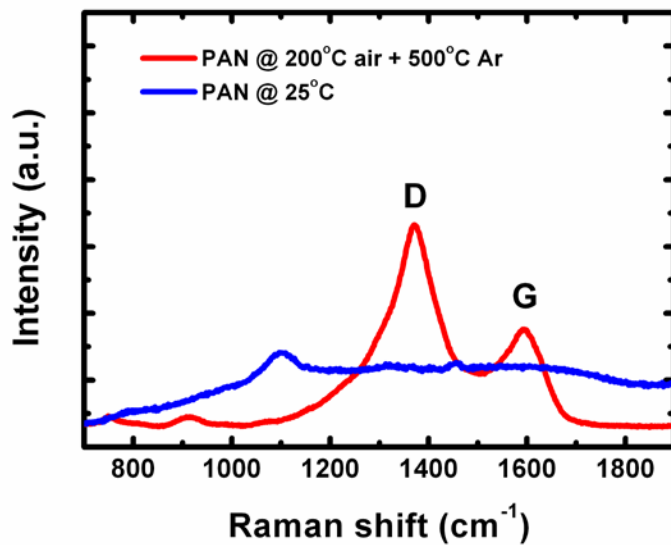


Figure 4.18. Raman spectra for untreated PAN (blue) and PAN treated at 200°C in air for 1 hour and then at 500°C under Ar flow for 1 hour (red). The observation of graphite D and G bands confirms delocalized sp² π bonding which confirms a good intrinsic electronic conductivity and a conjugated structure [32].

4.4. Conclusion

In summary, the performance of our PAN-FeS₂ composite cathode suggests that the problems associated with the mobility of FeS₂'s electroactive species can be addressed without the need for a costly all-solid-state battery structure. By the 50th cycle our PAN-FeS₂ electrode delivers 470 mAh g⁻¹, or 64% of its initial discharge capacity with a CE approaching 99.25%. When viewed alongside a recent development regarding dendrite-free lithium metal anodes [42], the results of our stabilized PAN-FeS₂ cathode study suggest that a practical, safe conventional secondary FeS₂/Li battery is close to reality. Moreover, we also observed ortho-FeS₂ (marcasite) as a full charge product which is a first for conventional liquid batteries and validates the results of our previous all-solid-state FeS₂ battery study.

4.5. References

- [1] U. Kasavajjula, C. Wang, A. J. Appleby, *Journal of Power Sources* **2007**, 163, 1003.
- [2] Z. Tomczuk, B. Tani, N. C. Otto, M. F. Roche, D. R. Vissers, *Journal of the Electrochemical Society* **1982**, 129, 925.
- [3] D. Bernardi, J. Newman, *Journal of the Electrochemical Society* **1987**, 134, 1309.
- [4] J. Cabana, L. Monconduit, D. Larcher, M. R. Palacin, *Advanced Materials* **2010**, 22, E170.
- [5] M. S. Whittingham, *Chemical Reviews* **2004**, 104, 4271.
- [6] J. B. Goodenough, *Journal of Power Sources* **2007**, 174, 996.
- [7] R. Fong, J. R. Dahn, C. H. W. Jones, *Journal of The Electrochemical Society* **1989**, 136, 3206.
- [8] Y. J. Choi, N. W. Kim, K. W. Kim, K. K. Cho, G. B. Cho, H. J. Ahn, J. H. Ahn, K. S. Ryu, H. B. Gu, *Journal of Alloys and Compounds* **2009**, 485, 462.
- [9] Y. Shao-Horn, S. Osmialowski, Q. C. Horn, *Journal of the Electrochemical Society* **2002**, 149, A1499.

- [10] D. Aurbach, E. Zinigrad, Y. Cohen, H. Teller, *Solid State Ionics* **2002**, 148, 405.
- [11] T. A. Yersak, H. A. Macpherson, S. C. Kim, V. D. Le, C. S. Kang, S. B. Son, Y. H. Kim, J. E. Trevey, K. H. Oh, C. Stoldt, S. H. Lee, *Advanced Energy Materials* **2013**, 3, 120.
- [12] R. Brec, A. Dugast, A. Le Mehaute, *Mater. Res. Bull.* **1980**, 15, 619.
- [13] D. Golodnitsky, E. Peled, *Electrochimica Acta* **1999**, 45, 335.
- [14] C. H. W. Jones, P. E. Kovacs, R. D. Sharma, R. S. Mcmillan, *J Phys Chem-US* **1991**, 95, 774.
- [15] K. Takada, Y. Kitami, T. Inada, A. Kajiyama, M. Kouguchi, S. Kondo, M. Watanabe, M. Tabuchi, *Journal of The Electrochemical Society* **2001**, 148, A1085.
- [16] R. D. Rauh, F. S. Shuker, J. M. Marston, S. B. Brummer, *Journal of Inorganic & Nuclear Chemistry* **1977**, 39, 1761.
- [17] R. D. Rauh, K. M. Abraham, G. F. Pearson, J. K. Surprenant, S. B. Brummer, *Journal of the Electrochemical Society* **1979**, 126, 523.
- [18] B. L. Ellis, K. T. Lee, L. F. Nazar, *Chemistry of Materials* **2010**, 22, 691.
- [19] X. L. Ji, K. T. Lee, L. F. Nazar, *Nature Materials* **2009**, 8, 500.

- [20] X. L. Ji, L. F. Nazar, *J Mater Chem.* **2010**, 20, 9821.
- [21] K. Takada, K. Iwamoto, S. Kondo, *Solid State Ionics* **1999**, 117, 273.
- [22] S. Y. Huang, X. Y. Liu, Q. Y. Li, J. Chen, *Journal of Alloys and Compounds* **2009**, 472, L9.
- [23] E. Peled, D. Golodnitsky, G. Ardel, J. Lang, Y. Lavi, *J Power Sources* **1995**, 54, 496.
- [24] E. Strauss, D. Golodnitsky, K. Freedman, A. Milner, E. Peled, *J Power Sources* **2003**, 115, 323.
- [25] E. Strauss, D. Golodnitsky, E. Peled, *Electrochim Acta* **2000**, 45, 1519.
- [26] D. Zhang, X. L. Wang, Y. J. Mai, X. H. Xia, C. D. Gu, J. P. Tu, *J Appl Electrochem* **2012**, 42, 263.
- [27] D. Zhang, Y. J. Mai, J. Y. Xiang, X. H. Xia, Y. Q. Qiao, J. P. Tu, *J Power Sources* **2012**, 217, 229.
- [28] D. Zhang, J. P. Tu, Y. J. Mai, J. Zhang, Y. Q. Qiao, X. L. Wang, *J Aust Ceram Soc* **2012**, 48, 189.
- [29] J. Fanous, M. Wegner, J. Grimminger, A. Andresen, M. R. Buchmeiser, *Chemistry of Materials* **2011**, 23, 5024.
- [30] C. Wang, T. Sakai, O. Watanabe, K. Hirahara, T. Nakanishi, *Journal of*

The Electrochemical Society **2003**, 150, A1166.

[31] X. G. Yu, J. Y. Xie, J. Yang, H. J. Huang, K. Wang, Z. S. Wen, J

Electroanal Chem **2004**, 573, 121.

[32] D. M. Piper, T. A. Yersak, S. B. Son, S. C. Kim, C. S. Kang, K. H. Oh, C.

M. Ban, A. C. Dillon, S. H. Lee, *Adv Energy Mater* **2013**, 3, 697.

[33] M. S. A. Rahaman, A. F. Ismail, A. Mustafa, *Polym Degrad Stabil* **2007**,

92, 1421.

[34] S.-B. Son, S. C. Kim, C. S. Kang, T. A. Yersak, Y.-C. Kim, C.-G. Lee, S.-

H. Moon, J. S. Cho, J.-T. Moon, K. H. Oh, S.-H. Lee, *Advanced Energy*

Materials **2012**, 2, 1226.

[35] I. C. Hoare, H. J. Hurst, W. I. Stuart, T. J. White, *Journal of the Chemical*

Society-Faraday Transactions I **1988**, 84, 3071.

[36] M. Nagao, A. Hayashi, M. Tatsumisago, *Electrochimica Acta* **2011**, 56,17.

[37] S. Evers, L.F. Nazar, *Accounts of Chemical Research* **2012**, 46, 5.

[38] Li-S binary phase diagram

[39] J. Wang, J. Yang, J. Xie, N. Xu, *Advanced Materials* **2002**, 14, 13.

[40] J. Wang, J. Yang, C. Wan, K. Du, J. Xie, N. Xu, *Advanced Functional*

Materials **2003**, 13, 6.

- [41] S. B. Son, J. E. Trevey, H. Roh, S. H. Kim, K. B. Kim, J. S. Cho, J. T. Moon, C. M. DeLuca, K. K. Maute, M. L. Dunn, H. N. Han, K. H. Oh, S. H. Lee, *Adv Energy Mater* **2011**, 1, 1199.
- [42] F. Ding, W. Xu, G. L. Graff, J. Zhang, M. L. Sushko, X. Chen, Y. Shao, M. H. Engelhard, Z. Nie, J. Xiao, *Journal of the American Chemical Society* **2013**, 135, 4450.

Conclusion

Microstructure observation of electrochemically driven Li_xSi

In this research, we observed micro structure of lithiated Si anode in all solid state Li ion battery. XRD analysis is performed to figure out phase variation of Si anode sample during Li insertion. XRD patterns show that crystalline Si undergoes amorphization while lithiated and forms crystalline phase after fully discharged which is known as $\text{Li}_{15}\text{Si}_4$. FIB equipped with air-lock system is used for TEM sample preparation. No oxygen signal in EDS result infers that the sample was not exposed by air during loading and unloading the samples. Clear two-phase region is observed by HRTEM at the first time showing amorphous Li_xSi and crystalline Si. HRTEM observation of fully discharged Si anode sample reveals that particle is consisting of high portion of pores at the surface which is responsible for cracks and pulverization of Si particle due to Li insertion.

Highly reversible nano-Si anode embedded in $\text{Ti}_4\text{Ni}_4\text{Si}_7$ matrix

We embed nano-Si in a $\text{Ti}_4\text{Ni}_4\text{Si}_7$ matrix for three reasons. First, because the $\text{Ti}_4\text{Ni}_4\text{Si}_7$ matrix limits the extent of Si lithiation. At STN's fully discharged state, one mole of Si is lithiated with 2.7 moles of Li ions ($\text{Li}_{2.7}\text{Si}$)

instead of the 3.7 moles of Li ions ($\text{Li}_{15}\text{Si}_4$) in a typical Si electrode. Limiting the extent of lithiation minimizes the maximum stress generated by reducing the volume expansion experienced by a Si particle. Secondly, because the $\text{Li}_x\text{Ti}_4\text{Ni}_4\text{Si}_7$ matrix facilitates fast and efficient Li ion and electron transfer to nano-Si. We find that $\text{Li}_x\text{Ti}_4\text{Ni}_4\text{Si}_7$ functions as solid state ionic conductor and an electronic conductor as well. And finally, the $\text{Li}_x\text{Ti}_4\text{Ni}_4\text{Si}_7$ matrix helps to reduce the formation of an SEI layer on the Si surface. The formation of a SEI layer on the surface of active materials typically increases interfacial resistance to charge transfer and also lowers the CE. Therefore, reducing the exposed active Si surface area will mitigate the parasitic reaction responsible for SEI layer formation. The $\text{Li}_x\text{Ti}_4\text{Ni}_4\text{Si}_7$ matrix coats much of the nano-Si surface and prevents the reduction of the organic electrolyte. This protection enables our system to have better mass transfer kinetics and a high CE. As a result, our STN demonstrates a specific capacity in excess of 900 mAh g^{-1} after the 50th discharge-charge cycle and a CE of 99.7% at a rate of 1C.

Improved cycle stability of Li/FeS₂ system using PAN confinement

We have developed PAN-FeS₂ by confining natural FeS₂ particles into a PAN host matrix. We proposed that by using PAN we decelerate polysulfide dissolution into the liquid electrolyte making FeS₂ conversion chemistry more stable and reversible. As far as resolving the exact mechanism on how the polysulfide retardation occurs in the PAN matrix has yet to be elucidated. We observed through TEM that our PAN acted as a buffer layer capturing polysulfides and preventing their direct dissolution to the liquid electrolyte. Moreover, we also observed the production of orthorhombic-FeS₂ at charged PAN-FeS₂ validating our previous work using an all-solid-state configuration. To this end, we have demonstrated that a PAN confinement closely relates to our previous all-solid-state architecture where mobility and dissolution of our electro-active species is prevented and thus, improves the reversibility of the Li/FeS₂ system with liquid electrolyte at ambient temperature. This work also emphasizes the possibility of a rechargeable Li/FeS₂ battery.

요약 (국문 초록)

이 논문에서는 현재 리튬 이온 전지에서 사용 되고 있는 전극 물질을 대체할 수 있는 새로운 전극 물질을 개발하고 그 특성을 평가하는 연구를 진행하였다. Si계 음극과 FeS₂ 양극의 전기화학 특성을 평가하고 전극 재료의 미세조직 분석을 통하여 해당 재료의 전기화학 반응 기구를 이해하는 것을 주 연구 목적으로 하였다.

2장에서는 Si음극이 Li과 반응 시 생기는 미세조직과 상의 변화에 대하여 연구하였다. 투과전자현미경을 이용하여 Si이 Li과 반응 시 초기에는 표면부분에 비정질의 Li_xSi층이 생성되며 내부에는 Li과의 반응이 진행되지 않은 결정질의 Si층이 남아있음을 확인하였다. Li과의 반응이 다 진행된 후에는 Si음극 내부에 많은 공공이 형성되어 있음을 확인할 수 있었으며 공공의 수는 표면보다 내부에 더 많이 형성되어 있음을 확인하였다. 화학역학 전산모사를 이용하여 Si이 Li과 반응할 시 일어나는 기계적 파괴거동을 모사 및 이해하였고, 이를 바탕으로 본 연구 결과가 새로운 Si계 음극재료를 개발하는데 있어 기초자료로

활용될 것으로 기대되는 바이다.

3장에서는 Si-Ti-Ni 3원계 합금을 리튬 이온 전지의 음극으로 개발하고 그 전기화학 성능을 평가하였다. Si-Ti-Ni 음극은 50회의 충방전 이후에도 900 mAh g^{-1} 이상의 용량을 보이는 것으로 확인되었으며 Coulombic 효율 또한 99.7%의 높은 효율을 보이는 것으로 확인되었다. Si-Ti-Ni의 제작은 멜트 스피닝 방법을 이용하였으며, 이 방법을 이용하여 나노 Si입자를 $\text{Ti}_4\text{Ni}_4\text{Si}_7$ 지지상이 둘러싸는 조직을 구현하였다. $\text{Ti}_4\text{Ni}_4\text{Si}_7$ 지지상은 Si이 Li과 반응할 시 생성되는 응력의 수준을 낮추어 줄 뿐만 아니라 Si입자가 전해질과 직접 반응하지 않도록 하여 부 반응층의 생성을 방지하면서 전기 및 이온 전도체로서 역할도 하게 되는 것으로 확인되었다. Si계 음극의 경우, 99.5% 이상의 Coulombic 효율은 거의 보고된바 없음을 고려할 때, Si-Ti-Ni 합금이 리튬 이온 전지의 음극으로서 새로운 가능성을 제시하고 있다고 할 수 있다.

4장에서는 고분자 PAN을 이용하여 FeS_2 양극을 코팅하였으며, 이를 이용하여 FeS_2 와 충방전 실험 중 발생하는 중간 반응물인 Fe^0 와 S_n^{2-} 를 구속하여 높은 효율의 가역적인 전기화학 반응이 계속하여 일어날 수 있도록 하였다. PAN- FeS_2 전극은 상온에서 50회의 충방전

이후에도 약 470 mAh g^{-1} 의 용량을 보이는 것으로 나타났다. 투과전자 현미경을 이용하여 10회 충전후의 FeS_2 조직을 관찰하였으며, 그 결과 초기 FeS_2 가 cubic 조직을 가지고 있던 반면 10회 충전 후에는 orthorhombic 조직을 갖고 있는 FeS_2 가 검출되었다. 이 결과는 상온에서 가역적으로 반응이 이루어지는 고체전해질을 이용한 FeS_2 전극에서 나온 결과와 같은 결과이며, 액체 전해질을 사용하는 FeS_2 전극에서는 처음 밝혀진 결과이다. 본 연구 결과는 아직 리튬 일차전지의 전극으로만 사용되고 있는 FeS_2 가 재충전이 가능한 이차전지의 전극 재료로서 사용이 가능하도록 개발되는데 있어 중요한 기초자료로 사용될 것으로 기대된다.

Curriculum Vitae

Seoung-Bum Son

Department of Materials Science & Engineering,

Seoul National University

Email:sunnn@snu.ac.kr

37-213, 599 Gwanak-Road, Gwank-Gu,

(office): 82-2-880-8306

Seoul, Korea, 151-742

(cell): 82-10-5295-9254

Personal

Full name: **Seoung-Bum Son**

Sex: Male

Date of birth: Feb 02, 1982

Nationality: Republic of Korea

Educations

- Ph.D (M.S/Ph.D. integrated course), Materials Science and Engineering (Mar 2010 - Feb 2014): Seoul National University, Seoul, Korea.
- M.S., Materials Science and Engineering (Mar 2008 - Feb 2010): Seoul National University, Seoul, Korea.
- B.S., Materials Engineering (Feb 2008): Korea Aerospace University, Gyeonggi-do, Korea.

Research experiences

- Visiting Scholar, School of Engineering and Applied Sciences, Harvard University, USA. (Mar 2013)
- Visiting Scholar, Mechanical Engineering, University of Colorado at Boulder, USA. (Aug 2010 - Aug 2012)

Experience

- Military service as Korean Augmentation to the United States Army (Oct 2002 – Nov 2004)

Research Interests

1. Finite Element Method (MSC.PATRAM and Abaqus 6.9) and Numerical approaches on mechanical process. (Drawing process, annealing process and modal analysis)
2. Development and application of focused ion beam machining technology for the preparation of nano structures involving the use of Focused Ion Beam (FIB)
3. Grain characteristic & Texture Analysis of Crystalline thin Film and Metal using Electron Back-Scattered Diffraction (EBSD)
4. Characteristic Analysis of Nano scale materials (powder, particle, thin film,

nanowire and electrodes) using TEM/EDX/EELS.

5. Synthesis of active material and anode/cathode for Lithium Ion Battery and electrochemical/structural analysis of cycled electrode.

Award

- Best Graduate Student award of 2012 year, Brain Korea 21 & Seoul National University.

Journal Publications

1. **Son, S.-B.**, Lee, Y.K., Kang, S.H., Chung, H.-S., Cho, J.S., Moon, J.-T., Oh, K.H., “A numerical approach on the inclusion effects in ultrafine gold wire drawing process”, *Engineering Failure Analysis* 18 (5), pp. 1272-1278, 2011.
2. Jung, H.-G., Myung, S.-T., Yoon, C.S., **Son, S.-B.**, Oh, K.H., Amine, K., Scrosati, B., Sun, Y.-K., “Microscale spherical carbon-coated $\text{Li}_4\text{Ti}_5\text{O}_{12}$ as ultra high power anode material for lithium batteries”, *Energy and Environmental Science* 4 (4), pp. 1345-1351, 2011.
3. **Son, S.-B.**, Roh, H., Kang, S.H., Chung, H.-S., Kim, D.H., Choi, Y.S., Cho, J.S., Moon, J.-T., Oh, K.H., “Relationship between microstructure homogeneity and bonding stability of ultrafine gold wire”, *Gold Bulletin*

44 (4), pp. 231-237, 2011.

4. **Son, S.-B.**, Trevey, J.E., Roh, H., Kim, S.-H., Kim, K.-B., Cho, J.S., Moon, J.-T., DeLuca, C.M., Maute, K.K., Dunn, M.L., Han, H.N., Oh, K.H., Lee, S.-H., “Microstructure Study of Electrochemically Driven Li_xSi ”, *Advanced Energy Materials* 1 (6), pp. 1199-1204, 2011.
5. Lee, B.-S., **Son, S.-B.**, Park, K.-M., Yu, W.-R., Oh, K.-H., Lee, S.-H., “Anodic properties of hollow carbon nanofibers for Li-ion battery”, *Journal of Power Sources* 199, pp. 53-60, 2012.
6. Lee, B.-S., **Son, S.-B.**, Park, K.-M., Seo, J.-H., Lee, S.-H., Choi, I.-S., Oh, K.-H., Yu, W.-R., “Fabrication of Si core/C shell nanofibers and their electrochemical performances as a lithium-ion battery anode”, *Journal of Power Sources* 206, pp. 267-273, 2012.
7. **Son, S.-B.**, Kim, S.C., Kang, C.S., Yersak, T.A., Kim, Y.-C., Lee, C.-G., Moon, S.-H., Cho, J.-S., Moon, J.-T., Oh, K.H., Lee, S.-H., “A highly reversible nano-si anode enabled by mechanical confinement in an electrochemically activated $\text{Li}_x\text{Ti}_4\text{Ni}_4\text{Si}_7$ matrix”, *Advanced Energy Materials* 2 (10), pp. 1226-1231, 2012.
8. Cho, J.-S., Yoo, K.-A., Moon, J.-T., **Son, S.-B.**, Lee, S.-H., Oh, K.-H., “Pd Effect on Reliability of Ag Bonding Wires in Microelectronic Devices in High-Humidity Environments”, *Metal and Materials International* 18, 5,

pp. 881~885, 2012.

9. Lee, B.-S., **Son, S.-B.**, Park, K.-M., Lee, G., Oh, K.H., Lee, S.-H., Yu, W.-R., “Effect of Pores in Hollow Carbon Nanofibers on Their Negative Electrode Properties for a Lithium Rechargeable Battery”, *Applied Materials and Interfaces* 4 (12), pp. 6701~6709, 2012.
10. Yersak, T.A., Macpherson, H.A., Kim, S.C., Le, V.-D., Kang, C.S., **Son, S.-B.**, Kim, Y.-H., Trevey, J.E., Oh, K.H., Stol dt, C., Lee, S.-H., “Solid State Enabled Reversible Four Electron Storage”, *Advanced Energy Materials* 3 (1), pp. 120-127, 2013.
11. Lee, B.-S., **Son, S.-B.**, Seo, J.-H., Park, K.-M., Lee, G., Lee, S.-H., Oh, K.H., Ahn, J.-P., Yu, W.-R., “Facile conductive bridges formed between silicon nanoparticles inside hollow carbon nanofibers”, *Nanoscale* 5 (11), PP. 4790-4796, 2013.
12. Piper, D.M., Yersak, T.A., **Son, S.-B.**, Kim, S.C., Kang, C.S., Oh, K.H., Ban, C., Dillon, A.C., Lee, S.-H., “Conformal Coatings of Cyclized-PAN for Mechanically Resilient Si nano-Composite Anodes”, *Advanced Energy Materials* 3 (6), pp. 697-702, 2013.
13. Lee, B.-S., Seo, J.-H., **Son, S.-B.**, Kim, S.C., Choi, I.-S., Ahn, J.-P., Oh, K.H., Lee, S.-H., Yu, W.-R., “Face-Centered-Cubic Lithium Crystals Formed in Mesopores of Carbon Nanofiber Electrodes”, *ACS NANO* 7 (7),

pp 5801-5807, 2013.

14. Yersak, T.A., **Son, S.-B.**, Cho, J.S., Suh, S.-S., Kim, Y.-U., Moon, J.-T., Oh, K.H., Lee, S.-H., “An all-solid-state Li-ion battery with a pre-lithiated Si-Ti-Ni alloy anode”, *Journal of the Electrochemical Society* 160, pp A1497-A1501, 2013.
15. Zhang, Z., Molina Piper, D., **Son, S.-B.**, Kim, S.C., Oh, K.H., Lee, S.-H., Ding, Y., “Carbon nanopatterns and nanoribbons from directly nanoimprinted polyacrylonitrile: Correlation between crystallite orientation and nanoimprint process”, *Polymer* 54, pp. 5936-5941. 2013.
16. **Son, S.-B.**, Yersak, T.A., Piper, D.M., Kim, S.C., Kang, C.S., Cho, J.S., Suh, S.-S., Kim, Y.-U., Oh, K.H., Lee, S.-H., “A stabilized PAN-FeS₂ cathode with an EC/DEC liquid electrolyte”, *Advanced Energy Material*, *in press*.
17. Piper, D.M., Travis, J.J., Young, M., **Son, S.-B.**, Kim, S.C, Oh, K.H, George, S.M., Ban, C., Lee, S.-H., “Reversible High Capacity Si Nanocomposite Anodes enabled by Molecular Layer Deposition”, *Advanced Materials*, *in press*.

Presentations

1. **S.-B. Son**, S. C. Kim, H.-S. Chung, D. H. Kim, K. H. Oh, “Synthesis of

Physical Evaporated β -Ga₂O₃ Nanowires”, **Poster Presentation**, MRS 2008 Fall Meeting, Boston, USA.

2. **S.-B. Son**, S. H. Kang, D. H. Kim, J. H Kim, H. Roh, J. S. Cho, J.-T. Moon, H.-S. Chung, K. H. Oh, “Asymmetric texture evolution of the gold wire and its effect on leaning problem”, **Poster Presentation**, MRS 2010 Spring Meeting, San Francisco, USA.

3. **Son, S.-B.**, Trevey, J.E., Roh, H., Kim, S.-H., Kim, K.-B., Cho, J.S., Moon, J.-T., DeLuca, C.M., Maute, K.K., Dunn, M.L., Han, H.N., Oh, K.H., Lee, S.-H., “Microstructure Study of Electrochemically Driven Li_xSi”, **Oral Presentation**, MRS 2012 Spring Meeting, San Francisco, USA.

4. **Son, S.-B.**, Kim, S.C., Kang, C.S., Yersak, T.A., Kim, Y.-C., Lee, C.-G., Moon, S.-H., Cho, J.-S., Moon, J.-T., Oh, K.H., Lee, S.-H., “A highly reversible nano-si anode enabled by mechanical confinement in an electrochemically activated Li_xTi₄Ni₄Si₇ matrix”, **Oral Presentation**, MRS 2012 Fall Meeting, Boston, USA.

Technical Proficiency

- Microstructures and texture analysis by using EBSD
- Thermal, mechanical stresses analysis by using FEM
- 3-Dimensional nano-sized material processing by using FIB

- Chemical composition analysis by using EDS
- Nano- and micro-structures analysis by using TEM and EELS
- Fabrication and evaluation of Li ion battery.

Appendix 1. Published paper during master's degree

Engineering Failure Analysis 18 (2011) 1272–1278



Contents lists available at ScienceDirect

Engineering Failure Analysis

journal homepage: www.elsevier.com/locate/engfailanal



A numerical approach on the inclusion effects in ultrafine gold wire drawing process

Seoung-Bum Son^a, Young Kwang Lee^a, Suk Hoon Kang^b, Hee-Suk Chung^c, Jong Soo Cho^{a,d}, Jeong-Tak Moon^d, Kyu Hwan Oh^{a,*}

^aDepartment of Materials Science and Engineering, Seoul National University, Seoul 151742, Republic of Korea

^bNuclear Materials Research Division, Korea Atomic Energy Research Institute, 1045 Daedeok-daero, Yuseong-gu, Daejeon 305353, Republic of Korea

^cDepartment of Materials Science and Engineering, University of Pennsylvania, 3231 Walnut Street, Philadelphia, PA 19104, USA

^dMK Electron, 316-2 Geumeo-ri Pogok-myeon Yongin-si, Gyeong gi-do 449810, Republic of Korea

ARTICLE INFO

Article history:

Received 15 July 2010

Received in revised form 12 March 2011

Accepted 23 March 2011

Available online 31 March 2011

Keywords:

Wire drawing stress

Inclusion

Finite element method

ABSTRACT

This study examined the effects of inclusions on the gold wire drawing stress using the Finite Element Method (FEM). Al_2O_3 and SUS304 are used as the model inclusion materials, which are frequently found on the fracture surfaces of drawn wire. The wire drawing stress showed a strong correlation with the size and yield stress of the inclusions. In the case of Al_2O_3 , a larger diameter induced more drawing stress in the wire, whereas in case of SUS304, a larger diameter induced less drawing stress in wire. The difference was estimated quantitatively by comparing the amount of equivalent plastic strain (PEEQ) in the wire, which is the result of an interaction between the wire and inclusion. This result shows that the reason of difference in drawing stress variation is due to the yield stress of the inclusion.

© 2011 Elsevier Ltd. All rights reserved.

1. Introduction

Bonding wires have been utilized as electronic signal paths between integrated circuits and printed circuit boards in electronic packaging processes under thermal–mechanical stress [1]. Therefore, stable electric conductivity with high reliability of the bonding wire is a major consideration when choosing the appropriate material for a bonding wire [2]. Gold is one of the most promising materials for bonding wires because of its superior reliability and sufficiently low electric resistivity. These facts have attracted continuous interest in ultrafine gold bonding wires [3].

Cold drawing is a common method for fabricating bonding wires with ultra fine diameters, which involves a large number of wire diameter reduction steps to prevent wire breaks. Along the drawing process to an ultrafine diameter, the cross section of the gold wire is subject to severe plastic strain when the diameter of gold wire is reduced when being passed through the die. Heat treatment during the drawing process is also used to gain a better plasticity of the bonding wire [4].

Many studies dealing with the optimum wire drawing condition have been published, including the die reduction angle [5], die reduction ratio [6], die reduction length, wire drawing speed, friction coefficient [7] and annealing condition. In particular, the inclusion effect has focused on the wire drawing process and there has been a gradual increase in interests in the inclusion effect.

Inclusions in a bonding wire are normally classified by their originality and locations. Exogenous inclusions originate from the accidental entrapment of external bodies, such as particles from dies, furnaces and intrusions of other defects

* Corresponding author. Tel: +82 2 880 8785; fax: +82 2 872 8307.

E-mail address: kyuhwan@snu.ac.kr (K.H. Oh).

originating from the drawing system and process. Although these inclusions cause serious problems in wire drawing due to their size, they comprise only few portions of breakage in the bonding wire. However, indigenous inclusions are formed because of the intrusion of other materials or compositional differences in the molten state of material. In the drawing process, these inclusions and surrounding areas have different drawing characteristics from the bulk materials, and this interference to wire drawing from the inclusions are caused by their material properties and size.

Despite the development of purification methods for raw materials, wire breakage due to the presence of inclusions increases sharply until the wire diameter reaches $<15 \mu\text{m}$ in diameter [8]. Many studies have examined copper wire breakage and reported that more than half of wire breakage problems are caused by inclusions [9–11].

The explosive demand for miniaturized electronic devices in the semiconductor market had prompted extensive research into methods to reduce the diameter of the bonding wire and overcome the current processing limits. In these days, wires with diameters of $15\text{--}20 \mu\text{m}$ are mainly used. Moreover, a finer gold wire could be beneficial for a size reduction as well as a cost reduction of the material. Although there are ongoing studies on the drawing characteristics with inclusions on gold bonding wires, the drawing characteristics of $<15 \mu\text{m}$ diameter of gold wire is still needed to reach miniaturized electronic devices. In this regard, this study examined the inclusion effect on gold bonding wire in a view of the drawing stress and PEEQ using FEM.

2. Analytical and FEM method in wire drawing

Two categories, the force equilibrium method and energy analysis, are mainly cited for theoretical considerations of the drawing processes. Force equilibrium analysis has generally been in more common use because of its relatively simple and considerable accuracy compared to energy analysis, even though energy analysis has the advantages of being easily comprehensive [12].

According to Sachs, drawing stress in the wire drawing process considering force equilibrium analysis can be expressed using the following equation:

$$\sigma_x/Y = [(1+B)/B] [1 - (1-r)^B] \quad (1)$$

where σ_x is the drawing stress, Y is the yield stress of material, B is the $\mu \cot \alpha$, μ is the friction coefficient, α is the die reduction angle, and r is the reduction of area, which is given by

$$r = (A_1 - A_2)/A_1 \quad (2)$$

where A_1 and A_2 are the inlet and exit areas of the wire, respectively [13]. Fig. 1 shows a schematic diagram of the force equilibrium method.

FEM analysis, which can provide precise stress and strain values, is used widely in the metal forming processes [14]. Rubio et al. already reported a numerical formula to calculate the drawing force using NFORC, which is a nodal variable code from ABAQUS. The forces at the nodes of the element caused by stress in the element are identified by NFORC [15]. However, in the present study, the total forces of the nodes in the end of wire element were considered to calculate the wire drawing force. The total force identifies the combined reaction force and point load at a specified node in ABAQUS.

3. Finite element analysis

All simulations were carried out using ABAQUS 6.5 software. Fig. 2 shows the wire meshes assumption and force applied nodes. The axis symmetric model was applied to reduce the computational cost, and indigenous inclusions which are positioned mainly at the center of the wire were considered for the FEM. A wire diameter of $14 \mu\text{m}$ was used, and the reduction angle and reduction ratio of the wire drawing were designated as 6° and 6% in all simulation cases, respectively. Fig. 2 shows the model used in this study and the inclusion size ratio to the gold wire diameter (d_i/d_w) was determined to be 0.2, 0.4 and 0.6 to determine of the change in drawing stress and equivalent plastic strain distribution on the inclusion size.

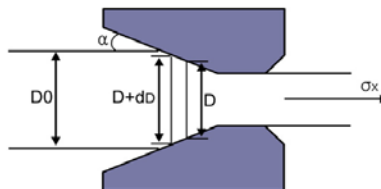


Fig. 1. Force equilibrium analysis in wire drawing.

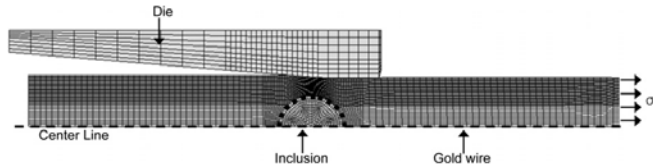


Fig. 2. Gold wire and inclusion meshes assumption and force applied nodes.

Table 1
Mechanical properties of gold, Al_2O_3 , and SUS304.

Materials	Parameter	Value	Unit
Gold	Young's modulus (E)	62,727	MPa
	Yield stress (σ_y)	484	MPa
	Poisson's ratio (ν)	0.44	–
Al_2O_3	Young's modulus (E)	370,000	MPa
	Poisson's ratio (ν)	0.22	–
SUS304	Young's modulus (E)	200,000	MPa
	Yield stress (σ_y)	289.6	MPa
	Poisson's ratio (ν)	0.29	–

Table 1 lists the mechanical properties used in this study. Due to several wire drawing processes, the gold wire was extensively work hardened and showed different properties from pure gold.

4. Results and discussion

Generally, wires containing inclusions do not display a considerable mechanical properties difference from the pure material. However, inclusions and their boundary area show different distribution of stress and strain at the wire diameter reduction area, which leads to wire breakage during wire processing. In this regard, Al_2O_3 and SUS304 are concerned as inclusion materials for our numerical approaches as both inclusions are the most frequently found on the wire surface fracture. Fig. 3a and b shows cross-sectional SEM images of the failed drawing gold wire corresponding to its Energy Dispersive Spectroscopy (EDS) spectrum. The EDS spectra in Fig. 3a and b show Al and Fe in the cross-section area, which can cause wire breakage during the drawing process.

Fig. 4a shows that Al_2O_3 inclusions in the gold wire do not deform in the wire diameter reduction area. However, the boundary area of the inclusions shows severe deformation to make up the reduction ratio in the reduction area by the distribution of PEEQ. In the case of $d_i/d_w = 0.2$, approximately 0.325 of PEEQ was observed at the boundary of the gold wire and inclusion (d_i means diameter of inclusion and d_w means diameter of wire). The Al_2O_3 inclusion does not show any PEEQ due to its relatively high strength. In the case of $d_i/d_w = 0.4$, the PEEQ at the boundary of the inclusion increased to 0.65, and most of the strain is concentrated on the inclusion boundary area. When the diameter of a 60% inclusion relative to the wire diameter was concerned in a gold wire drawing process, a relatively higher PEEQ of up to 1.23 was observed at the boundary area of the inclusion. Moreover, more PEEQ was concentrated on the front area of the inclusion than on the back side along the wire drawing direction. In the case of copper wire drawing, necking was initiated on the surface of the wire at the boundary area in front of the inclusions and both copper and gold wires showed a similar stress and strain distribution at the boundary area of the wire and inclusions [16,17].

Fig. 4b shows the drawing stress change depending on the Al_2O_3 inclusion size during the drawing process (σ_i means the wire drawing stress with inclusions and σ means the wire drawing stress without inclusions). In the case of $d_i/d_w = 0.2$, the wire drawing stress did not show an obvious difference when the inclusion was passed through the dies. However, the σ_i value in the wire diameter reduction area increased by a factor of 1.15 and 1.5 when the relative diameter of the inclusion was 40% and 60%, respectively. In the wire diameter reduction area, a larger Al_2O_3 inclusion means that the gold wire is forced to have smaller area for wire diameter reduction and indicates bigger PEEQ, which can explain why wire drawing with larger inclusions produces higher drawing stress in gold drawing wire.

However, in the case of SUS304, inclusions in the gold wire are unable to keep its original shape and deform. SUS304, which has lower yield stress (289.6 MPa) than the work hardened gold wire (484 MPa), is forced to undergo more deformation than the surrounding matrix area when the inclusion is passing through the die. In Fig. 4c, when $d_i/d_w = 0.2$ inclusion is passing through dies, the SUS304 inclusions show a PEEQ of up to 0.17, whereas the gold wire area in front of the inclusion shows a PEEQ of up to 0.11. In the event, $d_i/d_w = 0.4$, the SUS304 inclusion shows a larger PEEQ of 0.23, and the boundary area in the gold wire shows relatively lower PEEQ of 0.11. In the case of $d_i/d_w = 0.6$, the boundary area of the inclusion shows a

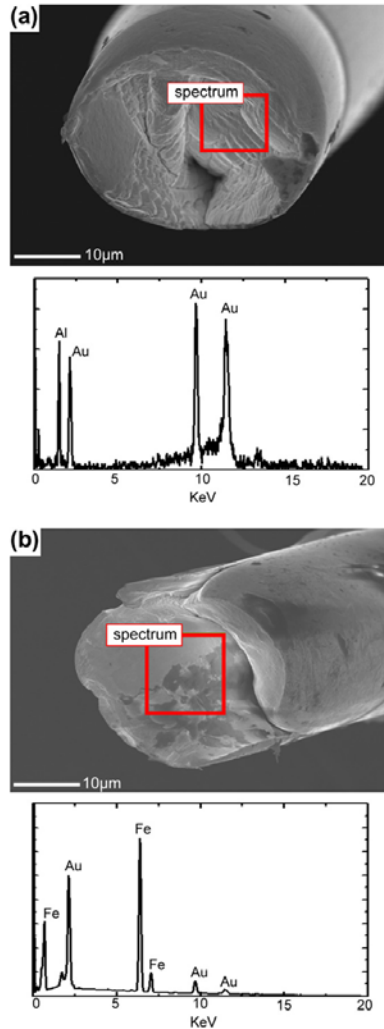


Fig. 3. Fracture surface of gold wire. (a) Al_2O_3 inclusion and (b) SUS304 inclusion.

PEEQ of 0.23, whereas a nearby inclusion in the gold wire only shows an equivalent plastic strain of 0.17. Relative to the Al_2O_3 case, there was no severe deformation area nearby and in front of the inclusions along the wire drawing direction.

Fig. 4d shows the wire drawing stress variations according to the SUS304 inclusion size. When the inclusion passes through the die, the $d_i/d_w = 0.2$ case does not show obvious σ_1 variations. However, at the wire diameter reduction area, σ_1 decreases with a ratio of 0.95 and 0.86 in the case of $d_i/d_w = 0.4$ and 0.6, respectively. Due to the relative lower yield stress of SUS304 than the gold wire, SUS304 is subject to undergo much larger PEEQ than the surrounding gold wire area. There-

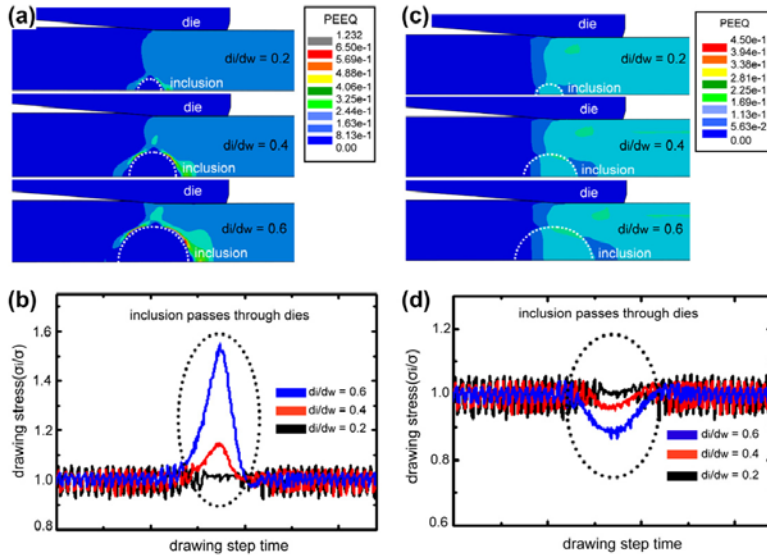


Fig. 4. Equivalent plastic strain distribution and drawing stress of gold wire. (a) PEEQ distribution with inclusion Al_2O_3 , (b) drawing stress with inclusion Al_2O_3 , (c) PEEQ distribution with inclusion SUS304, (d) drawing stress with inclusion SUS304.

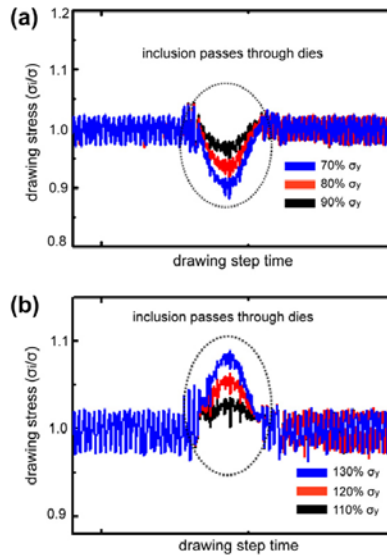


Fig. 5. Gold wire drawing stress with (a) soft inclusion, (b) hard inclusion.

fore, in the case of SUS304, the drawing stress decreased 95% and 86% at the wire diameter reduction area when the ratio of the inclusion diameter to the wire diameter was 0.4 and 06 respectively, because SUS304 requires less stress to be deformed than the work hardened gold wire.

The effect of the Al_2O_3 and SUS304 inclusions on wire drawing stress was calculated by FEM. The results showed that it is able to have both a positive and negative effect on the drawing stress increase in accordance with the size and types of inclusion material, which is related to its mechanical properties.

The calculated results showed difference tendency of drawing stress variation when two types of inclusions are located in the center of wire. In this regard, we introduce an inclusion that has the same mechanical properties with the gold wire but not yield stress. This study is able to examine the yield stress of the inclusions to determine the deformation tendency of the boundary area of the inclusions and gold wire, when a drawing stress is applied. The yield stress of the inclusion was 70%, 80%, 90%, 110%, 120% and 130% relative to the work hardened gold wire yield stress of 100%. The inclusion diameter was fixed to 60% of the gold wire diameter to determine how the yield stress of the inclusion affects the gold wire drawing stress. Fig. 5 shows the variation in drawing stress when different yield stress of the inclusions existed in the center of the wire. In the case of 70%, 80% and 90% yield stress of a work hardened gold wire, σ_1 decreases at a ratio of 0.88, 0.91 and 0.94 at the wire diameter reduction area, respectively. However, the σ_1 increased by 1.03, 1.06, and 1.09 in the case of 110%, 120% and 130% yield stress of a work hardened gold wire, respectively. These results show that the mechanical properties of the inclusion, particularly the yield stress, has an absolute influence on the wire drawing stress variation. This is because hard inclusions in the wire cause considerable deformation in the gold wire maintaining their original shape and causing a higher drawing stress, whereas the soft inclusions deform more easily than the gold wire in the wire diameter reduction area, resulting in less drawing stress.

5. Conclusion

The gold wire drawing characteristics with inclusions was analyzed using the FEM. Al_2O_3 and SUS304 were used as model inclusion materials, which are frequently found on wire breakage surfaces. Both inclusions have a different effect on the gold wire drawing stress. These results were explained by the PEEQ distribution at the boundary area of the gold wire and inclusions. In the case of Al_2O_3 , the inclusions do not show any deformation, whereas the gold wire showed deformation with a PEEQ of up to 1.23. However, in the case of the SUS304 inclusions, both inclusions and gold wire showed a deformed area at the wire diameter reduction area, even though SUS304 exhibits a larger PEEQ value due to its relatively lower yield stress (289.6 MPa) than the work hardened gold wire (484 MPa).

The FEM results of the Al_2O_3 and SUS304 inclusion showed that the drawing stress increases and the value of the PEEQ distribution are correlated. To determine the factor that alters the PEEQ distribution of the boundary area, the yield stress of the inclusions was considered to be a variable. The inclusions had a designated yield stress of 70–130% relative to the work hardened gold yield stress of 100%, and the inclusion diameter was fixed to 60% of the gold wire diameter. The FEM showed that inclusions with a lower yield stress than the gold wire cause a decrease in drawing force while inclusions with a higher yield stress than the gold wire cause an increase in drawing stress.

Acknowledgment

This study was carried out for "The Material & Component technology development program" funded by the Ministry of Knowledge & Economy (MKE) of Korea.

References

- [1] Khoury SL, Burkhard DJ, Galloway DP, Scharr TA. A comparison of copper and gold wire bonding on integrated circuit devices. IEEE Trans. Comp. Hybrids, Manuf., Tech. 1990;13:673–81.
- [2] Kang SH, Jung HS, Bang WH, Cho J-H, Oh KH, Kim DS, et al. High tensile strength of drawn gold. Mater Sci Forum 2007;495–497:907–12.
- [3] Tomiyama S, Fukui Y. Gold bonding wire for semiconductor applications. Gold Bull 1982;15:43–50.
- [4] Cho J-H, Rollett AD, Cho J-S, Park Y-J, Park S-H, Oh KH. Investigation on cold-drawn gold bonding wire with serial and reverse-direction drawing. Mater Sci Eng A 2006;432:202–15.
- [5] B Campos H, Cetlin PR. The influence of die semi-angle and of the coefficient of friction on the uniform tensile elongation of drawn copper bars. J Mater Process Technol 1998;80–81:388–91.
- [6] Cho H, Jo H-H, Lee S-G, Kim B-M, Kim Y-J. Effect of reduction ratio, inclusion size and distance between inclusions on wire breaks in Cu fine wire drawing. J Mater Process Technol 2002;130–131:416–20.
- [7] McAllen PJ, Phelan P. Numerical analysis of axisymmetric wire drawing by means of a coupled damage model. J Mater Process Technol 2007;183(2–3):210–8.
- [8] Yoshida K, Norasethasopon S, Shinohara T, Ido R. Influence of flaws of wire-rod surface, inclusions and voids on wire breaks in superfine wire drawing. JSME Int J A 2003;46(3):365–70.
- [9] Norasethasopon S, Yoshida K. Finite-element simulation of inclusion size effects on copper shaped-wire drawing. Mater Sci Eng 2006;422(1–2):252–8.
- [10] Raskin C, Janssen J. Copper wire breaks – another view. Wire J Int 1998;3(12):80–6.
- [11] Yoshida K. FEM analysis of wire breaks in drawing of superfine wire with an inclusion. Wire J Int 2000;33(3):102–7.
- [12] Blazynski TZ. Design of tools for deformation process. London: Elsevier Applied Science; 1986.
- [13] Sachs G. Plasticity problems in metals. Trans Faraday Soc 1928;24:84–92.
- [14] Luis CJ, León J, Luri R. Comparison between finite element method and analytical methods for studying wire drawing processes. J Mater Process Technol 2005;164–165:1218–25.

- [15] Rubio EM, Camacho AM, Sevilla L, Sebastián MA. Calculation of the forward tension in drawing process. *J Mater Process Technol* 2005;162–163(SPEC. ISS.):551–7.
- [16] Norasethasopon S, Yoshida K. Influences of inclusion shape and size in drawing of copper shaped-wire. *J Mater Process Technol* 2006;172(3):400–6.
- [17] Norasethasopon S, Yoshida K. Prediction of chevron crack initiation in inclusion, copper shaped-wire drawing. *Eng Fail Anal* 2008;15(4):378–93.

Appendix 2. Published paper during master's degree

Gold Bull (2011) 44:231–237
DOI 10.1007/s13404-011-0035-4

ORIGINAL PAPER

Relationship between microstructure homogeneity and bonding stability of ultrafine gold wire

Seung-Bum Son · Hyunchul Roh · Suk Hoon Kang ·
Hee-Suk Chung · Do Hyun Kim · Yong Seok Choi ·
Jong Soo Cho · Jeong-Tak Moon · Kyu Hwan Oh

Published online: 17 November 2011
© The Author(s) 2011. This article is published with open access at Springerlink.com

Abstract Inhomogeneous microtexture evolution during the cold drawing process usually results in lean, sway, or sweep failure. The $\langle 111 \rangle$ longitudinal fiber texture has higher stiffness than the $\langle 100 \rangle$ texture and its proportion and distribution in the cross-section are critical for the bonding stability of fine gold wire. We investigated the inhomogeneous microtexture evolution of gold wire that was cold drawn through an asymmetric diamond die. In this study, the distributions of the $\langle 111 \rangle$ and $\langle 100 \rangle$ textures in a 20 μm diameter fine gold wire are the variables and their effects on the bonding stability of the wire were estimated by electron backscattered diffraction (EBSD) and finite element method (FEM) simulations. The use of a focused ion beam apparatus enabled a high quality of band contrast of the EBSD to be achieved in the exact half cross-sectional area of the fine gold wire. The detailed three-dimensional

FEM results show that the asymmetric distribution of the textures plays a crucial role in increasing the spatial displacement of the gold bonding wire.

Keywords Gold bonding wire · Bonding stability · EBSD · FEM

Introduction

Recently, gold bonding wire has been extensively used for the fabrication of integrated circuits (ICs) because of its good electrical conductivity and mechanical stability with a diameter of 20 μm or less [1–3]. To advance the miniaturization of electronic packages, the process of creating gold bonding wire less than $\sim 20 \mu\text{m}$ in diameter has been performed by repeated cold drawing through diamond dies until the desired diameter is achieved. Repeated cold drawing affects the microstructure of the gold bonding wires, which leads to an inhomogeneous texture due to the asymmetric deformation caused by the imbalanced contact with the dies. From this perspective, it is crucial to investigate the proper drawing conditions through several steps, which enable the fine gold bonding wire to provide a reliable interconnection and bonding stability in an electronic package. There have been many reports on the formation of undesirable intermetallic compounds between the bonding wire and metal pad, since they decrease the electric conductivity and durability [4–6]. The residual stress after cold drawing has also attracted attention in industry because it can reduce the mechanical properties of the wire, such as its yield strength and ultimate tensile strength [7, 8]. However, there have not been any microstructure or texture studies that dealt with the

S.-B. Son · H. Roh · D. H. Kim · Y. S. Choi · J. S. Cho ·
K. H. Oh (✉)
Department of Materials Science and Engineering,
Seoul National University,
Seoul 151-742, South Korea
e-mail: kyuhwan@snu.ac.kr

S. H. Kang
Nuclear Materials Research Division,
Korea Atomic Energy Research Institute,
1045 Daedeok-daero,
Yuseong-gu, Daejeon 305-353, South Korea

H.-S. Chung
Fundamental Technology Group, Central R&D Institute,
Samsung Electro-Mechanics,
Suwon 443-743, South Korea

J. S. Cho · J.-T. Moon
MK electron,
316-2 Geumeo-ni, Pogok-myeon,
Yongin-si, Gyeong gi-do 449-810, South Korea

 Springer

bonding stability until now. In this sense, our study focused on the microstructure and texture distribution of cold drawing gold bonding wire to reveal the inhomogeneity of the bonding stability in a microtextural way.

As regards the texture features in cold drawn gold bonding wire investigated using electron backscattered diffraction (EBSD) analysis, the $\langle 100 \rangle$ and $\langle 111 \rangle$ textures are observed with dominant crystal directions along the wire drawing direction [9–12]. In general, the $\langle 100 \rangle$ and $\langle 111 \rangle$ textures are located at the center and between the surface and center of the gold wire, respectively. Furthermore, the relative fraction of $\langle 100 \rangle$ and $\langle 111 \rangle$ textures is known to be controlled by the stacking fault energy of the materials and corresponding processes such as drawing (volume fraction of $\langle 100 \rangle$ decreases and $\langle 111 \rangle$ increases) and annealing ($\langle 100 \rangle$ grains grow into $\langle 111 \rangle$ grains during heat treatment) [3, 11, 13, 14].

When we consider that every single step in the reduction of the wire diameter is related to the shear deformation of the wire, which rotates the crystal directions from $\langle 100 \rangle$ to $\langle 111 \rangle$, and that this shear deformation is caused by the contact with the diamond dies, it is clear that the dies play an important role in the symmetric or asymmetric texture evolution of the drawn wires. The inhomogeneity of shear deformation in the drawn wire results not only in a decrease of its draw ability, but also in a decrease of its physical properties, such as its electrical conductivity, current density, and mechanical properties [14–16]. In this research, the possible inhomogeneous deformation of fine gold drawn wire is analyzed in terms of the texture distribution using EBSD and the bonding stability of the drawn wire is investigated using FEM.

Experimental procedures

EBSD samples of gold wire were prepared by focused ion beam (FIB) milling. An FEI NOVA200 dual-beam system was used for the preparation of the gold wire samples. Sample preparation through FIB milling results in high-quality EBSD band contrast [17, 18]. The ion source is liquid Ga metal and ion milling currents ranging from 50 pA to 3 nA and a constant accelerating voltage of 30 kV were used for the gold wire milling. In this research, it is also important to achieve the exact half cross-sectional area of the drawn wire to define the symmetric wire deformation. By FIB milling, it is possible to obtain the exact half cross-sectional area of the drawn wire, which enables one to analyze the symmetric or asymmetric texture distributions during the drawing process. An HR-EBSD system (JEOL 6500 F with INCA/OXFORD EBSD system) was used for the measurement of the texture distribution of the

gold wire. An accelerating voltage of 20 kV and probe current of 4 nA were used for this measurement.

The manner in which the asymmetric texture of the drawn gold wire affects its bonding stability is proven by FEM analysis. ABAQUS 6.9 and CATIA V5 software were used for this FEM research. The CPS4 (two-dimensional) and C3D8 (three-dimensional) element types were used in this process to investigate the arched shape problem of the gold bonding wire.

It has already been reported that gold wire has mechanical property anisotropy because it has a different Young's modulus depending on the crystal direction [19, 20]. The Young's modulus of each orientation is calculated based on the following equation.

$$\frac{1}{E_{ijk}} = S_{11} - 2(S_{11} - S_{12} - \frac{1}{2}S_{44})(\lambda_{11}^2\lambda_{j2}^2 + \lambda_{j2}^2\lambda_{k3}^2 + \lambda_{k3}^2\lambda_{11}^2) \quad (1)$$

where, E_{ijk} is the Young's modulus in the $[ijk]$ direction; λ_{11} , λ_{j2} , and λ_{k3} are the direction cosines of the directional $[ijk]$; and S_{11} , S_{12} , and S_{44} are the elastic constants of an isotropic material given by

$$S_{11} = \frac{1}{E}, \quad S_{12} = -\frac{\nu}{E}, \quad S_{44} = \frac{1}{G}. \quad (2)$$

where, E is the Young's modulus, ν is the Poisson ratio, and G the shear modulus [21]. From the above equations, it is confirmed that each crystal direction has a different Young's modulus. In the case of gold, the $\langle 111 \rangle$, $\langle 110 \rangle$, and $\langle 100 \rangle$ crystal directions show Young's moduli of 116.28, 81.47, and 42.91 GPa, respectively.

The stress–strain curve of 20 μm diameter gold wire is achieved for the purpose of applying its mechanical properties to FEM analysis. Table 1 compares the mechanical properties of the bulk gold to the fine gold wire. The reported yield stress and ultimate tensile strength of bulk gold are 205 and 120 MPa, respectively, but can be affected by the history and heat treatment. The remarkable differences in the mechanical properties of these two materials are due to the work hardening of the fine gold wire caused by the numerous cold drawing treatments and the increase of the proportion of $\langle 111 \rangle$ texture in the fine drawing wire [1, 22, 23].

Table 1 Mechanical properties of bulk gold and fine gold wire

Material	Parameter	Value	Unit
Bulk gold	Young's modulus (E)	77.2	GPa
	Yield stress (σ_y)	205	MPa
	Ultimate tensile strength	120	MPa
Fine gold wire	Young's modulus (E)	65.7	GPa
	Yield stress (σ_y)	484	MPa
	Ultimate tensile strength	538	MPa

Results and discussion

After the gold wire is bonded, it can be seen that each wire has a different bonding shape and leans toward the other wires as shown in Fig. 1a, b. This nonstraightness problem has not been studied until now and the reason for this problem is also not known yet exactly. The drawing dies and microtexture distribution of the cold drawn gold wire is observed in an attempt to solve this problem.

As the bonding wire is formed by continuous cold drawing, its asymmetric deformation caused by the drawing dies is more or less effective depending on how the die and wire contact each other. Even if the wire has an inhomogeneous deformation resulting from the asymmetric dies, the inhomogeneity of the drawn wire can be increased or decreased by the subsequent drawing process. This can explain the locally observed arched bonding wire in Fig. 1. We should also consider that the asymmetric deformation in the drawn wire can occur not only leftward and rightward, but also forward and backward in the bonding wire.

Figure 1a, b show the straight and arched bonding wires and the schematics of the corresponding drawing process with dies. In Fig. 1b, the unexpected connection between the bonding wires causes a short-circuit problem and this

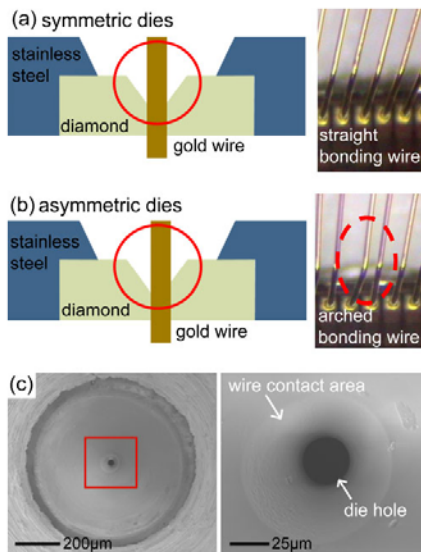


Fig. 1 Schematics, optical, and SEM images of drawing dies and the gold wire. **a** Symmetric dies and straight bonding wire. **b** Asymmetric dies and arched bonding wire. **c** SEM images of an asymmetric die

leads to IC chip failure, which means the failure of the device. We observed the SEM images of the drawing dies as the bonding wire is drawn through them to find the reason for the straightness problem of the bonding wire. Figure 1c shows the SEM images of the drawing dies. It can be seen that the drawing die is damaged around the hole area during the wire drawing process. However, the drawing wire diameter reduction area does not have the shape of a perfect circle and it is not centered on the hole. This observation tells us that there is a possibility for the asymmetrical deformation of the gold wire to occur. Asymmetric rolling is used to deliver enough sheer strain to the whole volume of the object and reduce the pressure during rolling, however it can also cause an asymmetric texture distribution since the texture evolution in the cold drawn wire is highly related to the sheer deformation [24, 25].

A two dimensional element type FEM simulation is used to quantify the relationship between the asymmetric shape of the die and displacement of the wire centerline and the $\langle 100 \rangle$ fiber center line. Figures 2a and b show the simplified schematics of the symmetric and asymmetric drawing processes. The gold wire model in this FEM study is assumed to have a diameter of 20 μm and be filled with 25% of $\langle 100 \rangle$ fiber in the center area and $\langle 111 \rangle$ fiber in the remaining area for the sake of simplicity. The volume fraction of $\langle 111 \rangle$ and $\langle 100 \rangle$ fiber is based on our EBSD study. The drawing die is designed to have a reduction ratio of 6% and reduction angle of 6° . The previously calculated mechanical properties of the $\langle 111 \rangle$ and $\langle 100 \rangle$ fibers of gold wire are applied in this model. It is assumed that the asymmetric dies have a spatial displacement compared to the symmetric dies. The spatial displacement between the symmetric dies and asymmetric dies is represented as a function of the displacement of the die. The spatial displacement of the wire center lines after drawing and the $\langle 100 \rangle$ center line are represented as a function of d_{100}/d_w . In Fig. 2b, even though the $\langle 100 \rangle$ center line also shows a spatial displacement after drawing according to our FEM study, it is represented as a straight line for the sake of providing easily perceptible schematics.

In Fig. 2c, the curve of d_{100}/d_w versus the displacement of the die is shown. As the displacement of the die increases, d_{100}/d_w increases as well. The curve generally shows linear behavior and makes it plain that the asymmetric shape of the dies affects the deformation tendency and results in the asymmetric deformation of the drawn wire. Considering that ultrafine gold wire is achieved by a large number of cold drawing processes, it is expected that ultrafine gold wire with an inhomogeneous microstructure can be produced in this way.

As shown in Fig. 3a, b, an EBSD analysis is performed to define the microstructure and differences of the texture distribution in the wires. Two samples of wire, one straight

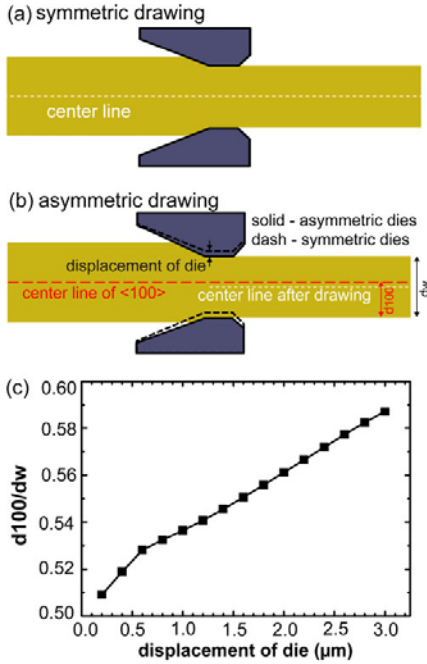


Fig. 2 Two-dimensional FEM simulation. **a** Schematic of symmetric drawing. **b** Schematic of asymmetric drawing. **c** d_{100}/d_w with regard to displacement of die

and the other arched, were collected to compare their texture distributions. Figure 3a shows an FIB ion image and EBSD rolling direction (RD) map of the corresponding area in the straight wire. It is observed that most of the area in the center of the wire is filled with the RD//<100> texture and that the RD//<111> texture is mainly located on the surface area of the gold wire, as expected. It can also be observed that the gold wire has a symmetric texture distribution, which means that the gold wire has been subjected to symmetric deformation, as the RD//<100> fibers are replaced by RD//<111> ones during cold drawing [3].

In Fig. 3b, however, the problem we are interested in is that the RD//<100> texture in the arched wire is not located at the exact center of the wire. It is observed that the <100> direction is not located in the exact center of the wire and that the value of d_{100}/d_w is approximately 0.6. As shown in our FEM results, the RD//<100> texture, which is not located in the exact center of the drawn wire, indicates that

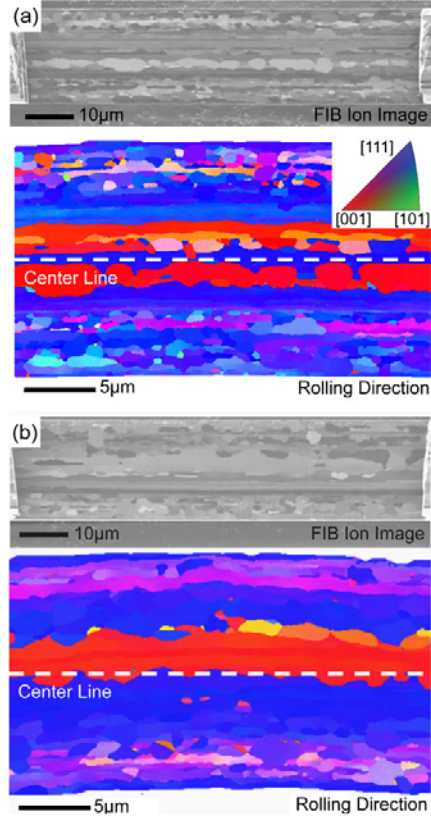


Fig. 3 FIB ion images and EBSD RD mappings of 20 μm gold wire. **a** Straight gold drawing wire and orientation color key. **b** Arched gold drawing wire

the drawn gold wire underwent asymmetric deformation while being drawn through the drawing dies.

Three-dimensional FEM models are applied to analyze this arched wire problem and the simulation models used in this research are shown in Fig. 4a. We assumed that the drawn gold wire is simply composed of two crystal directions, <100> and <111>, even though there are some other mixed crystal directions at the wire surface. The location of the <100> direction in each model is represented by d_{100}/d_w and has approximate values of 0.6, 0.7, 0.8, and 0.9 in the four models, respectively. The diameter of the <100> direction area is

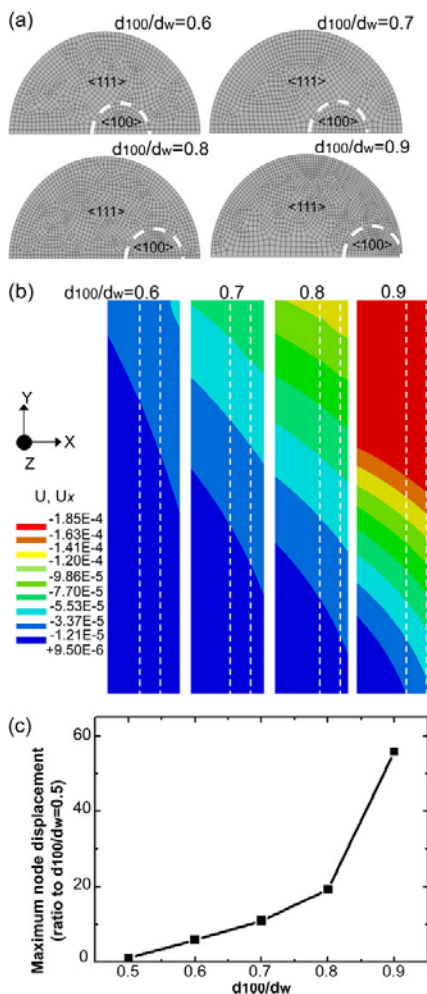


Fig. 4 Three-dimensional FEM models and simulations. **a** Normal views of four models applied in the FEM. **b** Spatial displacement contour maps in the x direction of four models. **c** Selected node displacement in x direction

assumed to be $5 \mu\text{m}$ based on our EBSD measurement results for the $20 \mu\text{m}$ diameter gold wire. All of the mechanical properties of our research models are based on

gold, but the Young's modulus of each crystal direction is applied based on the calculated results.

It is expected that the deformation shapes of the tensioned gold wire are different depending on the location of the $\langle 100 \rangle$ direction in the wire. In this FEM research, it is assumed that the bottoms of the wires are fixed, as the gold bonding wires are bonded to a metal pad. The tensile forces are applied to the upper side of each bonding wire in the FEM models [26]. Based on the location of the $\langle 100 \rangle$ direction, four models are determined and the same forces are applied to each. As shown in Fig. 4a, the location of the $\langle 100 \rangle$ direction in the four models is represented by d_{100}/d_w and have approximate values of 0.6, 0.7, 0.8, and 0.9, respectively.

Figure 4b shows the contour of spatial displacement in the x direction of the nodes in each model. All of the models in Fig. 4b correspond to those in Fig. 4a. The wire models adopted in our FEM study are assumed to have a length of $120 \mu\text{m}$ to reduce the computational cost, even though the actual bonding wires have a length of more than 1mm [27]. The dotted line in the models indicates the location of the $\langle 100 \rangle$ direction in the bonding wire models. All of the models show that the deformations caused by the tensile force are asymmetric and the right sides of the bonding wire models have more deformation than the left sides. The difference in the Young's modulus between the $\langle 111 \rangle$ and $\langle 100 \rangle$ directions is one reason for the asymmetric deformation of the bonding wire models. In general, the value of the Young's modulus indicates the stiffness and resistance to permanent deformation. In this regard, the simulated FEM models in Fig. 4b shows that the deformation caused by the bonding force is focused on the area where the $\langle 100 \rangle$ directions are located. Thus, the degree of d_{100}/d_w texture affects the asymmetric deformation of the bonding wire. The model with $d_{100}/d_w = 0.6$ shows a maximum spatial displacement of $-3.37 \text{E}-5$ in the x direction at the end of the wire. However, this spatial displacement value is based on the FEM models that have a wire length of $120 \mu\text{m}$. As mentioned above, the bonding wire used in the devices has a length of more than 1mm and this indicates that the actual bonding wire could have a greater spatial displacement at a specific point as the length of the wire increases. The results in Fig. 4b showing the concentration of the spatial displacement toward the end of the wire also confirms this hypothesis.

It is obvious that the bonding wires lean toward the left side because the $\langle 100 \rangle$ direction is located on the right side of the bonding wire models. In the case of the model with $d_{100}/d_w = 0.9$, its $\langle 100 \rangle$ direction is located almost at the surface of the gold bonding wire, and it shows a maximum spatial displacement of $-1.85 \text{E}-4 \mu\text{m}$ in the x direction, which is almost one order of magnitude higher than the value of $d_{100}/d_w = 0.6$.

In Fig. 4c, the curve of maximum node displacement in the x direction shown in Fig. 4b (ratio to $d_{100}/d_w=0.5$) versus d_{100}/d_w is shown. In our FEM study, the node displacement of the x direction is considered, because x is the most unfavorable direction from the point of view of the bonding stability and mechanical durability of the IC. As already shown in Fig. 4b, when moving away from the center of the wires in the $\langle 100 \rangle$ direction, the bonding wires lean more to the opposite side of the $\langle 100 \rangle$ direction. All of the models in the FEM study show that the maximum node displacement is proportional to the value of d_{100}/d_w and this means that the higher the value of d_{100}/d_w , the more the gold wire leans against the other gold bonding wires. Even in the case of d_{100}/d_w showing a value of 0.6, the node displacement in the x direction indicates the fivefold amount of $d_{100}/d_w=0.5$, which may be responsible for the severe leaning problem shown in Fig. 1b. What is more, this spatial displacement ratio of d_{100}/d_w is expected to have a higher value depending on the length of the bonding wire. When the value of d_{100}/d_w goes to 0.9, the maximum node displacement is exponentially increased, and this happens because the location of the $\langle 100 \rangle$ direction is extremely close to the surface of the gold bonding wire and this reduces the binding force from the interfaces that work to prevent the wire from leaning in the opposite direction.

Conclusions

In this research, we analyzed how the bonding wire straightness problem occur using EBSD and FEM analysis. By observing the SEM images of the wire dies, it can be seen that the dies have asymmetrical shapes near the wire reduction area. Asymmetrical dies lead to asymmetrical deformation of the bonding wire as confirmed by EBSD analysis. Considering that the RD// $\langle 100 \rangle$ rotates to the RD// $\langle 111 \rangle$ during the gold wire drawing process, it is thought that the gold wire undergoes asymmetrical deformation in the drawing process. We calculated the Young's modulus of each orientation and applied these to the FEM analysis. The positional deviation of the $\langle 100 \rangle$ texture from the center line of the wire is indicated by the d_{100}/d_w value. The results show that as d_{100}/d_w changes from 0.5 ($\langle 100 \rangle$ at the center) to 0.9 ($\langle 100 \rangle$ at the surface of the wire), the maximum amount of spatial displacement is exponentially increased, because the Young's moduli of the $\langle 111 \rangle$ and $\langle 100 \rangle$ orientations were found to be 116.28 and 42.91 GPa, respectively.

Acknowledgment This research (paper) was performed for "the Material & Component Technology Development Program" funded by the Ministry of Knowledge & Economy (MKE) of Korea.

Open Access This article is distributed under the terms of the Creative Commons Attribution License which permits any use,

distribution and reproduction in any medium, provided the original author(s) and source are credited.

References

- Kang SH, Jung HS, Bang WH et al (2005) High tensile strength of drawn gold. *Mater Sci Forum* 495:907–912
- Tomiyama S, Fukui Y (1982) Gold bonding wire for semiconductor applications. *Gold Bull* 15:43–50
- Cho JH, Rollett AD, Cho JS, Park YJ, Park SH, Oh KH (2006) Investigation on cold-drawn gold bonding wire with serial and reverse-direction drawing. *Mater Sci Eng, A* 432:202–215
- Yu C-F, Chan C-M, Chan L-C, Hsieh K-C (2011) Cu wire bond microstructure analysis and failure mechanism. *Microelectron Reliab* 51:119–124
- Chen J, Lai YS, Wang YW, Kao CR (2011) Investigation of growth behavior of Al–Cu intermetallic compounds in Cu wire bonding. *Microelectron Reliab* 51:125–129
- Ji HJ, Li MY, Wang CQ, Bang HS (2007) Comparison of interface evolution of ultrasonic aluminum and gold wire wedge bonds during thermal aging. *Mater Sci Eng, A* 447:111–118
- Elices M (2004) Influence of residual stresses in the performance of cold-drawn pearlitic wires. *J Mater Sci* 39:3889–3899
- Yang F, Jiang JQ, Fang F, Wang Y, Ma C (2008) Rapid determination of residual stress profiles in ferrite phase of cold-drawn wire by XRD and layer removal technique. *Mater Sci Eng, A* 486:455–460
- Dillamore IL (1964) Factors affecting the rolling recrystallisation textures in F.C.C. metals. *Acta Metall Mater* 12:1005–1014
- Wulff F, Breach CD, Dittmer K (2003) Crystallographic texture of drawn gold bonding wires using electron backscattered diffraction (EBSD). *J Mater Sci Lett* 22:1373–1376
- Cho JH, Cho JS, Moon JT (2003) Recrystallization and grain growth of cold-drawn gold bonding wire. *Metall Mater Trans* 34 A:1113–1125
- English AT, Chin GY (1965) On the variation of wire texture with stacking fault energy in F.C.C. metals and alloys. *Acta Metall Mater* 13:1013–1016
- Seeger A (1964) The stacking-fault energy of gold and silver. *Phil Mag* 101:887–890
- Hasani GH, Mahmudi R, Karimi-Taberi A (2010) On the strain inhomogeneity in drawn copper wires. *Int J Mater Form* 3:59–64
- De Castro ALR, Campos HB, Cetlin PR (1996) Influence of die semi-angle on mechanical properties of single and multiple pass drawn copper. *J Mater Process Tech* 60:179–182
- Rajan K, Petkie R (1998) Microtexture and anisotropy in wire drawn copper. *Mater Sci Eng, A* 257:185–197
- Mateescu N, Ferry M, Xu W, Cairney JM (2007) Some factors affecting EBSD pattern quality of Ga⁺ ion-milled face centered cubic metal surfaces. *Mater Chem Phys* 106:142–148
- Matteson TL, Schwarz SW, Houge EC, Kempshall BW, Giannuzzi LA (2002) Electron backscattered diffraction investigation of focused ion beam surfaces. *J Electron Mater* 31:33–39
- Noguchi K, Araki M, Ohno Y (2000) Preparation of transmission electron microscopy specimens of as-drawn gold wire. *Scripta Mater* 43:199–204
- Hannula SP, Wanagel J, Li CY (1983) Evaluation of mechanical properties of thin wires for electrical interconnections. *IEEE Trans Components Hybrids Manuf Technol* 6:494–502
- Meyers MA, Chawla KK (2009) *Mechanical behavior of materials*. New York, Cambridge
- Espinosa HD, Prorok BC, Peng B (2004) Plasticity size effects in free-standing submicron polycrystalline FCC films subjected to pure tension. *J Mech Phys Solid* 52:667–668

23. Wu B, Heidelberg A, Boland JJ (2005) Mechanical properties of ultrahigh-strength gold nanowires. *Nat Mater* 4:525–529
24. Maksimov EA (2011) Reducing pressure on the rolls and tension in the asymmetric cold-rolling of strip. *Metallurgist* 54:753–757
25. Cheon BH, Kim HW, Lee JC (2011) Asymmetric rolling of strip-cast Al-5.5 Mg-0.3Cu alloy sheet: Effects on the formability and mechanical properties. *Mater Sci Eng, A* 528:5223–5227
26. Tian YH, Wang CQ, Zhou YN (2008) Bonding mechanism of ultrasonic wedge bonding of copper wire on Au/Ni/Cu substrate. *T Nonfer Metal Soc* 18:132–137
27. Groover R, Shu WK, Lee SS (1994) Wire bond loop profile development for fine-pitch long-wire assembly. *IEEE Trans Semicond Manuf* 7:393–399

감사의 글

대학원에서의 시간은 제가 모르는 것이 무엇인지를 알고 그 해답을 찾기 위해 고민하는 시간이었던 것 같습니다. 그 고민의 시간들은 저를 학문적으로 그리고 정신적으로 성숙하게 만들어 주는 고마운 시간이었습니다. 아직도 많이 부족한 제 자신이지만 학교를 떠나는 지금, 그 시간들을 함께 해준 분들께 감사의 말씀을 드리고자 글을 씁니다.

먼저 항상 새로운 시각으로 사물을 바라보도록 지도하여 주신 저의 지도 교수님인 오규환 교수님께 감사 드립니다. 교수님께서 보여주신 학문에 대한 열정과 노력은 제가 연구자로 살아가면서 닦고 싶은 모습이기도 하였습니다. 학교의 울타리를 벗어난 곳에서의 교수님의 가르침은 저에게 좀 더 가까이 다가왔고, 쉽게 떠나지 않았습니다. 좋은 기회를 주셔서 정말 감사합니다. Castle Rock에서의 말씀을 잊지 않으며 연구하도록 하겠습니다.

Boulder에서의 생활 동안 저를 지도하여 주신 이세희 교수님께도 깊은 감사의 말씀을 드립니다. 교수님의 세심한 지도에 좋은 결과를 얻을 수 있었습니다. 졸업 후에도 교수님과 좋은 인연으로 같이 연구할 수 있는 기회가 있기를 바랍니다.

그리고 박사학위 논문을 작성하는데 있어 큰 도움을 주신 손현준 교수님, 유용렬 교수님, 강기석 교수님, 그리고 강선호 상무님께도 깊은 감사를 드립니다.

대학원에 입학하여 많은 시간이 지났습니다. 그 동안 연구실 선후배님들에게 참 많은 도움을 받았습니다. 이 기회에 모두에게 정말 고맙다는 말을 하고 싶습니다. 희석이형, 입학 당시 아무것도 모르는 저를 너무나도 잘 이끌어 주셨습니다. 형 같은 선배가 되고 싶었는데, 쉽지 않았던 것 같습니다. 석훈이형, 제게 성실함이 무엇인지 몸으로 보여 주셨었습니다. 형께서 저의 마무리 투수가 되어 주시겠다던 말, 너무 고맙습니다. 지우형, 불더에서 함께 지낸 시간들, 즐거웠습니다. Boulder 에서 열심히 생활하시는 형을 보면서 저는 스스로 반성을 많이 했습니다. 형과 저는 앞으로도 같은 분야에서 같이 연구하게 되겠죠? 도움이 되는 후배가 될 수 있도록 하겠습니다. 은규형, Ohio에 계실 때 많이 도와드리고 싶었는데, 그러지 못했던 것 같아 항상 죄송스런 마음이 있습니다. 모자란 후배를 앞으로도 많이 도와주세요. 정윤이형, 저는 형과 같이 학교 생활을 오래하지 못한 것이 참 아쉽습니다. 그래서 형이 빨리 돌아오기를 바라기도 했습니다. 형이 이제야 돌아오는데, 저는 떠나는군요. 또 아쉽습니다. 종수형, 와이어부터 Si까지, 형과 저는 아무래도 앞으로도 쪽 같이 갈 인연인 것 같습니다. 연구가 아니더라도 같이 갈 인연이지요. 정말 감사합니다. 영광이형, 아무것도 모르는 제게 친절히 Abaqus를 알려 주시던 기억이 납니다. 바쁘신 가운데 제가 답답하기도 하셨을 텐데, 침착한 모습만 보여주시고 가신 것 같습니다. 조금이나마 도움이 되었던 후배로 기억되면 좋겠습니다. 슬참이형, 입학 당시 형이 해주셨던 충고, 정말 많은 도움이 되었습니다. Boulder에서 형과 함께 보낸 시간은 즐거운 추억으로 오래오래 남을 것 같습니다. 연구적으로 그리고 정신적으로 도와주셔서 감사합니다.

도현아, 308호에서 아무것도 모르는 나를 잡고 친절히 알려줘서 고맙다. 너 덕분에 혼자서 308호의 장비들을 사용할 수 있었다. 너의 꼼꼼함과 순수한 열정도 배워야 할 텐데, 너의 장점이 부럽다. 정한이형, 형에게 필요한 후배가 되고 싶었는데, 그러지 못한 것 같아 많이 아쉽습니다. 부족한 후배, 앞으로도 잘 부탁 드립니다. 의선아, 지금 돌이켜 보면 나와 다르다는 이유로 널 이해하려는 내 노력이 부족하지 않았나 하는 생각이 든다. 앞으로 기회를 더 만들어 보자. 태준아, 우리는 공통점이 많아 쉽게 친해졌던 기억이 난다. 지금처럼 노력하면 앞으로 좋은 기회가 올 거라고 생각한다. 힘내라. 범라인 기범아, 항상 바쁘다는 핑계로 술 한잔 하자는 말 먼저 하지 못해 미안하다. 곧 한잔 하자. 용석아, 좋은 결과 얻어서 돌아오길 바란다. 그리고 산다라 사건은 미안하다. 규정아, 너가 없으니 연구실이 허전하다. 성실한 놈. 잘하고 돌아와라. 찬순아, 방장으로서는 연구실을 이끌어 나가느라 고생이 참 많구나. 그 성실함이면 어디서든 성공할 수 있을거야. 건강 생각해서라도 잠은 꼭 집에 가서 자도록 하고. 석현아, 요새 열심히 생활하는 것 같아 보기 좋다. 내가 옆에서 괴롭혀서 귀찮았지? 이제 간다. 그리고, 건강해야 꾸준히 오래간다. 진우야, 신입생답지 않은 존재감으로 연구실을 잘 받쳐주어 고맙구나. 앞으로 연구실을 잘 이끌어 주기 바란다. 총찬아, 이사할 때 스스로 도어락을 교체하겠다고며 날 도와주던 얼굴이 생각나는구나. 항상 그렇게 웃는 얼굴로 주위를 살피면서 훌륭한 연구하기를 바란다. 경일아, 선배로서 좋은 이야기들을 많이 해주려고 했는데, 도움이 되었는지 모르겠다. 다음에 형이 술 한잔 사마. 상섭아, 너와는 진지한 대화를 나눈 기억이 몇 번 없는 것 같구나.

너가 알아서 잘 하니까 그런 것 같다. 형이 떠나도 너와는 같이 일할 기회가 많이 있을 것 같다. 자주 연락하며 같이 연구하자.

I want to thank Dani, Tom and Jae-Ha for involving me in your research. I learned a lot from you and I really enjoyed the moment when we worked and discussed together. I hope we work together sometime in near future.

한홍남 교수님 연구실의 동기 애기 아빠 훈휘, 멋쟁이 용민이, 왠지 고독이라는 단어가 어울리는 현식이, 회식은 빠지지 않을 것 같은 동완이, 알게 모르게 날 잘 챙겨준 문조, 항상 나에게 아쉽다고 말해주는 양후, 이제 우리방 같은 근호, 생각보다 수다쟁이인 준영이, 새로 들어온 유정이와 성규. 모두 고맙고, 좋은 결과 얻어서 졸업하기를 바랍니다. 김미영 교수님 방의 덕황씨, 잘 챙겨줘서 고마워요. 먼저 갈 테니 빨리 따라와요. 승용씨, 많은 도움 드리고 싶었는데 많이 부족했던 것 같네요. 좋은 결과 얻길 바래요.

MKE의 문정탁 이사님, 조종수 차장님, 그리고 이상한 차장님. 와이어 과제부터 Si과제까지, 그 동안 과제가 무리 없이 잘 진행될 수 있도록 도와주셔서 정말 감사 드립니다. 앞으로도 잘 부탁 드립니다. 연이씨 그리고 김성민씨. 회사 업무에 도움도 안 되는 실험을 하겠다고 매번 귀찮게 헤드려서 죄송하고, 또 잘 도와주셔서 너무 감사합니다. 덕분에 무사히 졸업하게 되었습니다. 순호형, 희상씨, 기강씨, 승환씨, 그리고

전성민씨. 항상 지하에서 고생하시면서도 찾아갈 때마다 웃음을 잃지 않는 모습이 참 인상적이었습니다. 항상 친절하게 맞이하여 주셔서 제가 편하게 MKE에서 실험할 수 있었습니다. 감사합니다.

삼성 SDI의 강선호 상무님, 바쁘신 가운데 논문 심사를 도와 주셔서 감사합니다. 상무님의 조언이 새로운 곳에서의 생활에 큰 도움이 될 것 같습니다. 감사합니다. 최종서 부장님, 만날 때 마다 항상 따뜻하게 반겨 주시고, 관심 가져 주셔서 감사합니다. 나중에 따로 연락 드리고 찾아 뵈 수 있도록 하겠습니다. 김재혁 책임님, 권승욱 책임님, 서순성 책임님, 짧은 시간이었지만 과제가 잘 진행될 수 있도록 도와 주신 점 감사 드립니다. 졸업 후에도 같이 일할 수 있는 기회가 있을 거라고 생각합니다. 종종 연락 드리겠습니다. 김승완 과장님, 여러모로 관심 가져 주셔서 감사합니다. 알게 된 기간이 짧음에도 좋게 봐주시고 도와 주셔서 감사합니다. 저희는 조만간 밖에서 만날 수 있겠죠?

공부한다고 그 동안 소홀했던 나의 안식처 같은 친구들 보영이, 혁준이, 희진이, 상균이, 그리고 동명이. 고등학교 때부터 항상 가까운 옆자리에 있어줘서 고맙다. 너희들이 있어 힘들고 지칠 때 한 박자씩 쉬어갈 수 있었던 것 같다. 앞으로도 자주 보자.

우리 대장 영민이(역시 너가 대장이야), 용원스러운 용원이, 개동현이, 그리고 나와 같은 길을 걷고 있는 돌려 막기 민호. 다들 술 좀 적당히 먹어라. 맨 정신일 때는 다들 정상인데, 그래도 그래서 추억이 그렇게 많이 쌓였나 보다. 그 동안 고마웠다. 앞으로도 잘 부탁한다.

원석이형, 성원이형, 현우형, 정진이형, 병현이, 세령이, 인술이, Paul, 그리고 지은 누나. 어느덧 우리의 인연이 10년째가 되어 갑니다. 공부한다고 항상 바쁜 척 하며 연락도 뜸했었죠. 그래도 틈틈이 나타나면 반갑게 맞아주어 고맙습니다. 앞으로는 잘 할게요.

원혁아, 늦은 나이에 공부 시작하느라 힘들지? 고생해라. 넌 은근히 연구가 어울려. 윤정아, 강현이와 너 모두 건강하지? 너가 원혁이 옆에 있어서 참 안심이야. 덩고 윤정이, 그리고 탕웨이 지나. 우리 결국 관악산 보면서 비빔밥은 못 먹을 것 같다. 뭐 다른 거 먹자, 후식도 꼭.

우리가 꿈처럼 이야기하던 것들이 어느새 하나 둘씩 이루어지고, 이제 새로운 미래를 또 이야기하고 있어. 영선아, 옆에 있어 줘서 고마워.

철없던 막내가 어느새 자랑스런 동생이 되었구나. 승현아, 고맙다.

늦게 철이 들어 공부를 시작하겠다고 아들 믿고 옆에서 아낌없이 도와주신 아버지, 어머니 감사합니다. 아버지, 어머니 덕분에 큰 고생 없이 편하게 공부에 집중할 수 있었습니다. 훌륭한 아들이 되겠습니다.

처음 논문을 쓰기 위해 자리에 앉아 하얀 화면을 바라보면서 어떻게 시작을 하여야 하나 고민하던 시간이 떠오릅니다. 어느덧 마무리를 하게 되었습니다. 자만하지 않고 항상 앞을 바라보는 사람이 되겠습니다.

2013년 12월 30일

손승범